Synthetic Seismograms and Seismic Waveform Modeling

Lupei Zhu
Saint Louis University

2011

i

Acknowledgments

Contents

List of Figures

Chapter 1

Introduction

1.1 Characteristics of seismic waveforms in different distance ranges

Figure 1.1: Example observations and synthetics at ranges where the Earth appears simple (>30°), slightly complicated (upper-mantle ranges, 30° to 14°) and quite complicated (<14°), from [Helmberger, 1983].

Table 1.1: Instrument constants of different seismometers

	STS-1	STS-2	CMG-3ESP	CMG-40T	FBA-23	Episensor
f_0, Hz	$2.7778{\times}10^{-3}$	$8.3333{\times}10^{-3}$	$8.3333{\times}10^{-3}$	$3.3333{\times}10^{-2}$	50	180
G	2500 V/m/s	1500 V/m/s	2000 V/m/s	800 V/m/s	5 V/g	10 V/g

1.2 Seismic instruments and seismic data processing

1.2.1 Seismic instrument response

The output $y(t)$ of a simple vertical seismometer consisting of a spring k and a dash board η in response to ground motion $x(t)$ can be described by:

$$m\ddot{y} = -ky - \eta\dot{y} + mG\ddot{x} \tag{1.1}$$

or

$$\ddot{y} + 2h\omega_0\dot{y} + \omega_0^2 y = G\ddot{x}, \tag{1.2}$$

where $\omega_0 = \sqrt{k/m}$ (natural frequency of the spring), $h = \eta/2\sqrt{mk}$ (damping constant), and G is the amplification factor. Essentially, the response of a simple mechanical seismometer is determined by these three constants.

The frequency response of the seismometer is

$$H(\omega) = \frac{Y(\omega)}{X(\omega)} = \frac{G\omega^2}{\omega^2 - 2ih\omega_0\omega - \omega_0^2}. \tag{1.3}$$

Responses of modern broadband seismometers such as STS-1 and STS-2 take the same form as above, but are often responses to ground velocity instead of displacement. Accelerometers (e.g. FBA) respond to ground acceleration. Their responses are in the form

$$H(\omega) = \frac{-G\omega_0^2}{\omega^2 - 2ih\omega_0\omega - \omega_0^2}, \tag{1.4}$$

with a very large ω_0 (50 to 180 Hz) so that the response is essentially flat at G for $\omega \ll \omega_0$.

The analog output of a seismometer, normally in the unit of volts, is converted into digital counts by the data logger, which also applies a low-pass filter to the signal to avoid sampling aliasing. A 24-bit data logger has a dynamic range of $2^{24} = 144$ dB. For example, the Quantera Q680's digitization constant is 2^{23} counts/20 V and the K2's constant is 2^{23} counts/2 V.

The frequency and dynamic ranges of several popular seismometers are shown in Fig. 1.2.

Often an instrument response is expressed in terms of poles and zeros using z-transform:

$$H(z) = A_0 \frac{\prod_j (z - z_j)}{\prod_j (z - p_j)}, \tag{1.5}$$

where $z = i\omega$. For example, the two poles for the response in Eq. 1.3 are $\omega_0(-h \pm i\sqrt{1 - h^2})$.
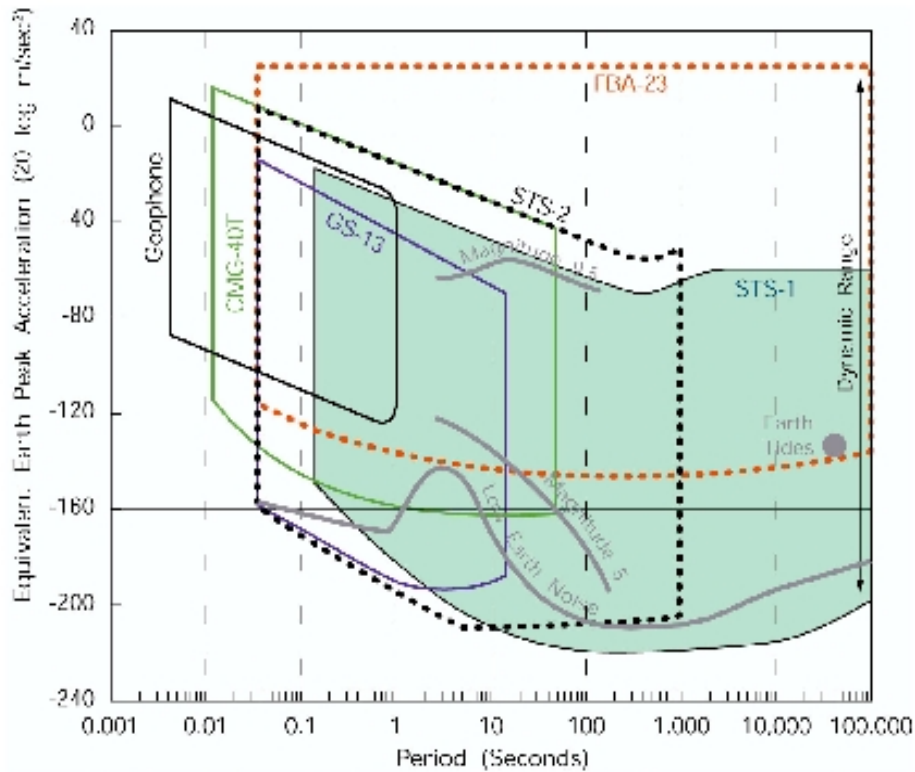
Figure 1.2: Spectral amplitudes of ambient seismic noise, earthquakes (magnitude 5 and 9 recorded at a distance of 4,500 km), and Earth tides.

1.2.2 Digital signal processing

The output of a seismic instrument is the convolution of input $x(t)$ and instrument response:

$$y(t) = h(t) * x(t) = \int_{-\infty}^{\infty} h(\tau - t)x(\tau)\mathrm{d}\tau. \tag{1.6}$$

Removing instrument response in $y(t)$ (deconvolution) can therefore be done either in the frequency domain using spectrum division in the time domain by solving a linear equation system.

1.3   Exercises

1. Use program *stp* to retrieve waveforms of seismic station TAB from a M4.4 earthquake on Aug. 20, 1998, near the San Andreas Fault (event CUSP ID 9064568).

2. According to documentation (see www.data.scec.org/stations/seed/dl_seed.php), channel HHZ is from a Guralp CMG-40T sensor and channel HLZ is from a FBA-23 sensor. Remove instrumental responses in these two channels to obtain vertical displacement waveform at TAB.

3. Plot and compare the displacement waveforms from these two sensors.

Chapter 2

Seismic Sources

2.1 Seismic sources

2.1.1 Seismic source representation

Earthquakes and other indigenous sources can be considered to be the result of a *local-ized, transient failure of the linearized elastic constitutive relation*. We define the difference between the true stress and the modeled stress as the *stress glut*

$$\mathbf{S} = \mathbf{T}^{model} - \mathbf{T}^{true}. \tag{2.1}$$

The equation of motion

$$\rho \frac{\partial^2 \mathbf{u}}{\partial t^2} = \nabla \cdot \mathbf{T}^{true}, \tag{2.2}$$

can be re-written as

$$\rho \frac{\partial^2 \mathbf{u}}{\partial t^2} = \nabla \cdot \mathbf{T}^{model} + \mathbf{f}, \tag{2.3}$$

where $\mathbf{f}$ is the seismic source term and is called the *equivalent body force*:

$$\mathbf{f} = -\nabla \cdot \mathbf{S}. \tag{2.4}$$

It can be shown that the net force and torque of $\mathbf{f}$ in V are zero.

The seismic moment tensor of the source is defined as

$$M_{ij} = \int_V f_i x_j \mathrm{d}V = \int_V S_{ij} \mathrm{d}V, \tag{2.5}$$

which is a symmetric tensor. Its diagonal elements correspond to force dipoles and off-diagonal elements correspond to force couples (Fig. 2.1).
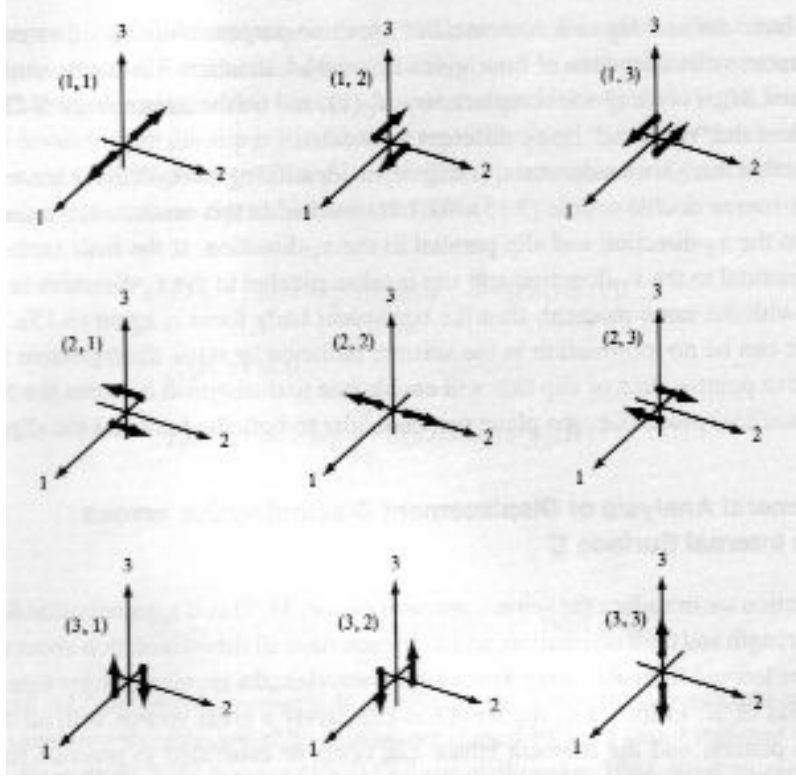
Figure 2.1: Moment tensor elements and their corresponding force dipoles and couples (from Aki and Richards [1980]).

The scalar moment of the source is defined using the norm of the tensor:

$$M_0 \equiv \frac{1}{\sqrt{2}}\sqrt{M_{ij}M_{ij}}. \tag{2.6}$$

The factor $\sqrt{2}$ was introduced for historical compatibility (see below).

2.1.2   Ideal fault

An *ideal fault* is a surface Σ embedded within V across which there is a tangential slip discontinuity $\Delta\mathbf{u}$. So

$$\Delta\mathbf{u} \cdot \hat{\mathrm{n}} = 0. \tag{2.7}$$

It can be shown that the stress glut is zero everywhere except on Σ:

$$\mathbf{S} = \mathbf{m}\delta_\Sigma, \tag{2.8}$$

where $\mathbf{m} = \mathbf{C} : \hat{\mathrm{n}}\Delta\mathbf{u}$ is the stress-glut density. For an isotropic Earth model:

$$\mathbf{m} = \mu\Delta u(\hat{\mathrm{n}}\hat{\mathrm{v}} + \hat{\mathrm{v}}\hat{\mathrm{n}}), \tag{2.9}$$
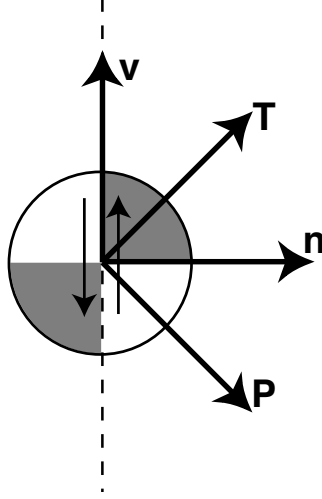
Figure 2.2: P and T axes of a double couple moment tensor.

which can be shown graphically equivalent to two force couples (double-couple, or DC). The scalar moment of the source with a fault area of A is

$$M_0 = \mu \Delta u A. \tag{2.10}$$

A double-couple moment tensor has three eigenvalues: $\pm M_0, 0$. The three eigenvectors

$$\hat{T} = \frac{1}{\sqrt{2}}(\hat{n} + \hat{v}), \tag{2.11}$$

$$\hat{P} = \frac{1}{\sqrt{2}}(\hat{n} - \hat{v}), \tag{2.12}$$

$$\hat{N} = \hat{n} \times \hat{v}, \tag{2.13}$$

are called the tension axis (T-axis, corresponding to M_0), the pressure axis (P-axis, corresponding to $-M_0$), and the null axis (N-axis, corresponding to 0), respectively. Note that the T-axis is located in the compressional quadrants of the focal sphere and the P-axis is located in the dilatational quadrants (Fig. 2.2). They are *not* principal stress axes.

2.1.3 Decompositions of a general moment tensor

A general moment tensor can be decomposed into an isotropic tensor and a deviatoric tensor:

$$M_{ij} = \frac{1}{3}tr(\mathbf{M})\delta_{ij} + M'_{ij} = \sqrt{2}M_0 \left(\zeta I_{ij} + \sqrt{1 - \zeta^2} D_{ij} \right), \tag{2.14}$$

where

$$I_{ij} = \frac{1}{\sqrt{3}}\delta_{ij}, \tag{2.15}$$

is the normalized isotropic tensor and D_{ij} is a normalized deviatoric tensor.

$$\zeta = \frac{tr(\mathbf{M})}{\sqrt{6}M_0}, \tag{2.16}$$

is a dimensionless parameter ranging from -1 to 1 that quantifies the relative strength of the istropoic component.

Next we decompose D_{ij} into double-couple and CLVD components. The CLVD has a dipole of magnitude 2 in its symmetry axis compensated by two unit dipoles in the orthogonal directions [Knopoff and Randall, 1970]. Let λ_1 be the largest eigenvalue (corresponding to the T-axis eigenvector $\hat{T}$) of the deviatoric tensor D_{ij}, λ_2 be the intermediate eigenvalue (corresponding to the null-axis eigenvector $\hat{N}$), and λ_3 the smallest eigenvalue (corresponding to the P-axis eigenvector $\hat{P}$), i.e.,

$$\lambda_1 \geq \lambda_2 \geq \lambda_3. \tag{2.17}$$

Note that all λ_i's are dimensionless and satisfy the conditions

$$\lambda_1 + \lambda_2 + \lambda_3 = 0, \tag{2.18}$$
$$\lambda_1^2 + \lambda_2^2 + \lambda_3^2 = 1. \tag{2.19}$$

Using (2.17)–(2.19), we get

$$\max(\lambda_2) = \min(\lambda_1) = \frac{1}{\sqrt{6}}, \tag{2.20}$$

$$\min(\lambda_2) = \max(\lambda_3) = -\frac{1}{\sqrt{6}}. \tag{2.21}$$

When $\lambda_2 = 0$ the deviatoric tensor D_{ij} is a pure double-couple.

As mentioned, the DC-CLVD decomposition is not unique as the CLVD symmetry axis can be aligned with any of the principal axes [e.g. Jost and Herrmann, 1989, Hudson et al., 1989]. Here we align the CLVD symmetry axis with the N-axis [e.g. Chapman and Leaney, 2011]:

$$\begin{aligned} D_{ij} &= \lambda_1 T_i T_j + \lambda_2 N_i N_j + \lambda_3 P_i P_j \\ &= \frac{\lambda_1 - \lambda_3}{\sqrt{2}} D_{ij}^{\mathrm{DC}} + \sqrt{\frac{3}{2}} \lambda_2 D_{ij}^{\mathrm{CLVD}}, \end{aligned} \tag{2.22}$$

where

$$D_{ij}^{\mathrm{DC}} = \frac{1}{\sqrt{2}}(T_i T_j - P_i P_j), \tag{2.23}$$

$$D_{ij}^{\mathrm{CLVD}} = \frac{1}{\sqrt{6}}(2N_i N_j - T_i T_j - P_i P_j), \tag{2.24}$$

are normalized DC and CLVD tensors. The above decomposition has the attractive property that the DC and CLVD basic sources are orthogonal

$$D_{ij}^{\mathrm{DC}} D_{ij}^{\mathrm{CLVD}} = 0. \tag{2.25}$$

8

The strength of the CLVD component can be quantified by the dimensionless parameter

$$\chi = \sqrt{\frac{3}{2}}\lambda_2. \tag{2.26}$$

It can be shown from (2.20) and (2.21) that $\frac{1}{2} \geq \chi \geq -\frac{1}{2}$.

Therefore, one way to parameterize a general moment tensor in terms of the basic isotropic, double couple, and CLVD sources while preserving the total scalar moment is

$$M_{ij} = \sqrt{2}M_0\left(\zeta I_{ij} + \sqrt{1-\zeta^2}\left(\sqrt{1-\chi^2}D_{ij}^{\mathrm{DC}} + \chi D_{ij}^{\mathrm{CLVD}}\right)\right). \tag{2.27}$$

The relative strength of each part can be measured by the ratio of its scalar moment to the total moment:

$$\Lambda^{\mathrm{ISO}} = \mathrm{sgn}(\zeta)\zeta^2, \tag{2.28}$$
$$\Lambda^{\mathrm{DC}} = (1-\zeta^2)(1-\chi^2), \tag{2.29}$$
$$\Lambda^{\mathrm{CLVD}} = \mathrm{sgn}(\chi)(1-\zeta^2)\chi^2, \tag{2.30}$$

such that

$$|\Lambda^{\mathrm{ISO}}| + \Lambda^{\mathrm{DC}} + |\Lambda^{\mathrm{CLVD}}| = 1. \tag{2.31}$$

Note that in this decomposition the maximum CLVD is 25% (at $\zeta = 0$ and $\chi = \pm 1/2$) (Fig. 2.1.3).

2.1.4 DC moment tensor components

With x-axis to the North, y-axis to the East, and z-axis down,

$$\hat{\mathrm{n}} = (-\sin\delta\sin\phi, \sin\delta\cos\phi, -\cos\delta)^T, \tag{2.32}$$
$$\hat{\mathrm{v}} = (\cos\lambda\cos\phi + \sin\lambda\cos\delta\sin\phi, \cos\lambda\sin\phi - \sin\lambda\cos\delta\cos\phi, -\sin\lambda\sin\delta)^T, \tag{2.33}$$

where ϕ is the fault strike measured from the North, δ is the fault dip measured from the horizontal, and λ is the slip direction (rake angle) measured CCW from the fault strike direction. For DC (see A&R, P112):

$$M_{xx} = -(\sin\delta\cos\lambda\sin 2\phi + \sin 2\delta\sin\lambda\sin^2\phi), \tag{2.34}$$

$$M_{xy} = \sin\delta\cos\lambda\cos 2\phi + \frac{1}{2}\sin 2\delta\sin\lambda\sin 2\phi, \tag{2.35}$$

$$M_{xz} = -(\cos\delta\cos\lambda\cos\phi + \cos 2\delta\sin\lambda\sin\phi), \tag{2.36}$$

$$M_{yy} = \sin\delta\cos\lambda\sin 2\phi - \sin 2\delta\sin\lambda\cos^2\phi, \tag{2.37}$$

$$M_{yz} = -(\cos\delta\cos\lambda\sin\phi - \cos 2\delta\sin\lambda\cos\phi), \tag{2.38}$$

$$M_{zz} = \sin 2\delta\sin\lambda. \tag{2.39}$$
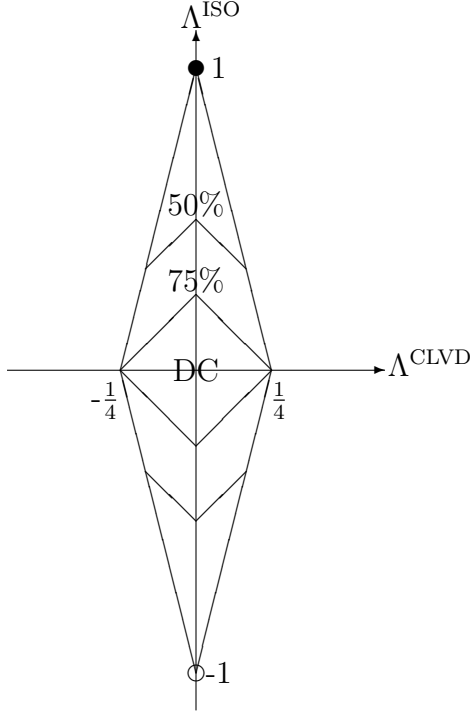
Figure 2.3: The ISO-DC-CLVD diagram showing permissible values of the Λ^{ISO}, Λ^{CLVD}, and Λ^{DC} percentages as bounded by the outer diamond. The pure explosion and implosion sources are indicated by the circles. The pure DC source is located at the center. The contours show DC levels of 75% and 50%.

2.2 Displacements produced by a point source in a whole-space

2.2.1 A single-force source

The displacement in a uniform whole-space produced by a single force F_p at the origin (Fig. 2.4) is

$$u_i(\mathbf{r}, t) = \frac{3\gamma_i\gamma_p - \delta_{ip}}{4\pi\rho r^3} \int_{r/\alpha}^{r/\beta} \tau F_p(t - \tau)\mathrm{d}\tau + \frac{\gamma_i\gamma_p}{4\pi\rho\alpha^2 r}F_p(t - \frac{r}{\alpha}) + \frac{\delta_{ip} - \gamma_i\gamma_p}{4\pi\rho\beta^2 r}F_p(t - \frac{r}{\beta}), \quad (2.40)$$

where $\gamma_i = \frac{x_i}{r}$ is the i-th component of the unit vector $\hat{\mathbf{r}}$. This is one of the most important solutions in seismology and was first given by Stokes in 1849. The first term of RHS is called the near field because it decays with distant rapidly. The other two terms are called the far-field P and S wave-fields respectively. When the source time function is an impulse, the far-field P and S waveforms are impulsive but the near-field waveform is a ramp starting at the P arrival time and ending at the S arrival time (Fig. 2.4).

If we set up a spherical coordinate system (r,θ,ϕ) with the symmetry axis aligned with the
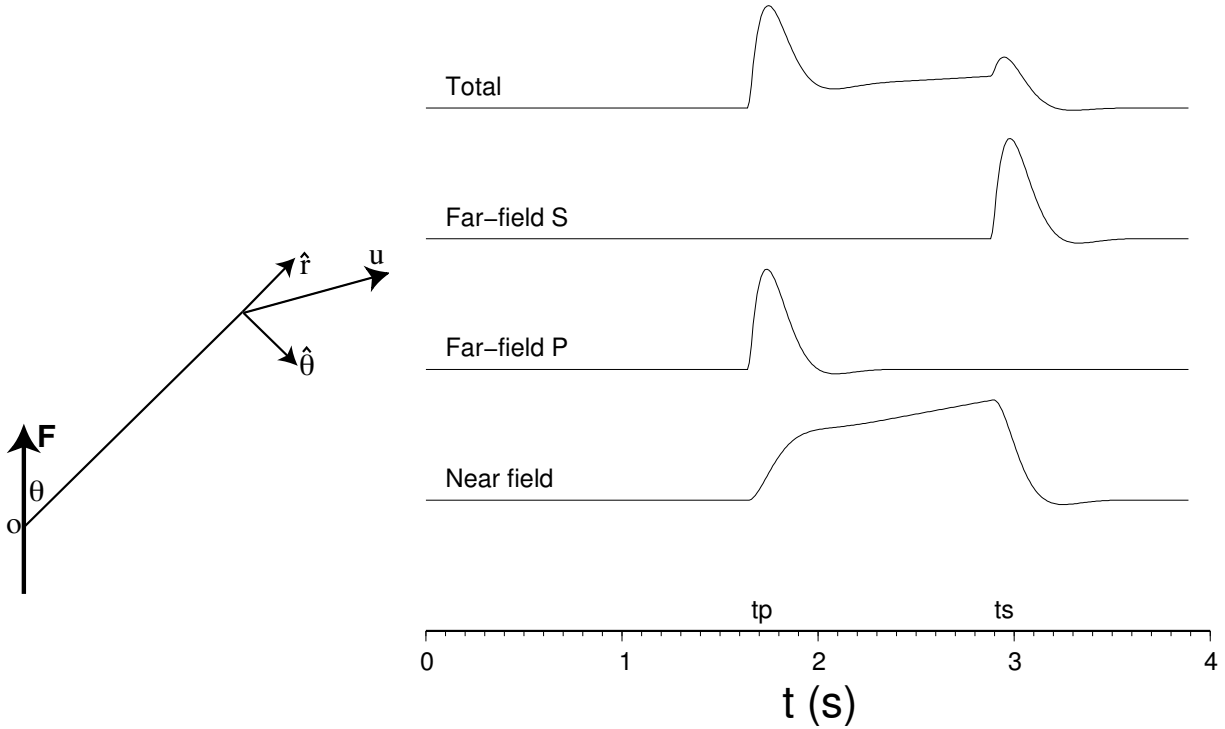
Figure 2.4: Displacement **u** from a single force **F** in a whole-space. Waveform shapes of the near field, far-field P, and far-field S are shown on the right.

single force direction (see Fig. 2.4), the directional variations of far-field P and S displacement amplitudes can be written as

$$\mathbf{A}^P = \cos\theta\hat{\mathrm{r}} \tag{2.41}$$
$$\mathbf{A}^S = -\sin\theta\hat{\theta}. \tag{2.42}$$

It is clear that the particle motion of the far-field P is parallel to $\hat{\mathrm{r}}$, i.e., the propagation direction, as expected. Its amplitude varies with direction as $\cos\theta$. The particle motion of the far-field S is perpendicular to the propagation direction and its amplitude varies with direction as $\sin\theta$. The P- and S-wave source radiation patterns are illustrated in Fig. 2.5.

11
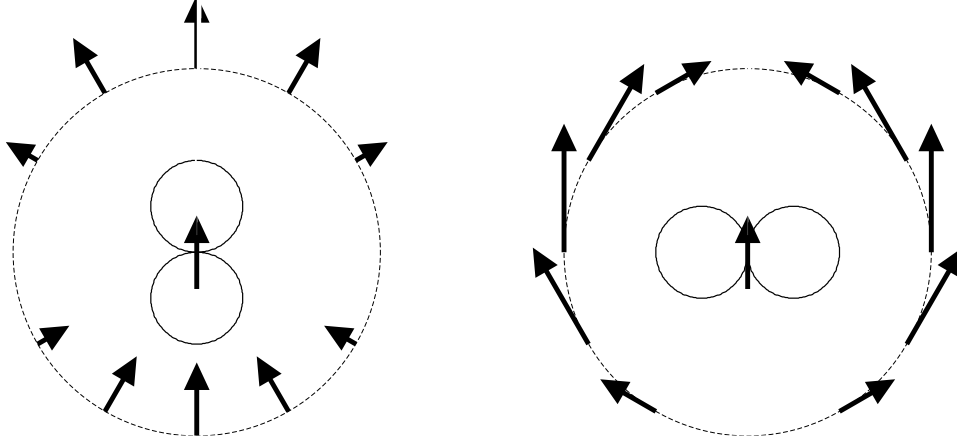
Figure 2.5: Radiation patterns and particle motions of far-field P (left) and S from a single force.

2.2.2 A general moment tensor source

The displacement from a general moment tensor source M_{pq} in a uniform whole-space can be derived from the displacement solution of a single force [Aki and Richards, 1980, Eq. 4.29]:

$$
\begin{aligned}
u_i(\mathbf{r}, t) = &\frac{1}{4\pi\rho r^4}(15\gamma_i\gamma_p\gamma_q - 3\gamma_i\delta_{pq} - 6\gamma_p\delta_{iq})\int_{r/\alpha}^{r/\beta}\tau M_{pq}(t-\tau)\mathrm{d}\tau \\
&+\frac{1}{4\pi\rho\alpha^2 r^2}(6\gamma_i\gamma_p\gamma_q - \gamma_i\delta_{pq} - 2\gamma_p\delta_{iq})M_{pq}(t-\frac{r}{\alpha}) \\
&-\frac{1}{4\pi\rho\beta^2 r^2}(6\gamma_i\gamma_p\gamma_q - \gamma_i\delta_{pq} - 3\gamma_p\delta_{iq})M_{pq}(t-\frac{r}{\beta}) \\
&+\frac{1}{4\pi\rho\alpha^3 r}\gamma_i\gamma_p\gamma_q\dot{M}_{pq}(t-\frac{r}{\alpha}) \\
&+\frac{1}{4\pi\rho\beta^3 r}(\delta_{ip} - \gamma_i\gamma_p)\gamma_q\dot{M}_{pq}(t-\frac{r}{\beta}).
\end{aligned}
\tag{2.43}
$$

In addition to the near-field term (the first term on RHS) and the far-field terms (the last two terms on RHS), there are two intermediate-field terms that decay as $\frac{1}{r^2}$.

Assuming that M_{pq} is a pure double couple in the (x_1, x_3) plane and setting up a spherical coordinate system (r, θ, ϕ) with the x_3-axis as the symmetry axis (Fig. 2.6), we can express the directional variation of far-field P and S displacement amplitudes [Aki and Richards, 1980, Eq. 4.33]

$$
\begin{aligned}
\mathbf{A}^P &= \sin 2\theta \cos \phi \hat{\mathbf{r}} & (2.44) \\
\mathbf{A}^S &= \cos 2\theta \cos \phi \hat{\theta} - \cos \theta \sin \phi \hat{\phi}. & (2.45)
\end{aligned}
$$

These radiation patterns in the 1-3 plane are illustrated in Fig. 2.7.

12
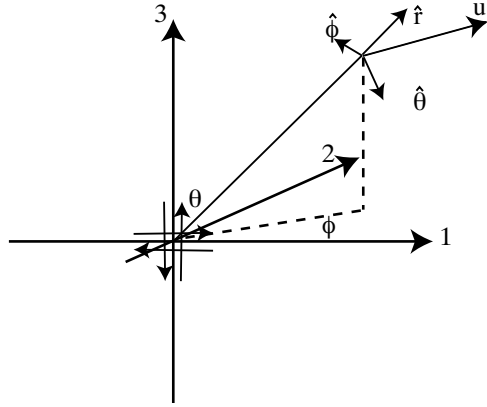
Figure 2.6: Displacement **u** produced by a double couple in the x_1-x_3 plane.
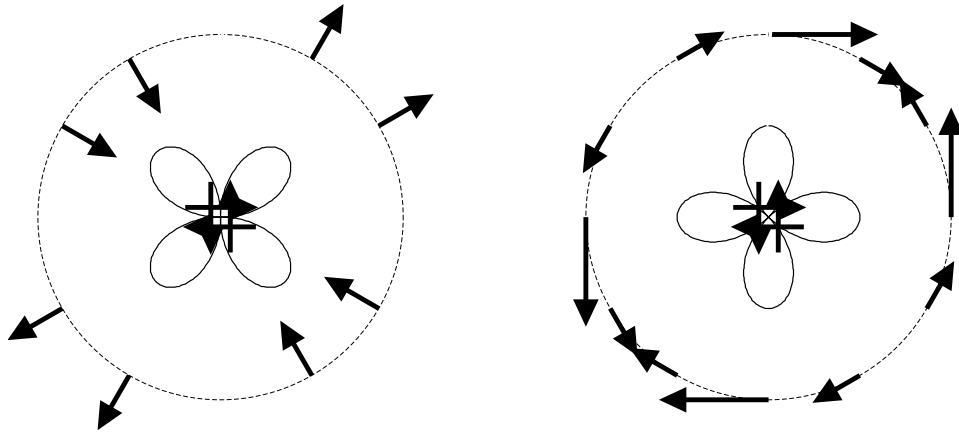
Figure 2.7: Radiation patterns and particle motions of far-field P (left) and S from a double couple.

2.2.3   Examples

Fig. 2.8 shows vertical acceleration recorded by TriNet station TAB from a nearby M_w 4.2 earthquake near the San Andreas fault in California. The earthquake is 11 km deep and about 3 km from the station. The obtained displacement using double integrations show significant near-field between the P and S phases and permanent displacement after the S. They are matched well by the whole-space solution prediction.

Near-field and permanent displacement have also been observed at regional distances from large deep earthquakes such as the 1994 Bolivia deep earthquake (Fig. 2.9). Vidale et al. [1995] reported an observation of the near-field of the Bolivia earthquake at stations in southern California (7,500 km away) (Fig. 2.10).
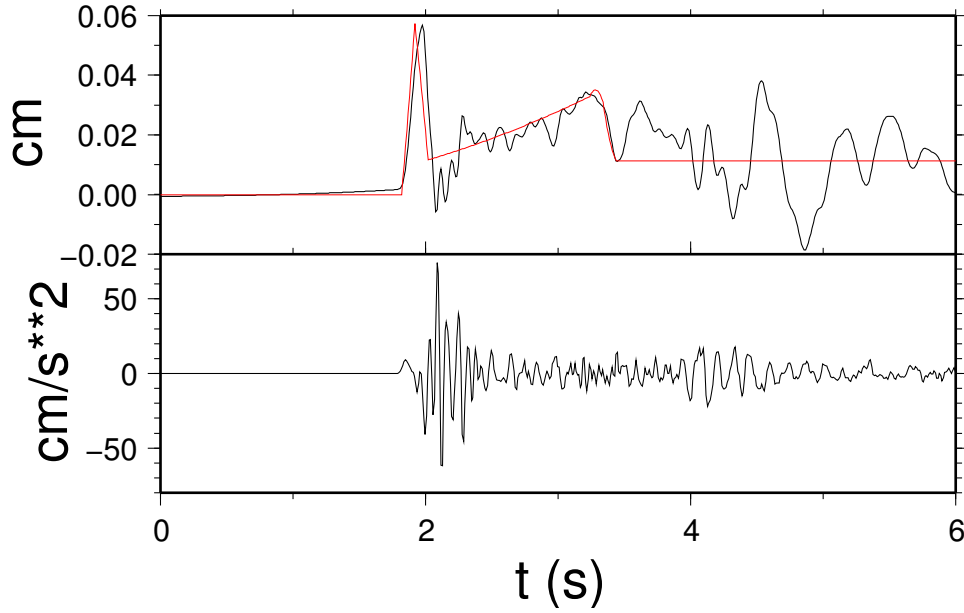
Figure 2.8: The bottom trace is the vertical-component acceleration recorded by TriNet station TAB from a nearby M_w 4.2 earthquake (3 km away and at a depth of 11 km). The top trace in black is the obtained displacement waveforms using double integration. The red-colored trace is synthetic displacement using the whole-space solution (multiplied by 2 to account for the free-surface effect).

2.3   Exercises

A sample Matlab program for computing displacement generated by a single force in a whole space is given below:

```
%%%%%%%%%%%%%%%%%%%%%%%%%%%%%%%%%%%%%%%%%%%%%%%%%%%%%%%%%%%%%%%%%%%%%%%%%
% computing displacements genenerated by a single force in a whole
% space.
%%%%%%%%%%%%%%%%%%%%%%%%%%%%%%%%%%%%%%%%%%%%%%%%%%%%%%%%%%%%%%%%%%%%%%%
clear;
addpath /home/lupei/Src/sac_msc

% model parameters of the whole-space
vp = 6.3;
vs = 3.6;

% sampling rate
dt = 0.01;

% force vector
```

14
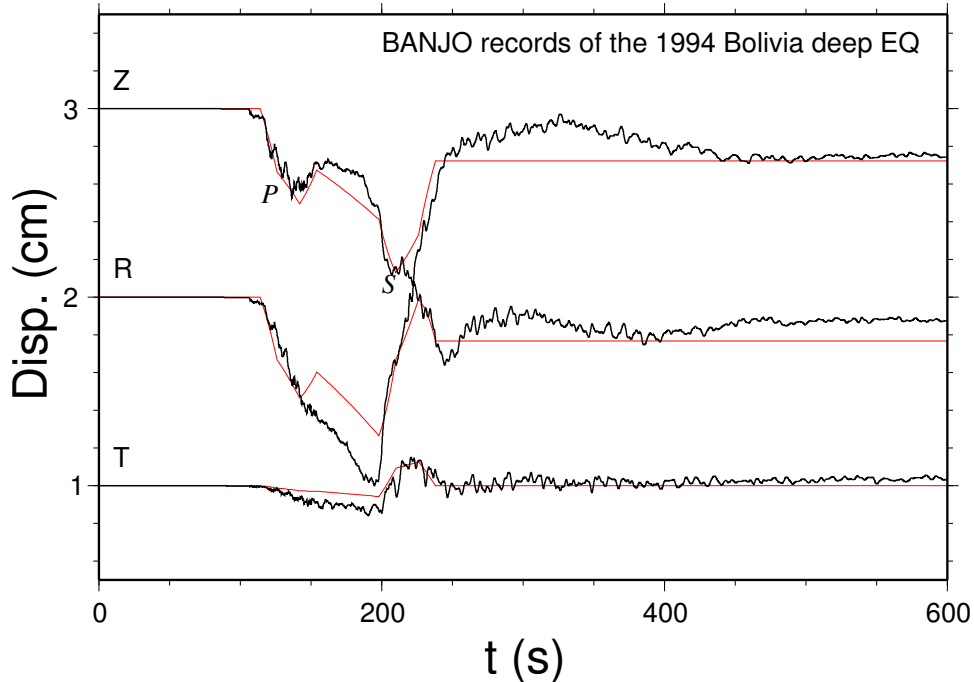
Figure 2.9: Black-colored traces are three-component displacement waveforms recorded at the BANJO array from the 1994 Mw 8.3 Bolivia deep earthquake (from Zhu [2003]). Red-colored traces are synthetic displacements using the whole-space solution (multiplied by 2 to account for the free-surface effect).

```
F = [0; 0; 1];

% receiver location
r = [3; 0; 10];

% compute the amplitudes of the nearfield and far-fields
dist = norm(r);
gamma = r/dist;
gammaDotF = gamma'*F;
AnearField = (3*gammaDotF*gamma-F)/(dist*dist*dist);
AfarP = gamma*(gammaDotF/(vp*vp*dist));
AfarS = (F-gammaDotF*gamma)/(vs*vs*dist);

% construct the time functions of the nearfield and far-fields
tp = dist/vp;
itp = round(tp/dt);
ts = dist/vs;
its = round(ts/dt);
nt = its + 100;
t = (0:nt-1)*dt;
```

15

June 9, 1994 Bolivian earthquake:
stack of 22 Californian P waves
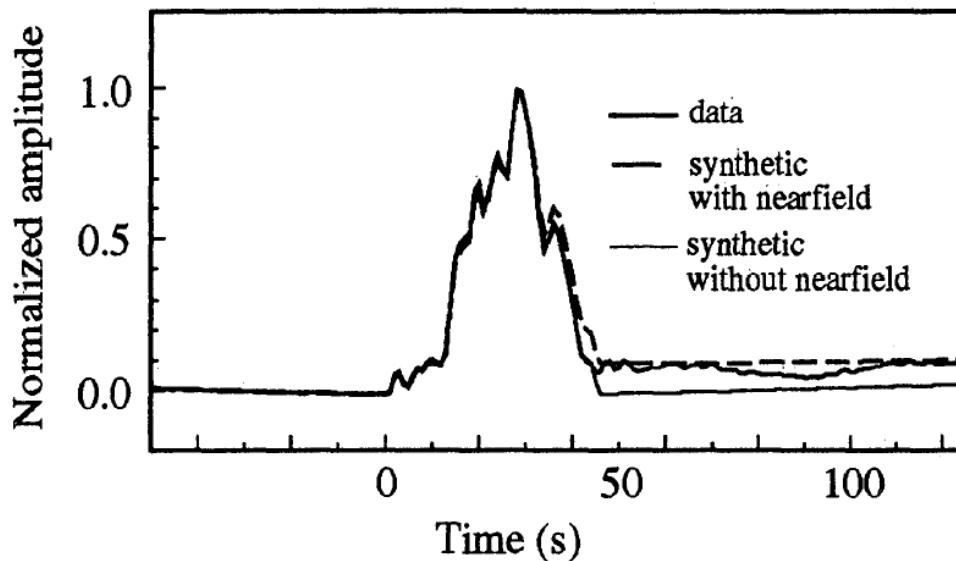
Figure 2.10: Observation of near field at teleseismic distances from the 1994 Bolivia deep earthquake (from Vidale et al. [1995]).

```
nearField = zeros(3,nt);
farP = zeros(3,nt);
farS = zeros(3,nt);
nearField(:,itp:its) = AnearField*t(itp:its);
farP(:,itp) = AfarP/dt;
farS(:,its) = AfarS/dt;
disp = nearField + farP + farS;

subplot(4,1,1),plot(t,nearField(3,:))
subplot(4,1,2),plot(t,farP(3,:))
subplot(4,1,3),plot(t,farS(3,:))
subplot(4,1,4),plot(t,disp(3,:))

% save
compnm = 'xyz';
hd = newhdr(nt,dt,0.);
for comp=1:3
  wtSac(['nf.' compnm(comp)], hd, nearField(comp,:));
  wtSac(['fp.' compnm(comp)], hd, farP(comp,:));
  wtSac(['fs.' compnm(comp)], hd, farS(comp,:));
end
```

%%%

A low-pass filtered version of the waveforms is shown in Fig. 2.4.

1. Write a computer program to calculate displacement field produced by a moment tensor in a whole-space using (2.43). You should assume that the time history of the source is a step function.

2. TriNet station TAB recorded a magnitude 4.4 earthquake about 3 km away on Aug. 20, 1998. According to waveform inversion, the event is located at a depth of 11 km and its moment tensor elements are Mxx=-2.243, Mxy=-0.749, Mxz=-0.383, Myy=-0.226, Myz= 0.118, Mzz= 2.469, with a scale of 10^{22} dyne-cm, here the x-axis is pointing north, y east, and z downward. Use your program to compute and plot the vertical displacement waveform of each individual field and the total field. Compare the synthetics with the observation obtained in Exe. 1.3 to find the appropriate V_p, V_s, and source rupture duration.

3. Use your program to model the displacement waveforms recorded at a BANJO station from the 1994 Bolivia deep earthquake (shown in Fig. 2.9). The station's epicentral distance is 5.76°and the azimuth is 181.53°. The Harvard CMT solution is Mxx=7.75, Mxy=-2.48, Mxz=-25.3, Myy=-0.16, Myz= 0.42, Mzz=-7.59, with a scale of 10^{27} dyne-cm, here the x-axis is pointing south, y east, and z up. The depth of the event after the Earth-flattening approximation is 682 km.

4. A strike-slip earthquake at 2 km depth ruptured a N-S oriented vertical plane of 6 km long and 2 km wide with a slip of 1 m. What is the moment magnitude of the earthquake (assumming that the rigidity is 30 GPa)? Modify your program to compute and plot horizontal permanent displacement field at the surface within 10 km from the epicenter. You need to divide the ruptured fault into small subfaults and sum up the contribution from each point source.

Chapter 3

Multi-layered Media − Generalized Ray Theory

3.1 Solution to wave equation in cylindrical coordinate system

In cylindrical coordinates (r,θ,z) with the z-axis downward, the wave equation in the Laplace domain is:

$$\frac{1}{r}\frac{\partial}{\partial r}\left(r\frac{\partial \phi}{\partial r}\right) + \frac{1}{r^2}\frac{\partial^2 \phi}{\partial \theta^2} + \frac{\partial^2 \phi}{\partial z^2} - \frac{s^2}{c^2}\phi = 0. \tag{3.1}$$

Using the variable separation method, the general solution from a point source at the origin in a whole-space can be found as

$$\phi(r, \theta, z, s) = \sum_{n=0,\pm 1,\cdots} e^{-in\theta} \int_0^\infty A_n(k)J_n(kr)e^{-\nu|z|}dk, \tag{3.2}$$

where

$$\nu = \sqrt{k^2 + \frac{s^2}{c^2}}, \qquad\qquad \Re\nu > 0, \tag{3.3}$$

and A_n is to be determined by initial conditions (i.e., the seismic source).

For example, the displacement field from an explosion source with a step source time function can be derived using (2.43) as

$$\mathbf{u}(r, z, t) = \nabla\phi = \frac{M_0}{4\pi\rho c^2}\left(\frac{H(t - R/c)}{R^2} + \frac{\dot{H}(t - R/c)}{cR}\right)\hat{\mathrm{R}}, \tag{3.4}$$

where $R = \sqrt{z^2 + r^2}$. So

$$\phi(r, z, t) = -\frac{M_0}{4\pi\rho c^2}\frac{H(t - R/c)}{R}. \tag{3.5}$$

By taking the Laplace transform and using the Somerfield integral,

$$\phi(r,z,s) = -\frac{M_0}{4\pi\rho c^2}\frac{1}{s}\frac{e^{-sR/c}}{R} = -\frac{M_0}{4\pi\rho c^2}\frac{1}{s}\int \frac{k}{\nu}J_0(kr)e^{-\nu|z|}dk, \tag{3.6}$$

i.e, the only non-zero term in (3.2) is $n=0$:

$$A_0 = -\frac{M_0}{4\pi\rho c^2}\frac{1}{s}\frac{k}{\nu}. \tag{3.7}$$

3.2   A liquid whole-space

Let us consider an explosion source with a step source time function in a liquid whole-space. To get the time-domain solution for pressure $\phi(t)$, one needs to evaluate two integrals: one for k (without $-\frac{M_0}{4\pi\rho c^2}$)

$$\phi(s) = \frac{1}{s}\int_0^\infty \frac{k}{\nu}J_0(kr)e^{-\nu|z|}dk, \tag{3.8}$$

and another for the inverse Laplace transform of $\phi(s)$.

A technique call the Cagniard-de Hoop method can be used to evaluate the double integrations at once. By variable substitution $k = -isp$ and using

$$J_0(-ispr) = \frac{i}{\pi}\left(K_0(spr) - K_0(-spr)\right), \tag{3.9}$$

(3.8) becomes

$$\phi(s) = -\frac{i}{\pi}\int_{-i\infty}^{i\infty}\frac{p}{\eta}K_0(spr)e^{-s\eta|z|}dp = \frac{2}{\pi}\Im\int_0^{i\infty}\frac{p}{\eta}K_0(spr)e^{-s\eta|z|}dp, \tag{3.10}$$

where

$$\eta = \sqrt{\frac{1}{c^2} - p^2}. \tag{3.11}$$

At large x,

$$K_n(x) = \sqrt{\frac{\pi}{2x}}e^{-x}\left(1 + \frac{4n^2-1}{8x} + \frac{(4n^2-1)(4n^2-9)}{2(8x)^2} + \cdots\right). \tag{3.12}$$

So, (3.10) becomes (only the first term is kept for simplicity)

$$\phi(s) = \sqrt{\frac{2}{\pi rs}}\Im\int_0^{i\infty}\frac{\sqrt{p}}{\eta}e^{-s(pr+\eta|z|)}dp. \tag{3.13}$$

It looks very much like a Laplace transform when we introduce

$$t = pr + \eta|z|, \tag{3.14}$$

19
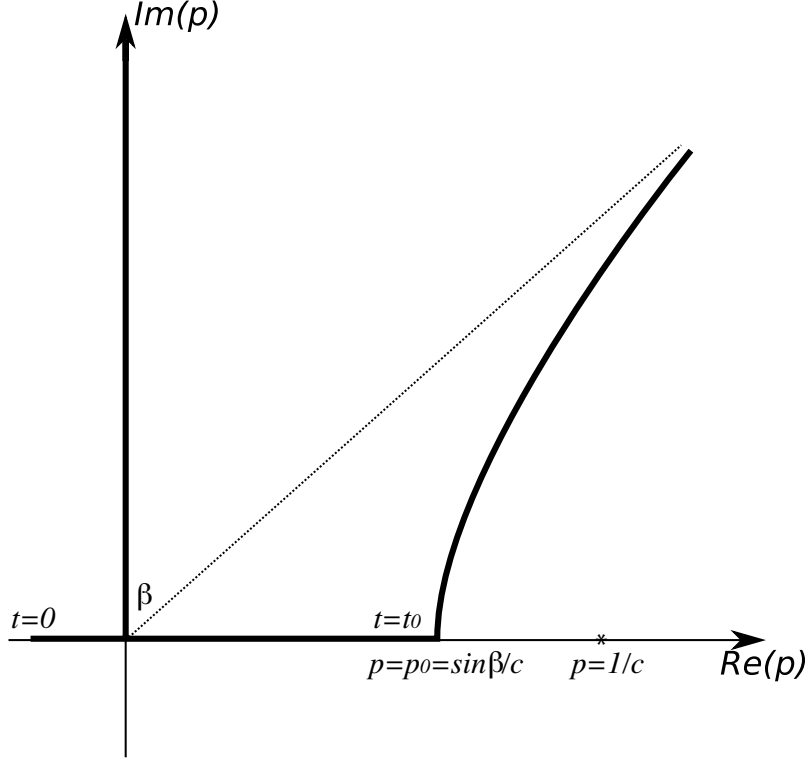
Figure 3.1: Cagniard-de Hoop contour.

and require that t be real. The corresponding

$$
p(t) = \begin{cases} \dfrac{rt}{R^2} - \dfrac{\sqrt{t_0^2 - t^2}}{R^2}|z|, & t < t_0, \\[2ex] \dfrac{rt}{R^2} + \mathrm{i}\dfrac{\sqrt{t^2 - t_0^2}}{R^2}|z|, & t > t_0, \end{cases} \tag{3.15}
$$

where $R = \sqrt{r^2 + z^2}$ and $t_0 = \frac{R}{c}$. The above contour in the complex p-plane, called the Cagniard-de Hoop contour, is show in Fig. 3.1. Because the integrant function is analytical except along the real p axis for $p > \frac{1}{c}$, the integration path $[0, \mathrm{i}\infty]$ can be changed to along the Cagniard-de Hoop contour and

$$
J(t) = \mathcal{L}^{-1}\left\{\Im \int_0^{\mathrm{i}\infty} \frac{\sqrt{p}}{\eta} \mathrm{e}^{-s(pr + \eta|z|)} \mathrm{d}p\right\} = \Im\left\{\frac{\sqrt{p}}{\eta}\frac{\mathrm{d}p}{\mathrm{d}t}\right\}. \tag{3.16}
$$

So, the final solution for the pressure

$$
\phi(t) = \frac{1}{\pi}\sqrt{\frac{2}{r}}\frac{1}{\sqrt{t}} * J(t). \tag{3.17}
$$

20

Since

$$\frac{\mathrm{d}p}{\mathrm{d}t} = \begin{cases} \dfrac{\eta}{\sqrt{t_0^2 - t^2}}, & t < t_0, \\[4mm] \dfrac{\mathrm{i}\eta}{\sqrt{t^2 - t_0^2}}, & t > t_0, \end{cases}$$

(3.18)

the largest contribution to $J(t)$ occurs at time $t = t_0$, which is the first arrival time. Using the asymptotic behavior of $\dfrac{\mathrm{d}p}{\mathrm{d}t}$ near t_0, one can get

$$J(t) = \sqrt{\frac{r}{2}} \frac{H(t - t_0)}{R\sqrt{t - t_0}}.$$

(3.19)

So, the first-motion approximation of the solution

$$\phi(t) = \frac{1}{\pi R} \frac{1}{\sqrt{t}} * \frac{H(t - t_0)}{\sqrt{t - t_0}} = \frac{H(t - t_0)}{R},$$

(3.20)

which is the same as the exact solution.

3.3   Two liquid half-spaces
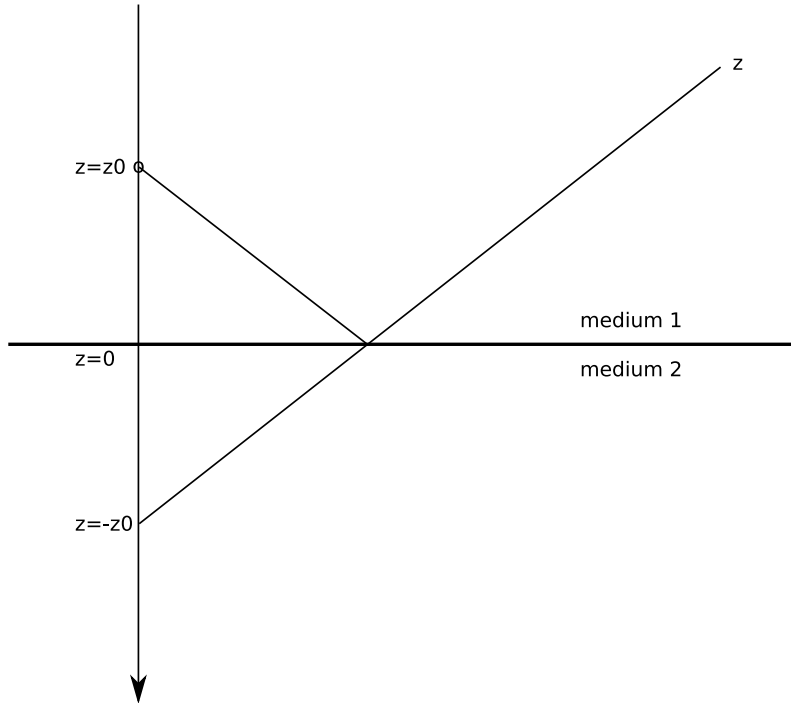
Figure 3.2: Two liquid half-spaces.

21

We now deal with two fluid half-spaces in contact at $z = 0$ (Fig. 3.2). The solution can be found using the general solution and the boundary conditions of ϕ and $\frac{1}{\rho}\frac{\partial \phi}{\partial z}$ continuous,

$$\phi_1(r, z, s) = \sqrt{\frac{2}{\pi r s}} \Im \int_0^{i\infty} \frac{\sqrt{p}}{\eta_1} \left[e^{-s(pr+\eta_1|z-z_0|)} + R_{12}(p)e^{-s(pr+\eta_1|z+z_0|)} \right] dp, \tag{3.21}$$

$$\phi_2(r, z, s) = \sqrt{\frac{2}{\pi r s}} \Im \int_0^{i\infty} \frac{\sqrt{p}}{\eta_1} T_{12}(p)e^{-s(pr+\eta_1|z_0|+\eta_2 z)} dp, \tag{3.22}$$

where

$$R_{12}(p) = \frac{\rho_2\eta_1 - \rho_1\eta_2}{\rho_2\eta_1 + \rho_1\eta_2}, \tag{3.23}$$

$$T_{12}(p) = \frac{2\rho_2\eta_1}{\rho_2\eta_1 + \rho_1\eta_2}, \tag{3.24}$$

are called the reflection and transmission coefficients of the interface, respectively. We recognize that the first term of ϕ_1 is the same as in the whole-space case. It represents the response of the direct wave. The Cagniard contour for the second term is defined by

$$t = pr + \eta_1|z + z_0|. \tag{3.25}$$

Its first-motion arrival time t_0 and p_0 are found to be

$$t_0 = \frac{R}{c_1}, \tag{3.26}$$

$$p_0 = \frac{r}{R}\frac{1}{c_1}, \tag{3.27}$$

where $R = \sqrt{r^2 + (z + z_0)^2}$. They correspond to the arrival time and ray-parameter of a geometrical ray that is reflected from the interface. So, the second term represents the response of the reflected wave.

If $c_2 > c_1$, the reflection coefficient can become complex even when $p < p_0$. This means that $J(t)$ can be non-zero before the arrival time t_0 of the geometrical reflection ray (Fig. 3.3). This non-geometrical arrival time is

$$t_c = \frac{r}{c_2} + \sqrt{\frac{1}{c_1^2} - \frac{1}{c_2^2}}|z + z_0|, \tag{3.28}$$

where is the head-wave arrival time.

Fig. 3.4 shows vertical displacement waveforms in such a two liquid half-space model

22
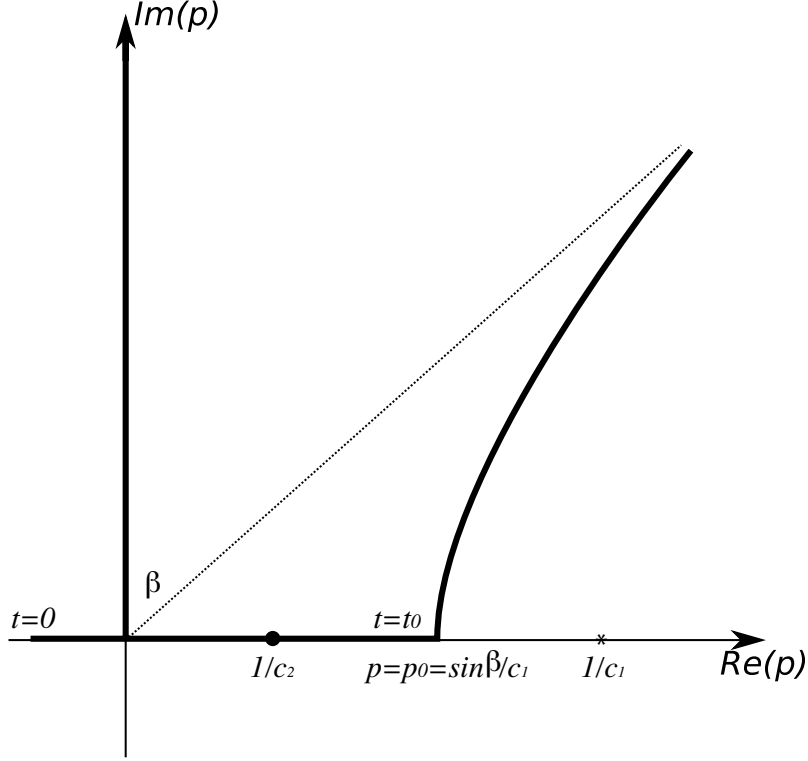
Figure 3.3: Cagniard contour for reflection ray in two liquid half-spaces.

3.4 A sandwiched liquid layer between two liquid half-spaces

If we add a layer of fluid of thickness d between the two half-spaces, the pressure solution in the top liquid is

$$\phi_1(r, z, s) = \sqrt{\frac{2}{\pi r s}} \Im \int_0^{i\infty} \frac{\sqrt{p}}{\eta_1} \left[e^{-s(pr + \eta_1 |z - z_0|)} + A(p) e^{-s(pr + \eta_1 |z + z_0|)} \right] dp, \qquad (3.29)$$

where

$$A(p) = \frac{R_{12} + R_{23} e^{-2s\eta_2 d}}{1 + R_{12} R_{23} e^{-2s\eta_2 d}}. \qquad (3.30)$$

We can use its Taylor expansion

$$A(p) = R_{12} + \sum_{n=1}^{\infty} (-1)^{n+1} R_{12}^{n-1} R_{23}^n (1 - R_{12}^2) e^{-2ns\eta_2 d}. \qquad (3.31)$$

So the pressure can be writtern as

$$\phi_1 = \phi^{direct} + \phi^{reflected} + \sum_{n=1}^{\infty} \phi^n, \qquad (3.32)$$

23
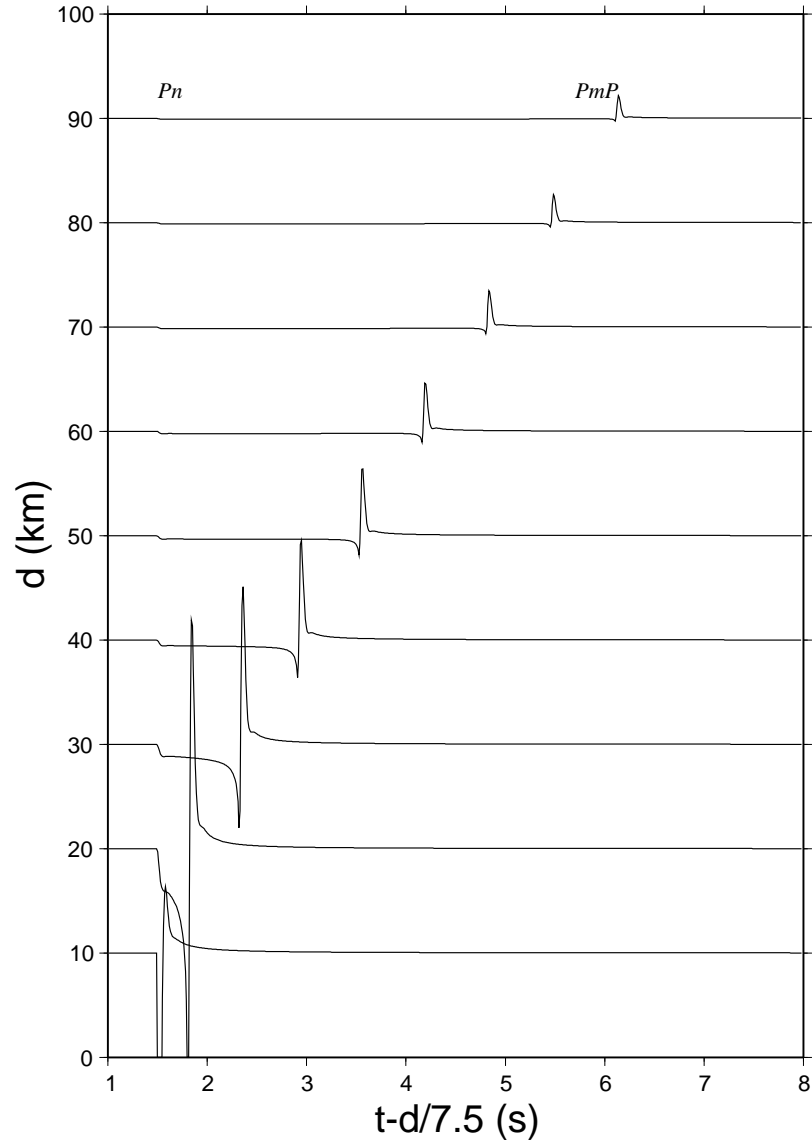
Figure 3.4: Vertical displacements produced by an explosion in a two liquid half-space model, located 5 km above the contact interface. The P velocity in the top half-space is 5 km/s, and 7.5 km/s in the bottom half-space.

where

$$\phi^n = \sqrt{\frac{2}{\pi rs}} \Im \int_0^{i\infty} T_{12}(-R_{12})^{n-1} R_{23}^n T_{21} \frac{\sqrt{p}}{\eta_1} e^{-s(pr+\eta_1|z+z_0|+2n\eta_2 d)} dp. \tag{3.33}$$

It can be recognized that ϕ^n corresponds to a geometrical ray with n-time internal reflections in the liquid layer.

(3.32) means that the full response can be constructed by adding up responses of all possible "rays" from the source to the receiver. The technique is called generalized ray theory. It was first introduced by Spencer [1960].

3.5 Double-couple sources in elastic media

For isotropic elastic media, the displacement field $\mathbf{u}$ satisfies a second-order differential equation:

$$\frac{\partial^2 \mathbf{u}}{\partial t^2} = \frac{1}{\alpha^2} \nabla\nabla \cdot \mathbf{u} - \frac{1}{\beta^2} \nabla \times (\nabla \times \mathbf{u}). \tag{3.34}$$

By using the Helmholtz representation of a vector

$$\mathbf{u} = \nabla\phi + \nabla \times \chi\hat{z} - \frac{1}{sp}\nabla \times (\nabla \times \psi\hat{z}), \tag{3.35}$$

we obtain three wave equations:

$$\nabla^2\phi = \frac{1}{\alpha^2}\frac{\partial^2\phi}{\partial t^2}, \tag{3.36}$$

$$\nabla^2\psi = \frac{1}{\beta^2}\frac{\partial^2\psi}{\partial t^2}, \tag{3.37}$$

$$\nabla^2\chi = \frac{1}{\beta^2}\frac{\partial^2\chi}{\partial t^2}, \tag{3.38}$$

where ϕ is called the P-wave potential, ψ SV potential, and χ SH potential.

For a double-couple source, the non-zero terms in the general solution (3.2) of these potentials are limited to $n \leq 2$:

$$\phi = \frac{M_0}{4\pi\rho}\sum_{n=0}^{2} A_n(\theta,\lambda,\delta)\frac{2}{\pi}\Im\int_0^{i\infty} C_n\frac{p}{\eta_\alpha}K_n(spr)e^{-s\eta_\alpha|z|}dp, \tag{3.39}$$

$$\psi = \frac{M_0}{4\pi\rho}\sum_{n=0}^{2} A_n(\theta,\lambda,\delta)\frac{2}{\pi}\Im\int_0^{i\infty} SV_n\frac{p}{\eta_\beta}K_n(spr)e^{-s\eta_\beta|z|}dp, \tag{3.40}$$

$$\chi = \frac{M_0}{4\pi\rho}\sum_{n=1}^{2} \frac{1}{n}\frac{\partial}{\partial\theta}A_n(\theta,\lambda,\delta)\frac{2}{\pi}\Im\int_0^{i\infty} SH_n\frac{p}{\eta_\beta}K_n(spr)e^{-s\eta_\beta|z|}dp. \tag{3.41}$$

Table 3.1: Vertical radiation coefficients of explosion and single-force sources.

n	Explosion	Single force		
	P	P	SV	SH
0	$-1/\beta^2$	$\epsilon\eta_\alpha$	$-p$	
1		$-p$	$-\epsilon\eta_\beta$	$1/p\beta^2$

A_n's are called horizontal radiation patterns:

$$A_0 = \frac{1}{2}\sin\lambda\sin 2\delta, \tag{3.42}$$

$$A_1 = \cos\lambda\cos\delta\cos\theta - \sin\lambda\cos 2\delta\sin\theta, \tag{3.43}$$

$$A_2 = \cos\lambda\sin\delta\sin 2\theta + \frac{1}{2}\sin\lambda\sin 2\delta\cos 2\theta, \tag{3.44}$$

where δ is the fault dip, λ is the slip direction (rake, measured on the fault plane from the strike direction), and θ is the station azimuth measured from the fault strike direction. Therefore, each individual term in the above potentials without the horizontal radiation coefficients represents response to three fundamental faultings: 45° down-dip slip ($n = 0$ with $\delta = 45°$ and $\lambda = -90°$), vertical dip slip ($n = 1$ with $\delta = 90°$ and $\lambda = -90°$), and vertical strike slip ($n = 2$ with $\delta = 90°$ and $\lambda = 0°$). Their vertical radiation patterns are

$$C_0 = p^2 - 2\eta_\alpha^2 \qquad SV_0 = 3\epsilon p\eta_\beta, \qquad SH_0 = 0, \tag{3.45}$$

$$C_1 = 2\epsilon p\eta_\alpha, \qquad SV_1 = \eta_\beta^2 - p^2, \qquad SH_1 = -\frac{\epsilon}{\beta^2}\frac{\eta_\beta}{p}, \tag{3.46}$$

$$C_2 = -p^2, \qquad SV_2 = -\epsilon p\eta_\beta, \qquad SH_2 = \frac{1}{\beta^2}, \tag{3.47}$$

where

$$\epsilon = \begin{cases} +1, & z > 0, \\ -1, & z < 0. \end{cases}$$

The vertical radiation coefficients for explosion and single force sources are give in Tab. 3.1.

To compute displacement from potentials, one needs to take derivatives of potential with respect to r, θ, and z. In a whole-space (ignoring the near-field terms),

$$u_z = \frac{\partial\phi}{\partial z} + sp\psi = s(-\eta_\alpha\phi + p\psi), \tag{3.48}$$

$$u_r = \frac{\partial\phi}{\partial r} - \frac{1}{sp}\frac{\partial^2\psi}{\partial r\partial z} + \frac{1}{r}\frac{\partial\chi}{\partial\theta} = s(-p\phi - \eta_\beta\psi), \tag{3.49}$$

$$u_\theta = \frac{1}{r}\frac{\partial\phi}{\partial\theta} - \frac{1}{spr}\frac{\partial^2\psi}{\partial\theta\partial z} - \frac{\partial\chi}{\partial r} = sp\chi. \tag{3.50}$$

This means that the displacements can be obtained by multiplying the so-called *receiver functions* to the potentials. The receiver functions of whole-space and half-space are listed in Table 3.2.

26

Table 3.2: Whole-space and half-space receiver functions.

	Whole-space			Half-space		
	P	SV	SH	P	SV	SH
u_z	$-\eta_\alpha$	p		$-2\eta_\alpha(\eta_\beta^2 - p^2)/D$	$4p\eta_\alpha\eta_\beta/D$	
u_r	$-p$	$-\eta_\beta$		$-4p\eta_\alpha\eta_\beta/D$	$-2\eta_\beta(\eta_\beta^2 - p^2)/D$	
u_θ			p			$2p$

$D = \left((\eta_\beta^2 - p^2)^2 + 4p^2\eta_\alpha\eta_\beta\right)\beta^2$ is called the Rayleigh denominator.

The Rayleigh denominator D in the half-space receiver functions is interesting. It has a root at $p \approx 1.1\beta^{-1}$ on the real p axis (called the Rayleigh pole). When the source is shallow, the Cagniard contour is close to the real p axis so that $J(t)$ has large amplitudes at times when the contour is close to the Rayleigh pole. It gives large-amplitude Rayleigh surface waves on the z and r components, with an apparent velocity of 0.9β. An example is shown in Fig. 3.5

The generalized reflection and transmission coefficients across solid-solid and solid-liquid interfaces can be found in Helmberger [1968].
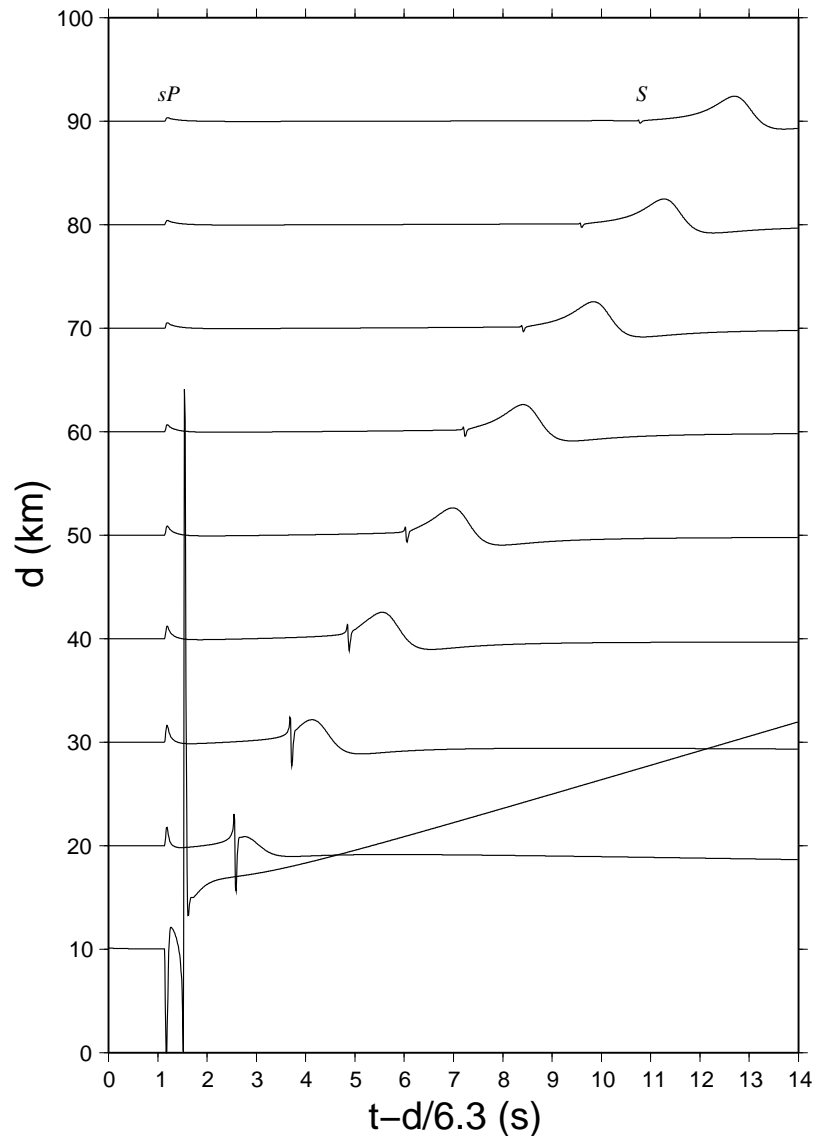
Figure 3.5: Vertical displacements from a strike-slip fault at 5 km depth in a uniform half-space (V_p 6.3 km/s, V_s 3.6 km/s, and ρ 2.7 g/cm^3).

3.6 Exercises

A sample Matlab program for computing the Cagniard-de Hoop coutour and pressure produced by an explosion in a liquid wholespace is given below:

```
%%%%%%%%%%%%%%%%%%%%%%%%%%%%%%%%%%%%%%%%%%%%%%%%%%%%%%%%%%%%%%%%%%%%%%%%%
% computing pressure generated by an explosion in fluid using
% the Cagniard-de Hoop method
%%%%%%%%%%%%%%%%%%%%%%%%%%%%%%%%%%%%%%%%%%%%%%%%%%%%%%%%%%%%%%%%%%%%%%%%%
clear
addpath /home/lupei/Src/sac_msc
% model: a fluid whole space
c=5.0; rho=1.0;
% source depth
h=5;
% receiver location
r=10;
nx = length(r);
z=h;
% time window
dt = 0.01;
n = 700;
nbefore = 100;

scale = -1/(4*pi*rho*c^2);
a = 2*sqrt((0:n-1)/dt); % 2*sqrt(t)
eps = 1.e-8; % small positive imaginary part
for ix=1:nx
  R = sqrt(r(ix)*r(ix)+h^2);
  t0 = R/c;
  t = t0 + dt*(-nbefore:n-nbefore-1)' + 0.5*dt;
  p = (r(ix)/R^2)*t - (z/R^2)*sign(t0-t).*sqrt(t0^2-t.^2)+eps*i;
  eta = sqrt(1/c^2-p.^2);
  % j(t)
  dpdt = sign(t0-t).*eta./sqrt(t0^2-t.^2);
  jt = imag((sqrt(p)./eta).*dpdt);
  % convolve with sqrt(t) and take a derviative
  phi = (scale*sqrt(2./r(ix))/pi)*diff(conv(a,jt));
  hd = newhdr(n-2,dt,t(2));
  hd(51) = r(ix);
  wtSac(['phi.' num2str(r(ix))],hd,phi);
end

% plotting
```

```
subplot(3,1,1);
plot(p,'+');
subplot(3,1,2);
plot(t,jt);
subplot(3,1,3);
plot(t(2:n-1),phi(1:n-2));
```

%%%

1. Write a Matlab program to plot vertical radiation patterns (3.45)-(3.47) as a function of take-off angle.

2. Modify the sample Matlab code above to compute vertical displacements of reflected waves from an explosion source in two liquid half-spaces. Note that the whole space receiver function for u_z is $-s\eta_\alpha$. The source and stations are 5 km above the interface in the top half-space with a P velocity of 5 km/s. The P velocity in the bottom half space is 7.5 km/s. Plot waveform profile from 10 to 100 km in epicentral distances.

3. Use the GRT program *aser* to repeat the above computation and compare the results. Note that the GRT outputs are impulse responses and need to be integrated to get the step responses in order to compare with the Matlab results. A sample GRT input is given below:

```
n # debug
n # Q individual rays
3 # number of terms for the Bessel function expansion
0.01 800 # dt and nt
2 # sample rate of the Cagniard contour, 0=FM
3 # number of layers in the model
  5.0  6.3   3.6   2.786  1000 500 # the 1st layer
  5.0  6.3   3.6   2.786  1000 500 # the 2nd layer
  0.0  8.0   4.5   3.000  1000 500 # the bottom halfspace
2 1 # The source type (0=EX, 1=SF; 2=DC) and source layer (at its top)
rays.file # The name of the ray file
4 # number of distance rangesi, followed by distance t0 name (2f10.3,1x,a80)
      1.000      0.500 grt/01.grn.
      5.000      1.000 grt/05.grn.
     10.000      1.500 grt/10.grn.
     50.000      7.500 grt/50.grn.
  #
  # The ray file looks like this:
  1 # number of rays
  p    2   1p   1p    0.00
  # wave type (p/s/t), number of seg., ray seg specification, ..., shift
```

Chapter 4

Multi-layered Media – Frequency-Wavenumber Integration Method

4.1 Displacement-stress vector in a source-free homogeneous medium

We set up a cylindrical coordinate system $(\mathbf{e}_r, \mathbf{e}_\theta, \mathbf{e}_z)$, with $\mathbf{e}_z$ pointing upward. The displacement in a vertically heterogeneous medium can be expanded in terms of three orthogonal vectors [e.g. Takeuchi and Saito, 1972]:

$$\mathbf{u}(r,\theta,z,t) = \frac{1}{2\,\pi} \sum_{m=0,\pm 1,\cdots} \int e^{-i\,\omega\,t}\,d\omega \int_0^\infty k\,dk \left(U_z \mathbf{R}_m^k + U_r \mathbf{S}_m^k + U_\theta \mathbf{T}_m^k\right), \qquad (4.1)$$

$\mathbf{R}_m^k, \mathbf{S}_m^k, \mathbf{T}_m^k$ are called the surface vector harmonics:

$$\mathbf{R}_m = -Y_m \hat{z}, \qquad (4.2)$$

$$\mathbf{S}_m = \frac{1}{k}\nabla Y_m = \frac{1}{k}\frac{\partial Y_m}{\partial r}\hat{r} + \frac{1}{kr}\frac{\partial Y_m}{\partial \theta}\hat{\theta}, \qquad (4.3)$$

$$\mathbf{T}_m = \mathbf{S}_m \times \hat{z} = \frac{1}{kr}\frac{\partial Y_m}{\partial \theta}\hat{r} - \frac{1}{k}\frac{\partial Y_m}{\partial r}\hat{\theta}, \qquad (4.4)$$

where

$$Y_m(r,\theta) = J_m(kr)e^{im\theta}. \qquad (4.5)$$

Similar expansion can be done to the traction on the horizontal plane

$$\sigma(r,\theta,z,t) = \frac{1}{2\,\pi} \sum_{m=0,\pm 1,\cdots} \int e^{-i\,\omega\,t}\,d\omega \int_0^\infty k^2\,dk \left(T_z \mathbf{R}_m^k + T_r \mathbf{S}_m^k + T_\theta \mathbf{T}_m^k\right). \qquad (4.6)$$

Note that a factor k is drawn from the T_z, T_r and T_θ to simplify the later derived matrices. Eq. (4.1) and (4.6) separate the z-variation of the displacement and stress from the (r, θ) variations. Under this expansion, the second-order differential equation of motion

$$(\lambda + 2\,\mu)\,\nabla\,(\nabla\cdot\mathbf{u}) - \mu\,\nabla\times\nabla\times\mathbf{u} + \rho\,\omega^2\mathbf{u} = 0, \tag{4.7}$$

is reduced to a set of first-order ordinary differential equations

$$\frac{\mathrm{d}}{\mathrm{d}z}\begin{bmatrix} U_r \\ U_z \\ T_z \\ T_r \\ U_\theta \\ T_\theta \end{bmatrix} = k \begin{bmatrix} 0 & -1 & 0 & \frac{1}{\mu} & 0 & 0 \\ 1 - 2\,\xi & 0 & \frac{\xi}{\mu} & 0 & 0 & 0 \\ 0 & -\rho\left(\frac{\omega}{k}\right)^2 & 0 & 1 & 0 & 0 \\ 4\,\mu\,\xi_1 - \rho\left(\frac{\omega}{k}\right)^2 & 0 & 2\,\xi - 1 & 0 & 0 & 0 \\ 0 & 0 & 0 & 0 & 0 & \frac{1}{\mu} \\ 0 & 0 & 0 & 0 & \mu - \rho\left(\frac{\omega}{k}\right)^2 & 0 \end{bmatrix} \begin{bmatrix} U_r \\ U_z \\ T_z \\ T_r \\ U_\theta \\ T_\theta \end{bmatrix}, \tag{4.8}$$

or, in the vector-matrix form:

$$\frac{\mathrm{d}\mathbf{b}(z)}{\mathrm{d}z} = \mathbf{M}\,\mathbf{b}(z). \tag{4.9}$$

Here, ρ is the density; $\xi = \mu/(\lambda + 2\,\mu)$; $\xi_1 = 1 - \xi$; λ, μ are the Lame constants. The vector $\mathbf{b}$ is often called the displacement-stress vector. Note that $\mathbf{M}$ can be partitioned into a 4×4 submatrix describing the motion in the (z, r) plane and a 2×2 submatrix for the motion in the θ-direction. They are often referred to as the P-SV system and the SH system. We will concentrate on the P-SV problem. The corresponding solution for the SH problem can be find in Appendix A.

For a homogeneous medium, $\mathbf{M}$ is constant. In this case, the general solution of (4.9) is

$$\mathbf{b}(z) = \mathrm{e}^{z\,\mathbf{M}}\,\mathbf{b}_0. \tag{4.10}$$

To calculate the matrix exponential, we use the Jordan decomposition of $\mathbf{M}$ [e.g. Turnbull and Aitken, 1952, Gantmatcher, 1960]:

$$\mathbf{M} = \mathbf{E}\,\mathbf{J}\,\mathbf{E}^{-1}, \tag{4.11}$$

where $\mathbf{E}$ is a similarity matrix and $\mathbf{J}$ is the Jordan canonical form of $\mathbf{M}$. Using (4.11) and the definition of matrix exponential, we have

$$\mathrm{e}^{z\,\mathbf{M}} = \mathbf{E}\,\mathrm{e}^{z\,\mathbf{J}}\,\mathbf{E}^{-1}. \tag{4.12}$$

From (4.10) and (4.12), the displacement-stress at any z can be expressed as

$$\mathbf{b}(z) = \mathbf{E}\,\mathbf{\Lambda}(z)\,\mathbf{w}, \tag{4.13}$$

where

$$\mathbf{\Lambda}(z) = \mathrm{e}^{z\,\mathbf{J}}, \tag{4.14}$$

and $\mathbf{w}$ is a constant vector that is to be determined by boundary conditions.

If the matrix $\mathbf{M}$ has a complete set of independent eigenvectors, the Jordan decomposition is reduced to the eigenvalue decomposition. $\mathbf{J}$ is simply a diagonal matrix with the eigenvalues as the diagonal elements and the columns of $\mathbf{E}$ are the eigenvectors. This is the case for the elasto-dynamic problem with $\omega \neq 0$. For the P-SV system, the $4{\times}4$ $\mathbf{M}$ has 4 eigenvalues and

$$\mathbf{J} = \begin{bmatrix} -\nu_\alpha & 0 & 0 & 0 \\ 0 & -\nu_\beta & 0 & 0 \\ 0 & 0 & \nu_\alpha & 0 \\ 0 & 0 & 0 & \nu_\beta \end{bmatrix}, \tag{4.15}$$

where $\nu_\alpha = \sqrt{k^2 - \left(\frac{\omega}{\alpha}\right)^2}$ and $\nu_\beta = \sqrt{k^2 - \left(\frac{\omega}{\beta}\right)^2}$. Here, α, β are the compressional and shear velocities of the medium. Correspondingly,

$$\mathbf{E} = \begin{bmatrix} -1 & -\frac{\nu_\beta}{k} & 1 & \frac{\nu_\beta}{k} \\ \frac{\nu_\alpha}{k} & 1 & \frac{\nu_\alpha}{k} & 1 \\ -2\,\mu\,\gamma_1 & -2\,\mu\,\frac{\nu_\beta}{k} & 2\,\mu\,\gamma_1 & 2\,\mu\,\frac{\nu_\beta}{k} \\ 2\,\mu\,\frac{\nu_\alpha}{k} & 2\,\mu\,\gamma_1 & 2\,\mu\,\frac{\nu_\alpha}{k} & 2\,\mu\,\gamma_1 \end{bmatrix}, \tag{4.16}$$

$$\mathbf{\Lambda}(z) = \begin{bmatrix} \mathrm{e}^{-\nu_\alpha z} & 0 & 0 & 0 \\ 0 & \mathrm{e}^{-\nu_\beta z} & 0 & 0 \\ 0 & 0 & \mathrm{e}^{\nu_\alpha z} & 0 \\ 0 & 0 & 0 & \mathrm{e}^{\nu_\beta z} \end{bmatrix}, \tag{4.17}$$

$$\mathbf{E}^{-1} = \frac{\gamma}{2} \begin{bmatrix} -1 & -\gamma_1\,\frac{k}{\nu_\alpha} & \frac{1}{2\,\mu} & \frac{k}{2\,\mu\,\nu_\alpha} \\ \gamma_1\,\frac{k}{\nu_\beta} & 1 & -\frac{k}{2\,\mu\,\nu_\beta} & -\frac{1}{2\,\mu} \\ 1 & -\gamma_1\,\frac{k}{\nu_\alpha} & -\frac{1}{2\,\mu} & \frac{k}{2\,\mu\,\nu_\alpha} \\ -\gamma_1\,\frac{k}{\nu_\beta} & 1 & \frac{k}{2\,\mu\,\nu_\beta} & -\frac{1}{2\,\mu} \end{bmatrix}, \tag{4.18}$$

where $\gamma = 2\,k^2\,\beta^2/\omega^2$, $\gamma_1 = 1 - 1/\gamma$.

For the dynamic SH problem,

$$\mathbf{J} = \begin{bmatrix} \nu_\beta & 0 \\ 0 & -\nu_\beta \end{bmatrix}, \tag{4.19}$$

$$\mathbf{E} = \begin{bmatrix} -1 & 1 \\ \mu\frac{\nu_\beta}{k} & \mu\frac{\nu_\beta}{k} \end{bmatrix}, \tag{4.20}$$

$$\mathbf{\Lambda}(z) = \begin{bmatrix} \mathrm{e}^{-\nu_\beta z} & 0 \\ 0 & \mathrm{e}^{\nu_\beta z} \end{bmatrix}, \tag{4.21}$$

$$\mathbf{E}^{-1} = \frac{1}{2} \begin{bmatrix} -1 & \frac{k}{\mu\,\nu_\beta} \\ 1 & \frac{k}{\mu\,\nu_\beta} \end{bmatrix}. \tag{4.22}$$
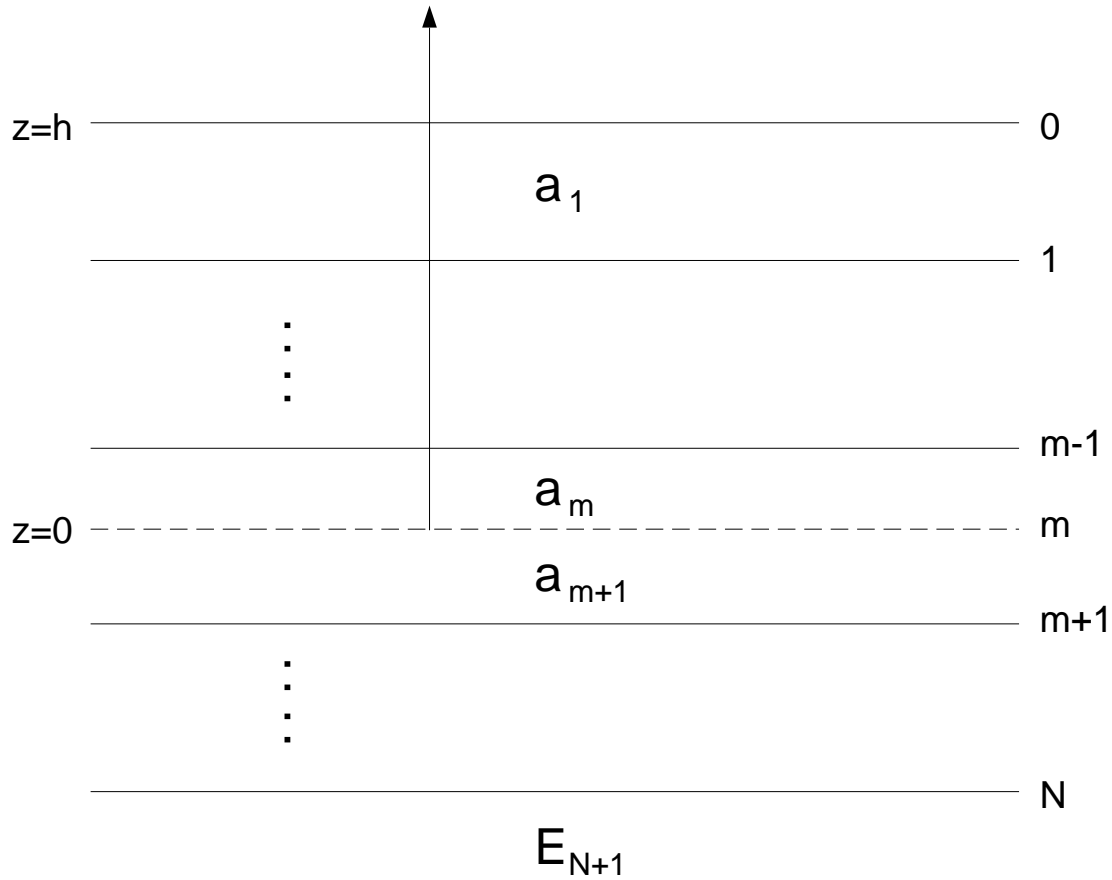
Figure 4.1: A layered half-space consists of N layers over a half-space at the bottom. The source is located at a depth of h between layer m and $m+1$ with identical elastic properties.

4.2 Surface displacement of layered half-space from an embedded point source

The general description of model is shown in Figure 4.1. It consists of a stack of layers on top of half space, with source embedded somewhere in the middle. The solution to the wave equation within each layer is represented by the wave-vector $\mathbf{w}_n$. The boundary conditions are:

1. Continuity of displacement and stress across all interfaces except at the source interface.

2. Vanishing of up-going waves in the half space.

3. Vanishing of stress at the free surface.

From (4.13) the stress-displacement vectors at top and bottom of layer n are:

$$\mathbf{b}_{n-1} = \mathbf{E}_n \mathbf{\Lambda}_n(z_{n-1})\mathbf{w}_n, \tag{4.23}$$

$$\mathbf{b}_n = \mathbf{E}_n \mathbf{\Lambda}_n(z_n)\mathbf{w}_n, \tag{4.24}$$

which lets us to "propagate" the stress-displacement vector from the top to the bottom:

$$\mathbf{b}_n = \mathbf{a}_n \mathbf{b}_{n-1}, \tag{4.25}$$

where

$$\mathbf{a}_n = \mathbf{E}_n \mathbf{\Lambda}_n(z_n - z_{n-1})\mathbf{E}_n^{-1} = \mathbf{E}_n \mathbf{\Lambda}_n(d_n)\mathbf{E}_n^{-1}. \tag{4.26}$$

The $\mathbf{a}$ matrix is often called Thompson-Haskell propagation matrix [Haskell, 1964, Wang and Herrmann, 1980]:

For the *P-SV* system

$$\mathbf{a}_n = \gamma \begin{bmatrix} C_\alpha - \gamma_1 C_\beta & \gamma_1 Y_\alpha - X_\beta & \frac{C_\beta - C_\alpha}{2\mu} & \frac{X_\beta - Y_\alpha}{2\mu} \\ \gamma_1 Y_\beta - X_\alpha & C_\beta - \gamma_1 C_\alpha & \frac{X_\alpha - Y_\beta}{2\mu} & \frac{C_\alpha - C_\beta}{2\mu} \\ 2\mu\gamma_1 (C_\alpha - C_\beta) & 2\mu (\gamma_1^2 Y_\alpha - X_\beta) & C_\beta - \gamma_1 C_\alpha & X_\beta - \gamma_1 Y_\alpha \\ 2\mu (\gamma_1^2 Y_\beta - X_\alpha) & 2\mu\gamma_1 (C_\beta - C_\alpha) & X_\alpha - \gamma_1 Y_\beta & C_\alpha - \gamma_1 C_\beta \end{bmatrix}, \tag{4.27}$$

where $C_\alpha = \cosh(\nu_\alpha d)$, $X_\alpha = \nu_\alpha \sinh(\nu_\alpha d)/k$, and $Y_\alpha = k \sinh(\nu_\alpha d)/\nu_\alpha$, and similarly for C_β, X_β, and Y_β. $d = z_{n-1} - z_n$ is the thickness of the layer. Our $\mathbf{a}_n$ is different from the original one given by Haskell [1964] for the traction related terms. This stems from the difference of our definition of the displacement-stress vector from the Haskell's in which he multiplied the traction by ω^2. As shown later, the Haskell's definition introduces the apparent ω-dependence of source terms and causes difficulty to unify the elasto-dynamic solution and the elasto-static solution.

For the *SH* problem, the Thomson-Haskell propagator matrix is

$$\mathbf{a} = \begin{bmatrix} C_\beta & -\frac{Y_\beta}{\mu} \\ -\mu X_\beta & C_\beta \end{bmatrix}. \tag{4.28}$$

At the interface where the source is located, $\mathbf{b}$ is discontinuous due to the presence of the source:

$$\mathbf{b}_m^- = \mathbf{b}_m^+ - \mathbf{s}. \tag{4.29}$$

Since $\mathbf{b}$ is continuous at all other interfaces, we can connect the wave-vector in half space with the stress-displacement vector at the surface

$$\mathbf{\Lambda}_{N+1}(z_N)\mathbf{w}_{N+1} = \mathbf{X}\mathbf{b}_m^- = \mathbf{X}(\mathbf{b}_m^+ - \mathbf{s}) = \mathbf{R}\mathbf{b}_0 - \mathbf{X}\mathbf{s}, \tag{4.30}$$

where

$$\mathbf{X} = \mathbf{E}_{N+1}^{-1}\mathbf{a}_N \cdots \mathbf{a}_{m+1}, \tag{4.31}$$

$$\mathbf{R} = \mathbf{E}_{N+1}^{-1}\mathbf{a}_N \cdots \mathbf{a}_1. \tag{4.32}$$

The stress-free surface boundary condition means that for $\mathbf{b}_0$:

$$T_z = T_r = T_\theta = 0. \tag{4.33}$$

In the bottom half-space, the components of $\mathbf{w}_{N+1}$ associated with up-going waves $e^{-\nu_{\alpha,\beta}z}$ should vanish:

$$w_{N+1}(1) = w_{N+1}(2) = w_{N+1}(5) = 0. \tag{4.34}$$

We then get:

$$\begin{pmatrix} R_{11} & R_{12} & 0 \\ R_{21} & R_{22} & 0 \\ 0 & 0 & R_{55} \end{pmatrix} \begin{pmatrix} U_r \\ U_z \\ U_\theta \end{pmatrix} - \begin{pmatrix} X_{11} & X_{12} & X_{13} & X_{14} & 0 & 0 \\ X_{21} & X_{22} & X_{23} & X_{24} & 0 & 0 \\ 0 & 0 & 0 & 0 & X_{55} & X_{56} \end{pmatrix} \mathbf{s} = \begin{pmatrix} 0 \\ 0 \\ 0 \end{pmatrix}. \tag{4.35}$$

Solving above linear equations, we can obtain the displacement at the surface:

$$\begin{pmatrix} U_r \\ U_z \end{pmatrix} = \frac{1}{F_R} \begin{pmatrix} R_{22} & -R_{12} \\ -R_{21} & R_{11} \end{pmatrix} \begin{pmatrix} X_{1i}s_i \\ X_{2i}s_i \end{pmatrix}, \tag{4.36}$$

$$U_\theta = \frac{X_{5i}s_i}{F_L}, \tag{4.37}$$

where

$$F_R = R_{11}R_{22} - R_{21}R_{12}, \tag{4.38}$$

$$F_L = R_{55}, \tag{4.39}$$

are often called Rayleigh denominator and Love denominator.

As an example, consider a half space,

$$\mathbf{R} = \mathbf{E}^{-1}, \tag{4.40}$$

The Rayleigh denominator

$$F_R = R_{11}R_{22} - R_{21}R_{12} = \frac{1}{k^2} \left((1-\gamma)^2 k^2 - \gamma^2 \nu_\alpha \nu_\beta \right), \tag{4.41}$$

Figure 4.2 plots F_R as a function of k.

For a layer over half space,

$$\mathbf{R} = \mathbf{E}_2^{-1}\mathbf{a}_1, \tag{4.42}$$

The Love denominator:

$$F_L = R_{55} = -\frac{1}{2} \left(\cosh \nu_{\beta_1} d - \frac{\rho_1 \nu_{\beta_1} \beta_1^2}{\rho_2 \nu_{\beta_2} \beta_2^2} \sinh \nu_{\beta_1} d \right), \tag{4.43}$$

which is shown in Figure 4.3.
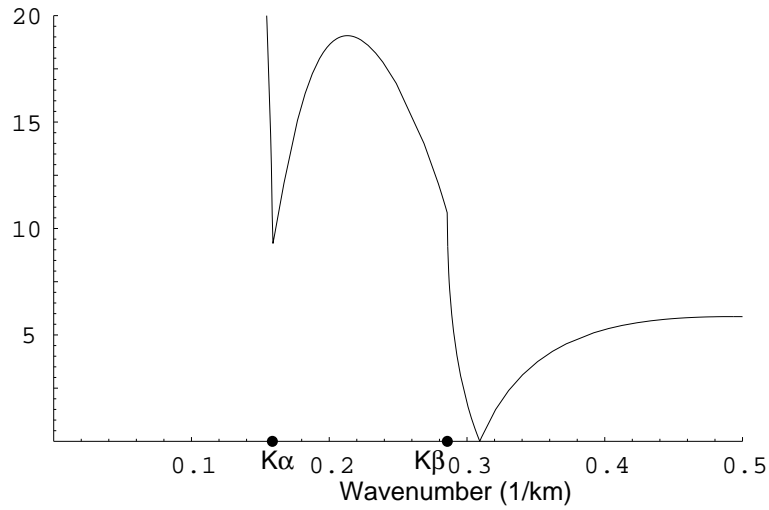
Figure 4.2: Raleigh denominator ($\omega = 1$ Hz) and locations of branch points and Rayleigh pole for a half space (α=6.3 km/s, β=3.5 km/s). Note that the Rayleigh pole is on the right of k_β which means that Rayleigh velocity is slower than the shear velocity of the half space.
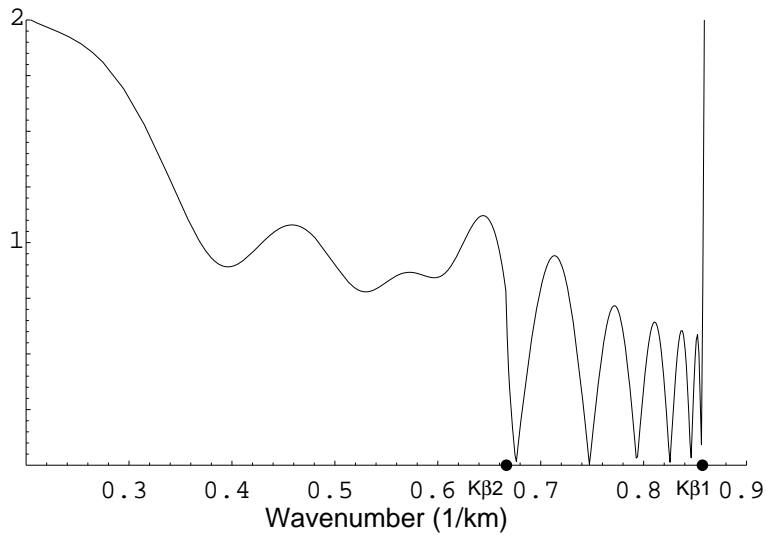
Figure 4.3: Love denominator as function of wavenumber (we set $\omega = 3$ Hz) for a one layer over half space model. Note that there are multiple poles corresponding to fundamental and higher modes and all the poles are located between k_{β_1} and k_{β_2}.

37

4.3 Source terms and horizontal radiation pattern

The displacement-stress discontinuities to represent the source can be found by expanding the solution of the whole-space problem with the cylindrical spherical harmonics (4.1 and 4.6) [Haskell, 1953, Takeuchi and Saito, 1972]. Takeuchi and Saito [1972] have listed the displacement-stress discontinuities produced by various sources. Since our definition of $\mathbf{s}$ is slightly different from theirs, we will give below the non-zero terms for several types of sources often encountered in seismology.

4.3.1 Explosion source

Only $m = 0$ term exists for the isotropic source

$$\mathbf{s}^0 = (0,\ \xi/\mu,\ 0,\ 2\xi,\ 0,\ 0)^{\mathrm{T}}. \tag{4.44}$$

4.3.2 Single force

None-zero terms exist for $m = 0, \pm1$. We use the symmetry between $m = -1$ and $m = 1$ terms and factor out the common source geometry independent term. This reduces the number of source vectors $\mathbf{s}$ from 3 to 2:

$$\mathbf{s}^0 = \frac{1}{k} (0,\ 0,\ -1,\ 0,\ 0,\ 0)^{\mathrm{T}}, \tag{4.45}$$

$$\mathbf{s}^1 = \frac{1}{k} (0,\ 0,\ 0,\ -1,\ 0,\ 1)^{\mathrm{T}}. \tag{4.46}$$

They will produce five components of ground displacement, u_z^0, u_r^0, u_z^1, u_r^1, u_θ^1 (u_θ^0 is always zero). The actual displacement is obtained by adding the force orientation when summing over azimuthal modes m. By re-arranging terms, the summation can be expressed as

$$u_z = \cos\phi \cos\delta\, u_z^1 - \sin\delta\, u_z^0, \tag{4.47}$$

$$u_r = \cos\phi \cos\delta\, u_r^1 - \sin\delta\, u_r^0, \tag{4.48}$$

$$u_\theta = -\sin\phi \cos\delta\, u_\theta^1, \tag{4.49}$$

where δ is the dip angle of the force, measured from the horizontal plane; ϕ is the azimuth of the station, measured clockwise from the direction of the force. It can be seen that $\mathbf{u}^0$ is produced by an unit vertical force (upward) and $\mathbf{u}^1$ is produced by a horizontal force of magnitude $\sqrt{2}$ at azimuth 45° CCW from the force direction.

4.3.3 Double-couple without torque

Similar to the single force, the five none-zero source vectors ($m = 0$, ± 1, ± 2) can be reduced to three:

$$
\begin{aligned}
\mathbf{s}^0 &= (0,\, 2\,\xi/\mu,\, 0,\, 4\,\xi - 3,\, 0,\, 0)^{\mathrm{T}}, && (4.50) \\
\mathbf{s}^1 &= (1/\mu,\, 0,\, 0,\, 0,\, -1/\mu,\, 0)^{\mathrm{T}}, && (4.51) \\
\mathbf{s}^2 &= (0,\, 0,\, 0,\, 1,\, 0,\, -1)^{\mathrm{T}}. && (4.52)
\end{aligned}
$$

The displacement for arbitrary double-couple is

$$
\begin{aligned}
u_z =\ & \frac{1}{2}\sin 2\delta \,\sin\lambda\, u_z^0 \\
& - (\sin\phi\,\cos 2\delta\,\sin\lambda - \cos\phi\,\cos\delta\,\cos\lambda)\, u_z^1 \\
& - (\sin 2\phi\,\sin\delta\,\cos\lambda + \frac{1}{2}\cos 2\phi\,\sin 2\delta\,\sin\lambda)\, u_z^2,
\end{aligned}
\qquad (4.53)
$$

$$
\begin{aligned}
u_r =\ & \frac{1}{2}\sin 2\delta \,\sin\lambda\, u_r^0 \\
& - (\sin\phi\,\cos 2\delta\,\sin\lambda - \cos\phi\,\cos\delta\,\cos\lambda)\, u_r^1 \\
& - (\sin 2\phi\,\sin\delta\,\cos\lambda + \frac{1}{2}\cos 2\phi\,\sin 2\delta\,\sin\lambda)\, u_r^2,
\end{aligned}
\qquad (4.54)
$$

$$
\begin{aligned}
u_\theta =\ & -(\sin\phi\,\cos\delta\,\cos\lambda + \cos\phi\,\cos 2\delta\,\sin\lambda)\, u_\theta^1 \\
& + (\frac{1}{2}\sin 2\phi\,\sin 2\delta\,\sin\lambda - \cos 2\phi\,\sin\delta\,\cos\lambda)\, u_\theta^2,
\end{aligned}
\qquad (4.55)
$$

where δ is the dip angle of the fault plane; λ is the slip direction measured counterclockwise from the strike of the fault; ϕ is the azimuth of the station, measured clockwise from the strike of the fault. The above coefficients are often called the horizontal radiation patterns and were given by different authors [e.g. Aki and Richards, 1980, Wang and Herrmann, 1980, Helmberger, 1983]. The results show that $\mathbf{u}^0$ is produced by a 45° down-dip slip (magnitude -2) at azimuth 45° from the fault strike, $\mathbf{u}^1$ is produced by a vertical dip slip (magnitude -$\sqrt{2}$) at azimuth 45°, and $\mathbf{u}^2$ is produced by a vertical strike slip (magnitude -$\sqrt{2}$) at azimuth 22.5°.

4.4 Frequency-wavenumber integration

Calculation of Green's function involves following double integration:

$$
\int_0^\infty e^{i\omega t}\mathrm{d}\omega \int_0^\infty U(\omega, k) J_n(kr)\,\mathrm{d}k,
\qquad (4.56)
$$

which can be done in different ways (GRT, slowness method, etc). The frequency-wavenumber (F-K) integration method that we are going to discuss below does the k-integration first by some numerical integration scheme. The ω-integration is then easily implemented by the inverse fast Fourier transform (IFFT).
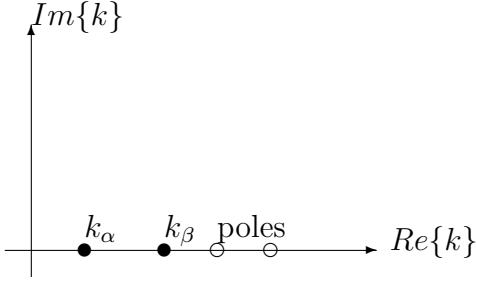
Figure 4.4: Location of branch points and poles in complex k-plane.

4.4.1 Wavenumber integration

The k-integration over the real k-axis from 0 to ∞ is complicated by several issues. First, the branch points k_α, k_β, and also the Rayleigh poles and Love poles, are all located on the real axis (Figure 4.4). This makes the numerical computation of $U(\omega, k)$ very unstable. Fortunately for anelastic medium, the velocities are complex and frequency-dependent:

$$ v = v_r(1 + \frac{1}{\pi Q} \log f + \frac{i}{2Q}), \tag{4.57} $$

where v_r is the reference velocity at 1 Hz. Since

$$ k_\alpha = \frac{\omega}{\alpha}, \qquad\qquad k_\beta = \frac{\omega}{\beta}, \tag{4.58} $$

all the branch points and poles are moved below the real k axis. As shown in Figure 4.5, introducing attenuation in the velocity model helps to smooth the kernel and stabilize the calculation.

Another way to stabilize the computation of $U(\omega, k)$ along real k-axis is to introduce a small negative imaginary part in ω, while will also move branch points below the real k axis. Instead of calculating $U(\omega, k)$, we now calculate $U(\omega - \sigma i, k)$. Because

$$ IFFT\left[f(\omega - \sigma i)\right] = e^{-\sigma t}f(t) + \sum_{n \neq 0} f(t + nT)e^{-\sigma(t+nT)}, \tag{4.59} $$

where $T = \frac{2\pi}{d\omega}$, this small imaginary part helps to damp the time sequence and reduce wrap-around (time aliasing).

Integration using trapezoidal rule

A simple integration scheme is to use trapezoidal rule:

$$ \int_{k_1}^{k_1+dk} g(k)\,\mathrm{d}k = \frac{dk}{2}(g(k_1) + g(k_1 + dk)), \tag{4.60} $$

40
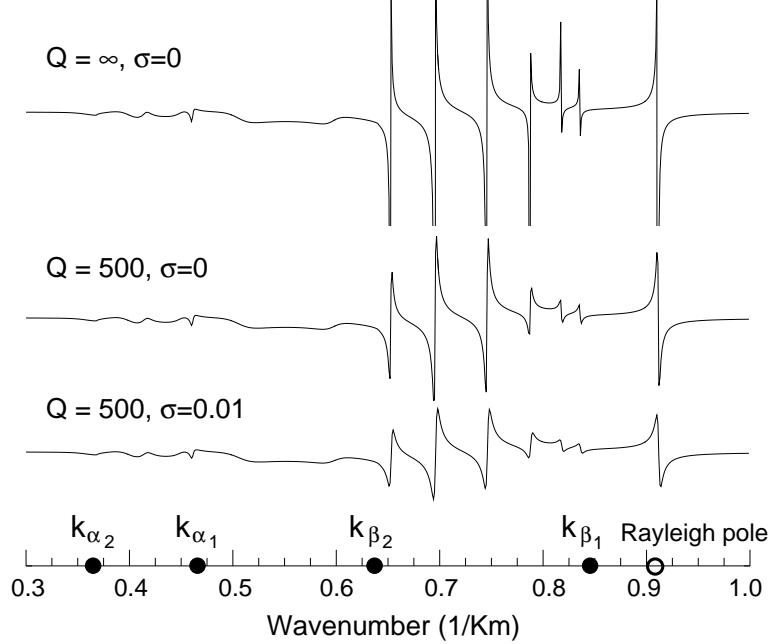
Figure 4.5: Vertical displacement kernel as function of k for different Q_β and σ value (we set $\omega = 0.47\ Hz$). The velocity model is a one-layer over half-space, with $\alpha_1 = 6.3$, $\beta_1 = 3.5$, $\alpha_2 = 8.1$, $\beta_2 = 4.5$.

where $g(k) = U(k)J_n(kr)$. So the integration from $k = 0$ to k_{max} can be approximated by (assuming $g(0) = g(k_{max}) = 0$, which is usually the case):

$$\int_0^{k_{max}} g(k)\, \mathrm{d}k = dk(g_1 + g_2 + \cdots + g_n). \tag{4.61}$$

Usually the integrand $g(k)$ is highly oscillatory, especially at large r (Figure 4.6). Generally the trapezoidal rule is not a good scheme for this kind of integration. However, from a physical point of view, replacing continuous k-integral with summation of discrete horizontal wavenumbers is equivalent to summing all contributions from infinite number of point sources uniformly distributed in horizontal plane [Bouchon, 1981], with separation distance:

$$L = \frac{2\pi}{dk}, \tag{4.62}$$

(Figure 4.7). So, as long as this separation satisfies:

$$L > 2r, \tag{4.63}$$
$$\sqrt{(L-r)^2 + h^2} > v_{max}t, \tag{4.64}$$

the wavefield obtained at (r, t) will not be disturbed by the closest neighbor source.
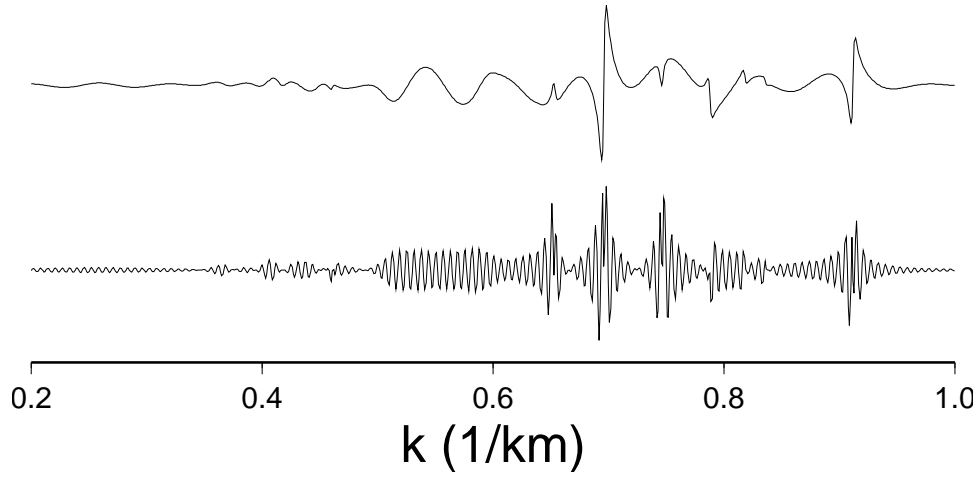
Figure 4.6: F-K integrand $U(\omega, k)J_0(kx)$ at distance ranges of 100 km (above) and 1000 km (below).
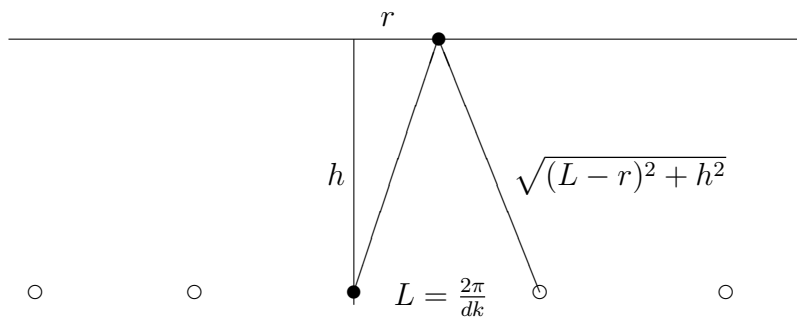
Figure 4.7: Discrete summation in wavenumber is equivalent to summing infinite number of point sources (open circles) uniformly distributed in r direction.
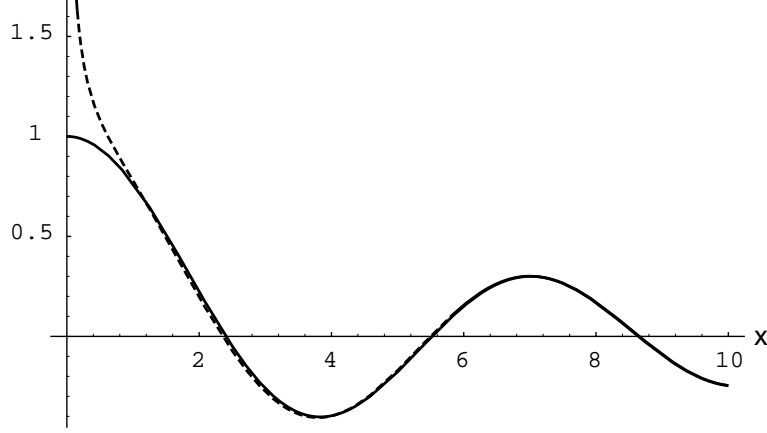
Figure 4.8: Bessel function $J_0(x)$ (solid line) and its first term of asymptotic expansion $\sqrt{\frac{2}{\pi x}} \cos(x - \frac{\pi}{4})$ (dashed line).

Filon scheme

Another method often used for integrating oscillatory functions is the Filon scheme [e.g. Saikia, 1994]. It tries to separate the kernel $U(k)$ from the more oscillatory Bessel function $J_n(kr)$ through integration by parts.

First we express Bessel function in terms of Hankel functions:

$$J_n(kr) = \frac{H_n^{(1)}(kr) + H_n^{(2)}(kr)}{2}. \tag{4.65}$$

As $kr \gg 1$, we have:

$$H_n^{(1)} \sim \sqrt{\frac{2}{\pi kr}} e^{ikr}, \tag{4.66}$$

$$H_n^{(2)} \sim \sqrt{\frac{2}{\pi kr}} e^{-ikr}. \tag{4.67}$$

Dropping the $H_n^{(1)}$ term which represents inward propagating waves, and integrating by parts:

$$\int_{k_1}^{k_1+dk} U(k) e^{-ikr} \, \mathrm{d}k = -\frac{1}{ir} (U e^{-ikr})|_{k_1}^{k_1+dk} + \frac{1}{ir} \int_{k_1}^{k_1+dk} U' e^{-ikr} \, \mathrm{d}k. \tag{4.68}$$

Assuming $U(k)$ is linear between k_1 and $k_1 + dk$, RHS can be written as:

$$
\begin{aligned}
&-\frac{1}{ir} (g(k_1 + dk) - g(k_1)) + \frac{U(k_1 + dk) - U(k_1)}{irdk} \int_{k_1}^{k_1+dk} e^{-ikr} \, \mathrm{d}k \\
&= -\frac{1}{ir} (g(k_1 + dk) - g(k_1)) + \frac{U(k_1 + dk) - U(k_1)}{r^2 dk} (e^{-ir(k_1+dk)} - e^{-irk_1}),
\end{aligned} \tag{4.69}
$$

43

finally, we have:

$$\int_{k_1}^{k_1+dk} U(k)e^{-ikr}\,\mathrm{d}k = dk(c\,g(k_1) + \tilde{c}\,g(k_1+dk)), \tag{4.70}$$

where

$$c = \frac{1-\cos\epsilon + i(\sin\epsilon - \epsilon)}{\epsilon^2}, \tag{4.71}$$

$$\epsilon = rdk. \tag{4.72}$$

So, the integration can be approximated by:

$$\int_0^{k_{max}} g(k)\,\mathrm{d}k = 2\frac{1-\cos\epsilon}{\epsilon^2}dk(g_1 + g_2 + \cdots + g_n). \tag{4.73}$$

Note that above formula differs from (4.61) only by a coefficient. So the two schemes should give same waveform shapes with different amplitudes. Numerical test shows that the Filon scheme gives poor amplitude prediction. The reason is that the assumption it made about kernel's linear behavior between any two sampling points is not proper in our case.

4.4.2   Compound matrix

Haskell propagator matrix elements contain exponential function like $e^{\pm\nu d}$. Multiplication of propagator matrices of several layers usually causes severe loss of significant digits and leads to large numerical errors. A solution is to use the so-called *compound matrix* instead of the Haskell matrix itself. The compound matrix of $\mathbf{A}$ is formed by its subdeterminants:

$$\mathbf{A}|_{kl}^{ij} = A_{ik}A_{jl} - A_{il}A_{jk}. \tag{4.74}$$

By factoring $\mathbf{R}$ into two parts

$$\mathbf{R} = \mathbf{XZ}, \tag{4.75}$$

where

$$\mathbf{Z} = \mathbf{a}_m \dots \mathbf{a}_1, \tag{4.76}$$

is the propagator matrix from the surface to above the source, the displacement kernels in Eq. (4.36) can be expressed as:

$$\begin{pmatrix} U_r \\ U_z \end{pmatrix} = \frac{1}{\mathbf{R}|_{12}^{12}} \begin{pmatrix} s_i\mathbf{X}|_{ij}^{12}Z_{j2} \\ -s_i\mathbf{X}|_{ij}^{12}Z_{j1} \end{pmatrix}, \tag{4.77}$$

where

$$\mathbf{X}|_{ij}^{12} = (\mathbf{E}_{N+1}^{-1})|_{mn}^{12}\mathbf{a}_N|_{op}^{mn} \dots \mathbf{a}_{m+1}|_{ij}^{st}, \tag{4.78}$$

$$\mathbf{R}|_{12}^{12} = (\mathbf{E}_{N+1}^{-1})|_{mn}^{12}\mathbf{a}_N|_{op}^{mn} \dots \mathbf{a}_1|_{12}^{st}. \tag{4.79}$$

Note that the 4×4 matrix $\mathbf{X}|_{ij}^{12}$ can also be viewed as a 1×6 row vector

$$\mathbf{g} = (\mathbf{X}|_{12}^{12}, \mathbf{X}|_{13}^{12}, \mathbf{X}|_{14}^{12}, \mathbf{X}|_{23}^{12}, \mathbf{X}|_{24}^{12}, \mathbf{X}|_{34}^{12}), \tag{4.80}$$

which is to be propagated upward by the 6×6 compound matrix, see Wang and Herrmann [1980] for details.

4.4.3 Other boundary conditions

If the top interface is not a free surface but the bottom of an elastic half-space, the stress-free boundary condition is replaced by the vanishing of down-going waves in the top half-space. The equation takes the same form of Eq. (4.30) except the matrix $\mathbf{R}$ is multiplied from the right by matrix $\mathbf{E_0}$ of the top half-space.

If the bottom interface is a free boundary, the LHS of Eq. (4.30) is replaced by the displacement-stress vector at the bottom with rows 3 and 4 vanished. By multiplying both sides by

$$\mathbf{H} = \begin{pmatrix} 0 & 0 & 1 & 0 \\ 0 & 0 & 0 & 1 \\ 1 & 0 & 0 & 0 \\ 0 & 1 & 0 & 0 \end{pmatrix}, \tag{4.81}$$

we swap rows 1–2 with 3–4 thus obtain the same format solution of Eq. (4.36), except that $\mathbf{E}_N^{-1}$ is replaced by $\mathbf{H}$ in $\mathbf{L}$ and $\mathbf{R}$. Similar technique can be used to handle rigid bottom boundary condition by using an unit matrix for $\mathbf{H}$, see Herrmann [2007].

4.4.4 Buried receivers

For obtaining displacement kernels for buried receivers beneath the surface but above the source level, one might attempt to obtain the surface displacement vector first and then use the Haskell matrix to propagate it down to the receiver depth:

$$\begin{pmatrix} U_r \\ U_z \\ T_z \\ T_r \end{pmatrix} = \frac{\mathbf{Y}}{\mathbf{R}|_{12}^{12}} \begin{pmatrix} s_i \mathbf{X}|_{ij}^{12} Z_{j2} \\ -s_i \mathbf{X}|_{ij}^{12} Z_{j1} \\ 0 \\ 0 \end{pmatrix}, \tag{4.82}$$

where $\mathbf{Y}$ is the propagator matrix from the surface to the receiver. This approach is, however, not numerically stable at high frequencies due to the exponential functions in the Haskell matrix. Herrmann [2007] used the compound matrix by replacing the $\mathbf{Z}$ matrix above with

$$\mathbf{Z} = \mathbf{VY}, \tag{4.83}$$

where $\mathbf{V}$ is the propagator matrix from the receiver to the source. The displacement-stress vector at the buried receiver becomes

$$\begin{pmatrix} U_r \\ U_z \\ T_z \\ T_r \end{pmatrix} = \frac{1}{\mathbf{R}|_{12}^{12}} \begin{pmatrix} s_i \mathbf{X}|_{ij}^{12} V_{jk} \mathbf{Y}|_{12}^{1k} \\ s_i \mathbf{X}|_{ij}^{12} V_{jk} \mathbf{Y}|_{12}^{2k} \\ s_i \mathbf{X}|_{ij}^{12} V_{jk} \mathbf{Y}|_{12}^{3k} \\ s_i \mathbf{X}|_{ij}^{12} V_{jk} \mathbf{Y}|_{12}^{4k} \end{pmatrix}. \tag{4.84}$$

If the receiver is below the source, one can flip the model to carry out the same computations and correct the vertical displacement polarity when done. In the process, source vectors $\mathbf{s}^0$ of single force and $\mathbf{s}^1$ of double couple need to be reversed.

4.4.5 Partitioning of up-going and down-going wavefields

Partitioning of total wavefield into up-going and down-going wavefields is done by separating the source displacement-stress jump vector $\mathbf{s}$ into the up-going and down-going parts:

$$\mathbf{s} = \mathbf{s}^+ + \mathbf{s}^- = (\mathbf{D}^+ + \mathbf{D}^-)\mathbf{s}. \tag{4.85}$$

For the P-SV system,

$$\mathbf{D}^+ = \mathbf{E} \begin{pmatrix} 1 & 0 & 0 & 0 \\ 0 & 1 & 0 & 0 \\ 0 & 0 & 0 & 0 \\ 0 & 0 & 0 & 0 \end{pmatrix} \mathbf{E}^{-1}$$

$$= \frac{1}{2} \begin{pmatrix} 1 & \gamma\left(\gamma_1\dfrac{k}{\nu_\alpha} - \dfrac{\nu_\beta}{k}\right) & 0 & \dfrac{\gamma}{2\mu}\left(\dfrac{\nu_\beta}{k} - \dfrac{k}{\nu_\alpha}\right) \\ \gamma\left(\gamma_1\dfrac{k}{\nu_\beta} - \dfrac{\nu_\alpha}{k}\right) & 1 & \dfrac{\gamma}{2\mu}\left(\dfrac{\nu_\alpha}{k} - \dfrac{k}{\nu_\beta}\right) & 0 \\ 0 & 2\mu\gamma\left(\gamma_1^2\dfrac{k}{\nu_\alpha} - \dfrac{\nu_\beta}{k}\right) & 1 & \gamma\left(\dfrac{\nu_\beta}{k} - \gamma_1\dfrac{k}{\nu_\alpha}\right) \\ 2\mu\gamma\left(\gamma_1^2\dfrac{k}{\nu_\beta} - \dfrac{\nu_\alpha}{k}\right) & 0 & \gamma\left(\dfrac{\nu_\alpha}{k} - \gamma_1\dfrac{k}{\nu_\beta}\right) & 1 \end{pmatrix}, \tag{4.86}$$

and for the SH system,

$$\mathbf{D}^+ = \frac{1}{2} \begin{pmatrix} 1 & \dfrac{k}{\mu\nu_\beta} \\ \dfrac{\mu\nu_\beta}{k} & 1 \end{pmatrix}. \tag{4.87}$$

4.4.6 Some practical aspects in the F-K integration

I have written a Fortran code to implement the propagator matrix algorithm to compute the displacement kernels. This code closely follows the notations of Zhu and Rivera [2002]. The structure of the Fortran program to calculate F-K integration can be illustrated as following:

```
for frequency = ω_min to ω_max step dω
    for wavenumber = k_min to k_max step dk
        for layer = bottom to top
            calculating propagation matrix
        end of layer loop
        calculating kernel U(k,ω)
        summing J(kx)U(k,ω)
    end of wavenumber loop
end of frequency loop
```

inverse Fourier transformation

There are essentially three loops in the computation, i.e., layer-propagation, k-loop, and ω-loop. For each k and ω, the code starts at the bottom half space, initializing the $\mathbf{g}$ with the $(\mathbf{E}_{N+1}^{-1})|_{ij}^{12}$. Then it propagates this $1{\times}6$ vector upward using the compound matrix of each layer. When crossing the source interface, it initializes the $1{\times}4$ vector $z_j = s_i \mathbf{X}|_{ij}^{12}$ and then propagates it upward using the Haskell matrix $\mathbf{a}$ until reaching the surface. The total time will be proportional to the number of layers in the model, k-samplings rate, and ω-samplings rate. Because displacement kernels are independent of distance range x, calculating for multiple distance ranges only slightly increases computation time.

The efficiency and success of calculating full time response using F-K double integration depends on correct chose of several parameters. For k-integration, we need to decide the k sampling interval, dk, and maximum wavenumber, k_{max}. Both are model dependent. k_{max} is determined by the lowest velocity in the model.

$$k_{max} > \frac{\omega}{v_{min}}, \tag{4.88}$$

and dk has to satisfy the Bouchon criteria:

$$dk < \frac{\pi}{x_{max}}. \tag{4.89}$$

For ω-integration, ω_{max} and $d\omega$ are determined by the sampling rate, dt, and duration of the signal, T, we desire to calculate:

$$\omega_{max} = \frac{\pi}{dt}, \tag{4.90}$$

$$d\omega = \frac{2\pi}{T}. \tag{4.91}$$

If the actual duration of signal is longer than T, time-aliasing (wrap-around) will occur. This, as we shown before, can be mitigated by introducing a small imaginary part σ in the frequency. It also help to smooth the displacement kernels to avoid space-aliasing. But too large σ can introduce long-period noise in the result. Usually we select σ in such a way that the end of signal is damped by factor of 2-3 with respect to the beginning of the signal. This means that.

$$\sigma = \frac{2 \sim 3}{T}. \tag{4.92}$$

Some examples are given in Figures 4.9 to 4.12. A sample of input for the *fk* code is given below
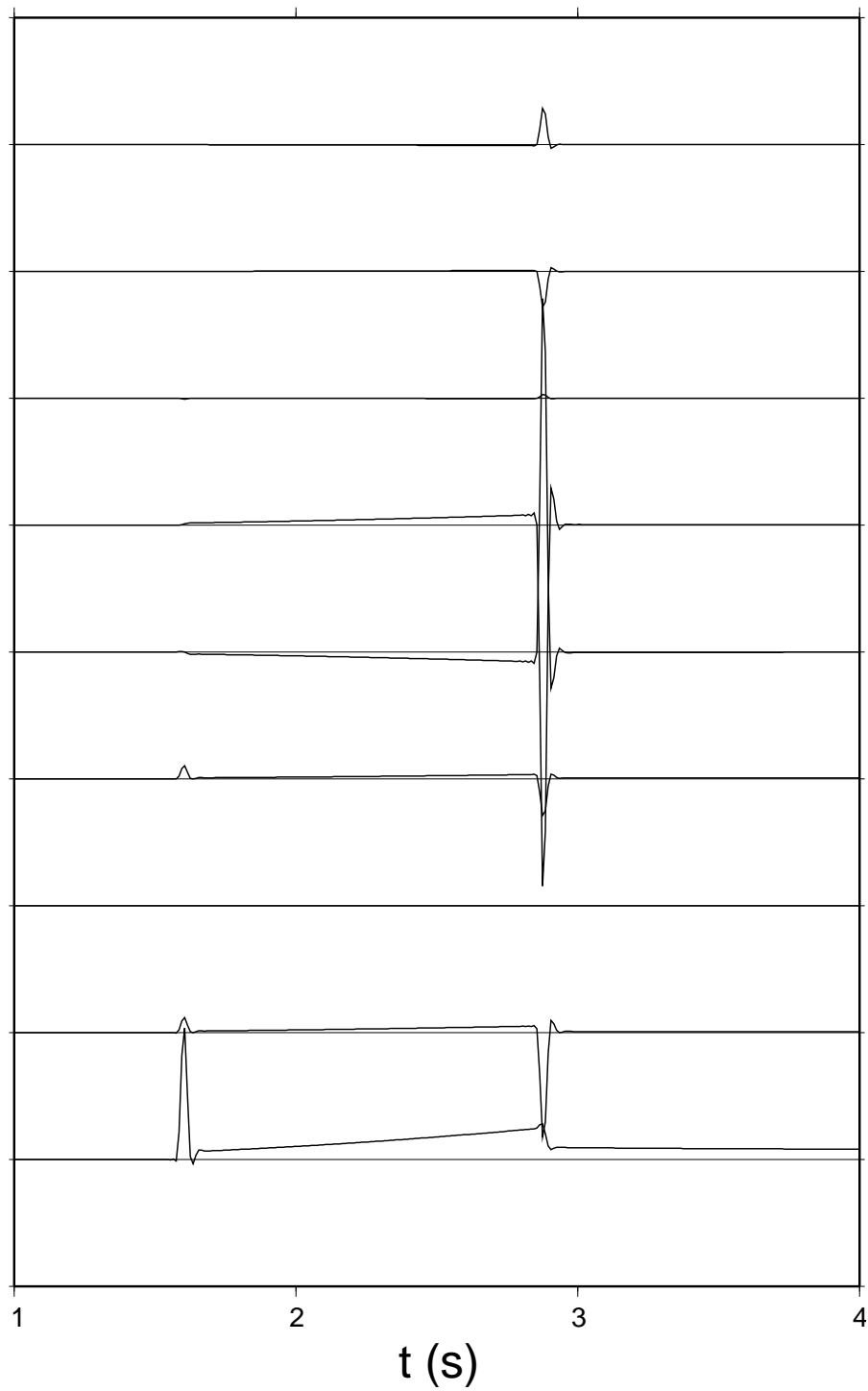
Figure 4.9: Components of Greens' function at distance of 1 km for a double couple source in half space (V_p=6.3 km/s, V_s=3.5 km/s, source depth 10 km). The components are, from the bottom to top, ZDD, RDD, TDD, ZDS, RDS, TDS, ZSS, RSS, and TSS. The near field between P and S arrivals and permanent displacements after S are best displayed on ZDD.
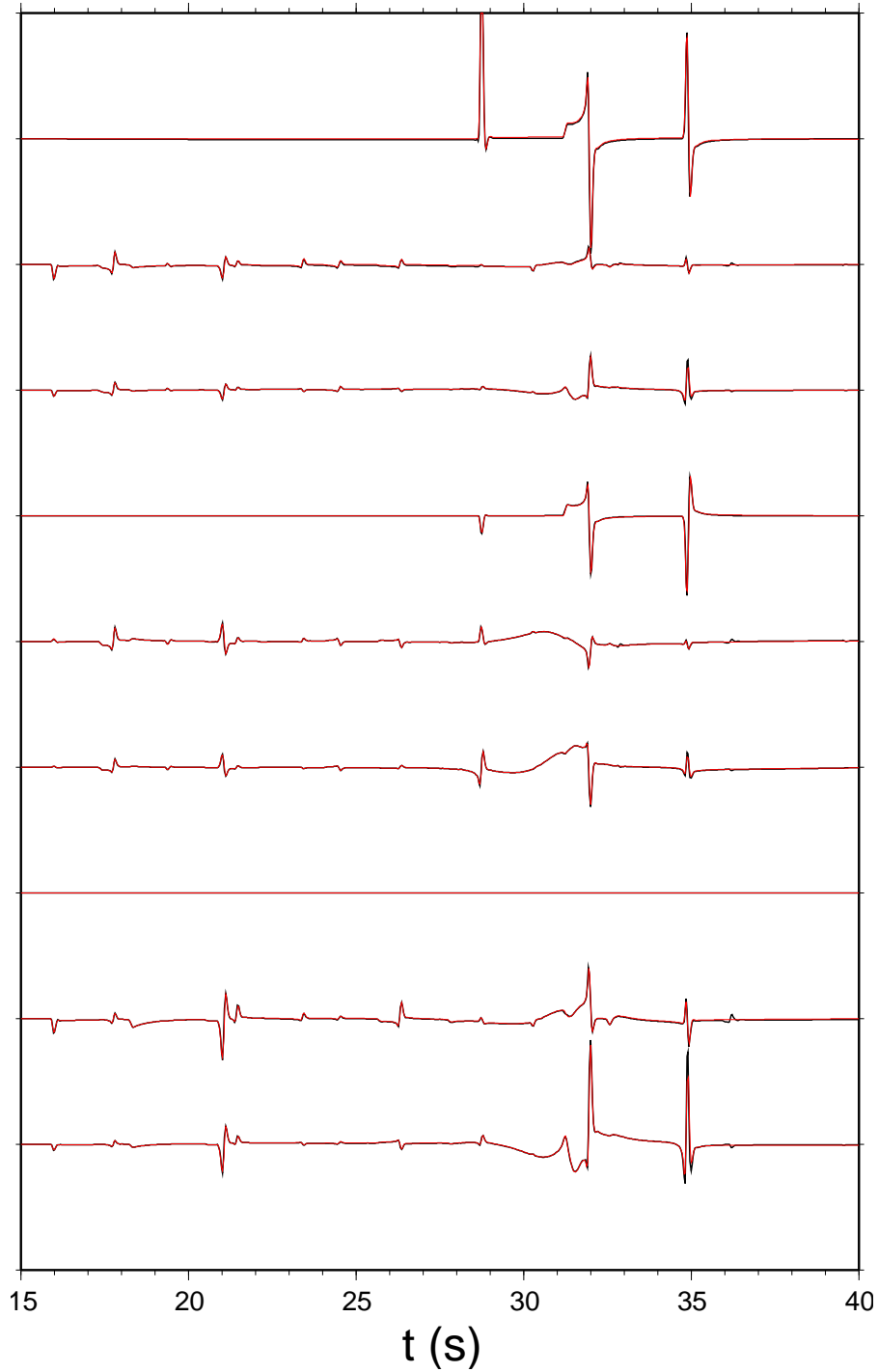
Figure 4.10: Comparison of Greens functions calculated by FK method (heavy lines) with those by GRT (red lines). The velocity model is a 30-km-thick layer (V_p=6.3 km/s and V_s=3.6 km/s) over a half space (V_p=8.1 km/s and V_s=4.5 km/s). The source is at 10 km depth and the distance range is 100 km. The components are, from the bottom to top, ZDD, RDD, TDD, ZDS, RDS, TDS, ZSS, RSS, and TSS. Total of 14 primary rays are used in GRT calculation which takes about 0.1 sec on a SUN-Ultra. FK takes about 1.4 sec.
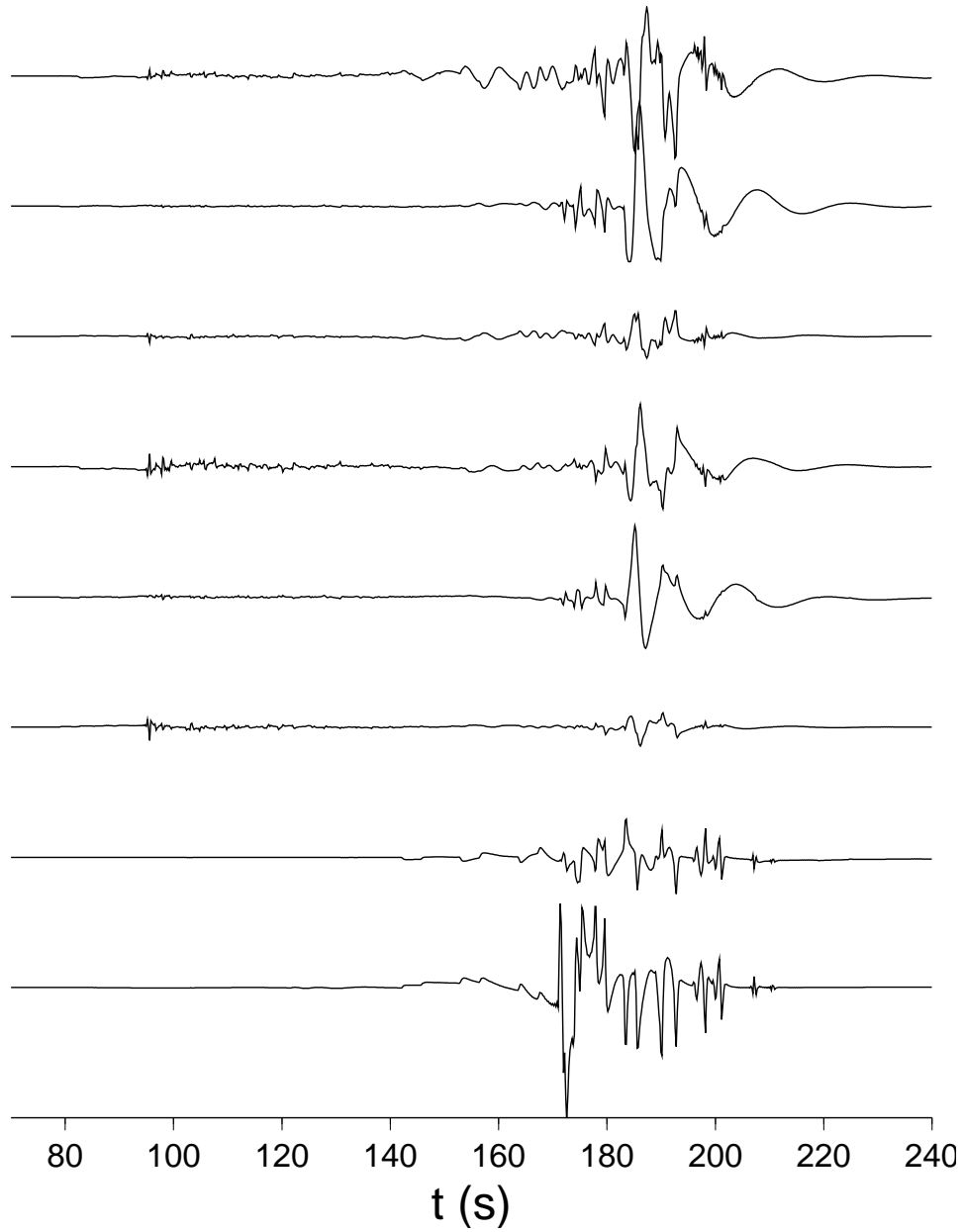
Figure 4.11: Greens' function at distance of 600 km for previous model. Wavenumber sampling interval dk is set to 0.005 km^{-1}.
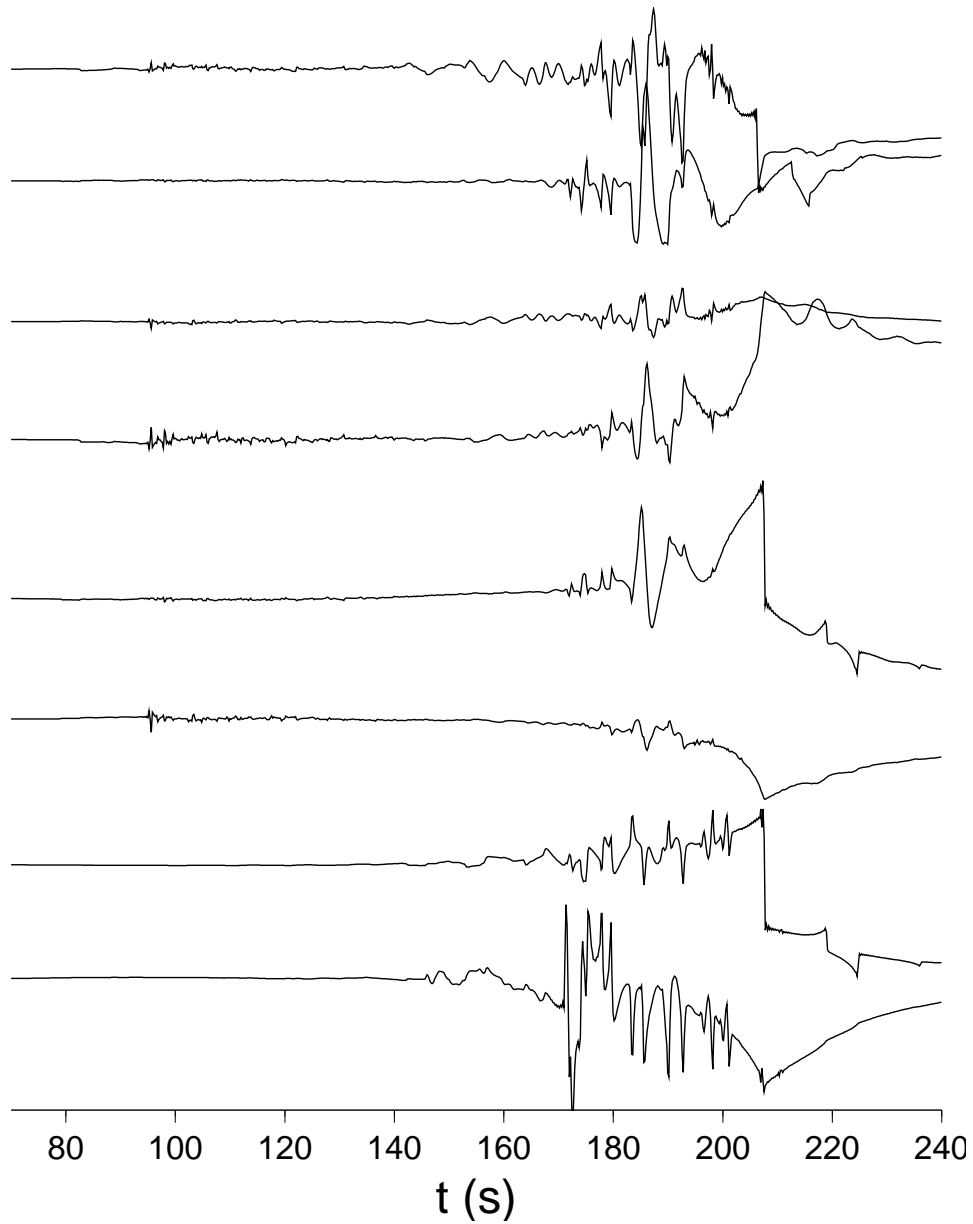
Figure 4.12: Same velocity model and distance range as in Figure 4.11, but shows the problem of space-aliasing in waveforms when dk is not small enough ($dk = 0.01$ km^{-1}).

4.5 Differential seismograms

4.5.1 Analytical derivatives of propagator matrices and source terms

4.5.2 Analytical solution

4.5.3 Implementation and tests

4.5.4 Application to waveform inversion

4.6 Exercises

1. Download the Frequency-Wavenumber synthetic seismogram package from http://www.eas.slu.edu/People/LZhu/home.html and compile the program *fk*. Use it to compute the Green's functions shown in Fig. 4.9. Do the same using the GRT program *aser*. Plot the waveforms to compare the results from the two methods.

2. Use *fk* and *aser* to compute the Green's functions shown in Fig. 4.10. Plot the waveforms to compare the results from the two methods.

Chapter 5

Regional Distance Seismic Waveforms

5.1 Local distances

5.2 Regional distances
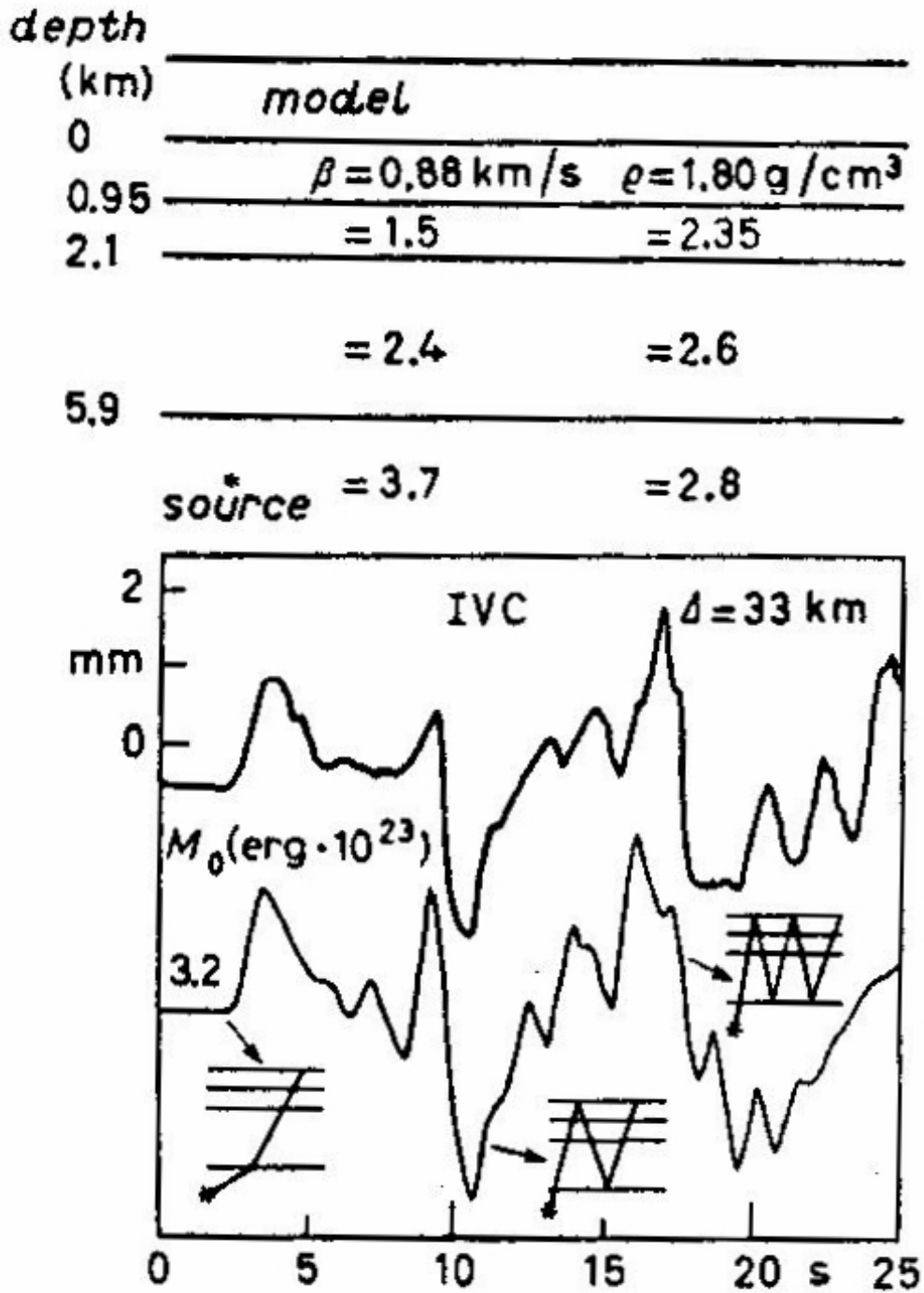
Figure 5.1: Comparison of synthetics with strong-motion record of station IVC of an earthquake at Brawley, CA, in Nov. 1976. From Helmberger [1983].
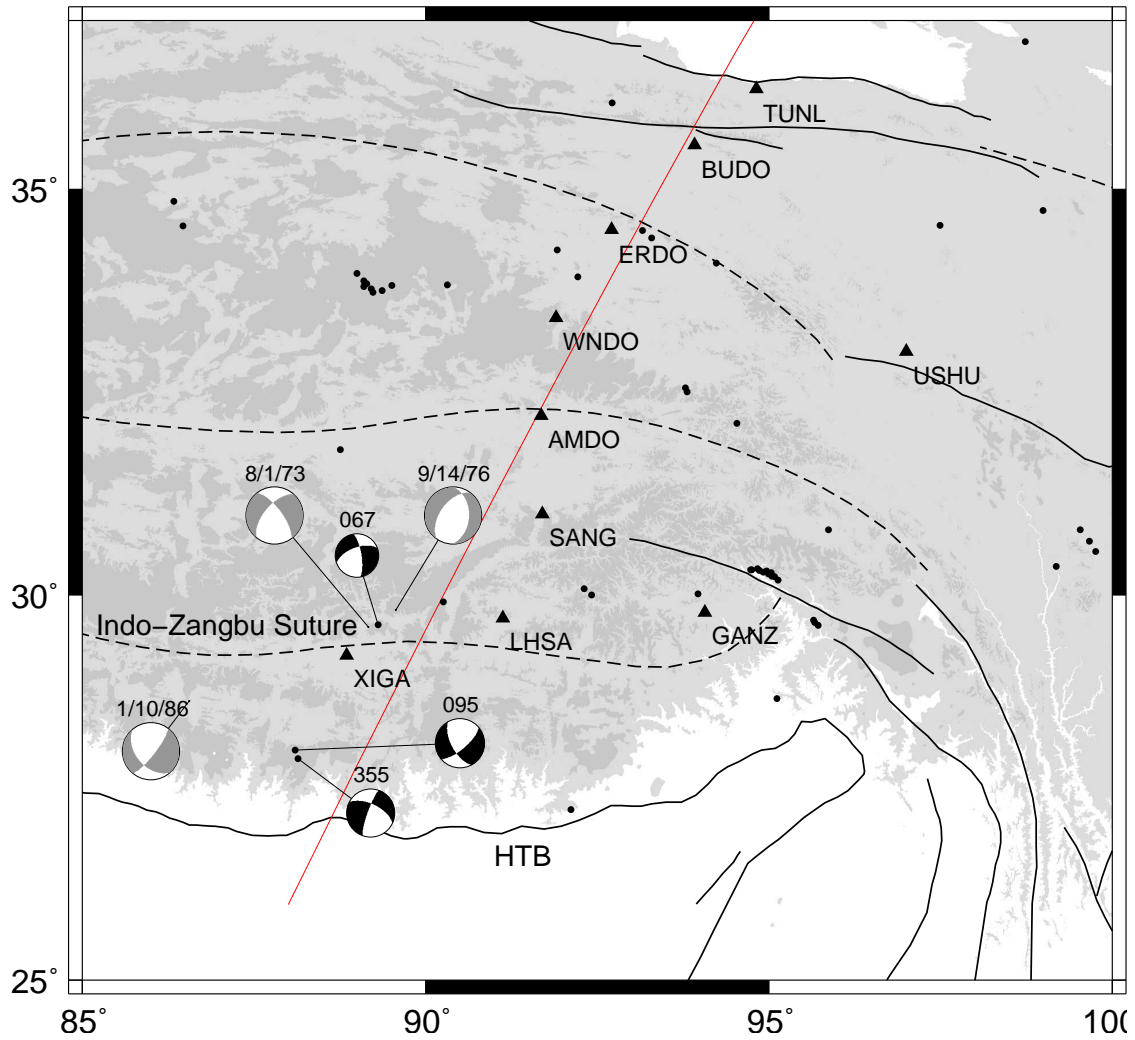
Figure 5.2: Map of eastern Tibet showing major tectonic boundaries and the station locations (triangles) of the 1991-1992 Tibet PASSCAL experiment. Shading indicates elevation above 3 km. Darkly shaded focal spheres are for sub-crustal events analyzed in this study. Lightly shaded focal spheres are from Molnar and Chen [1983] and the Harvard CMT solution (for event on 1/10/86). All of them are located at intermediate depths.
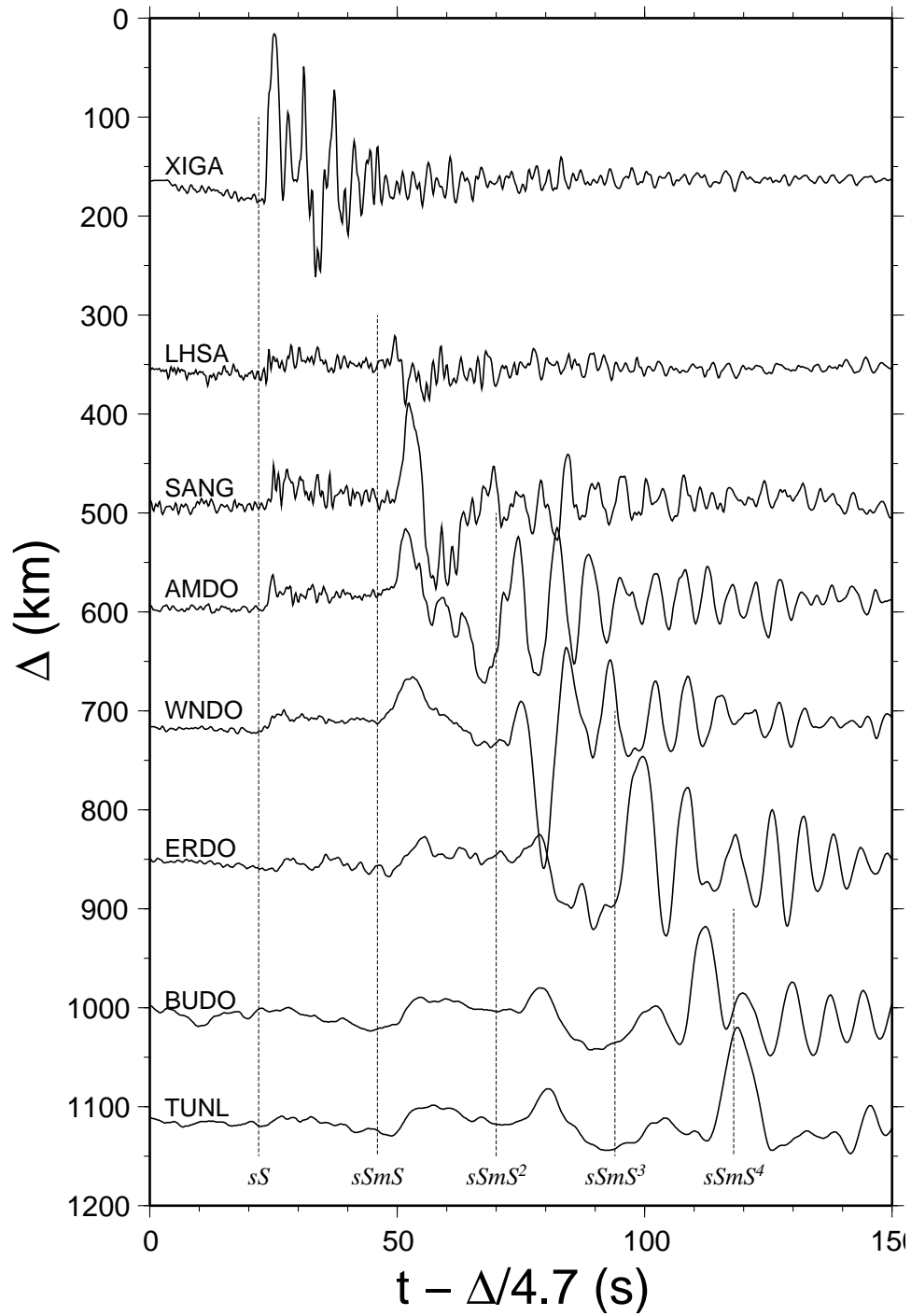
Figure 5.3: *SH* displacements of event 355. Note the sharp onsets of *S* waves beyond 300 km. Crustal multiples up to the 4th order are indicated by the evenly separated dashed lines.
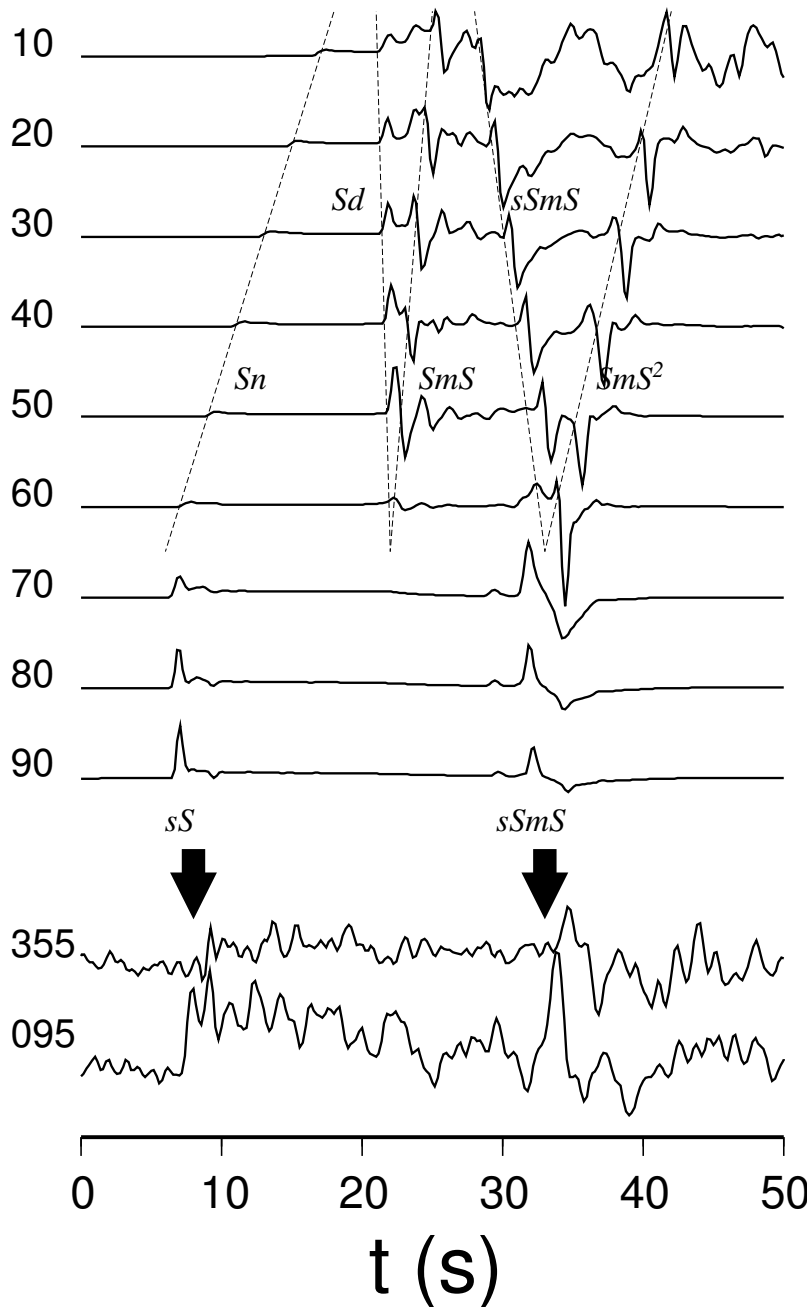
Figure 5.4: *SH* components of the Green's functions of a strike-slip source at different depths (numbers in km left of the trace). The velocity model is T93 with the Moho at 65 km depth. The Distance range is 350 km. Also shown in the figure are observed *SH* displacements of Events 355 and 095 recorded at station LHSA at the same distances.
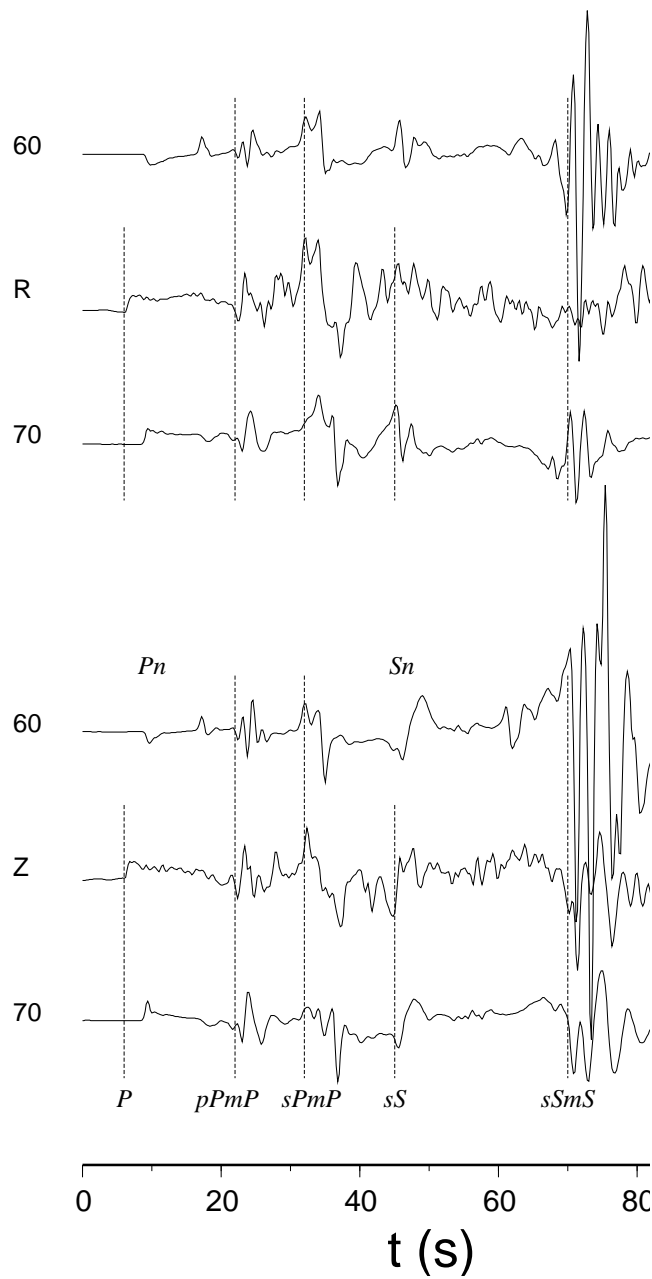
Figure 5.5: Comparison of the vertical and radial displacements from Event 355 at station LHSA with synthetics from a source above (60 km) and below (70 km) the Moho. The synthetics are constructed using the source mechanisms obtained from the waveform inversion at the corresponding depth.
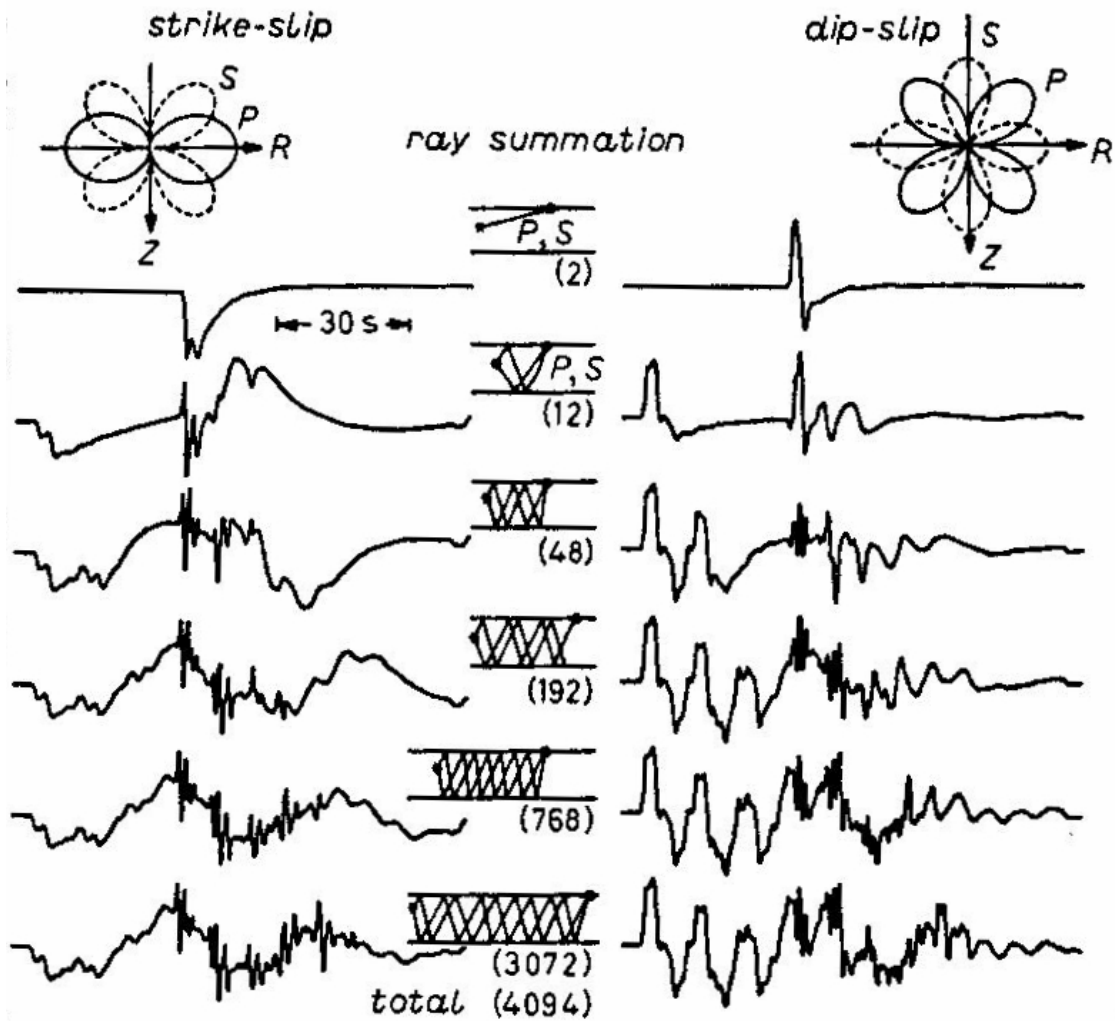
Figure 5.6: Vertical components of motion as a function of number of generalized ray summed. The epicentral distance is 1000 km. From Helmberger [1983].
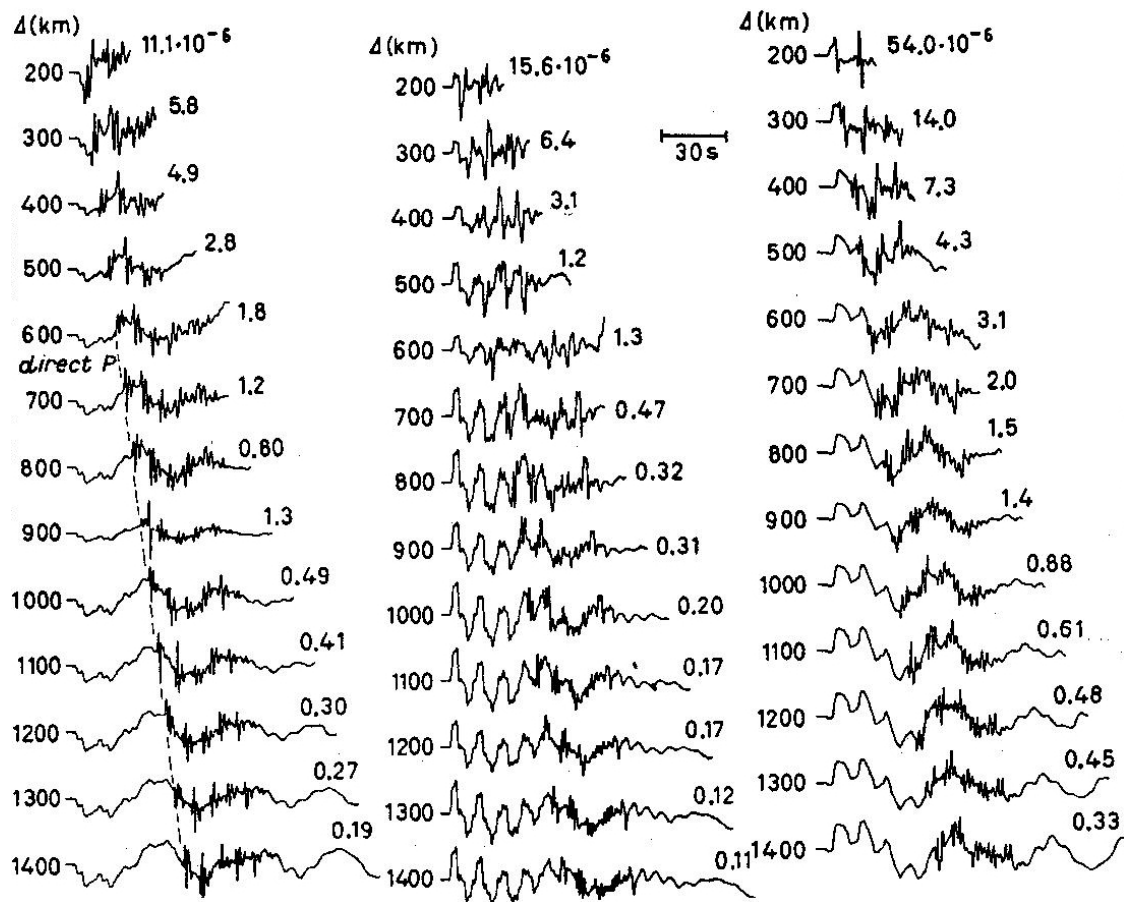
Figure 5.7: Profile of vertical displacements for the three fundamental faults. The Green's functions have been convolved with a 1.5 s trapezoid source time function. From Helmberger [1983].
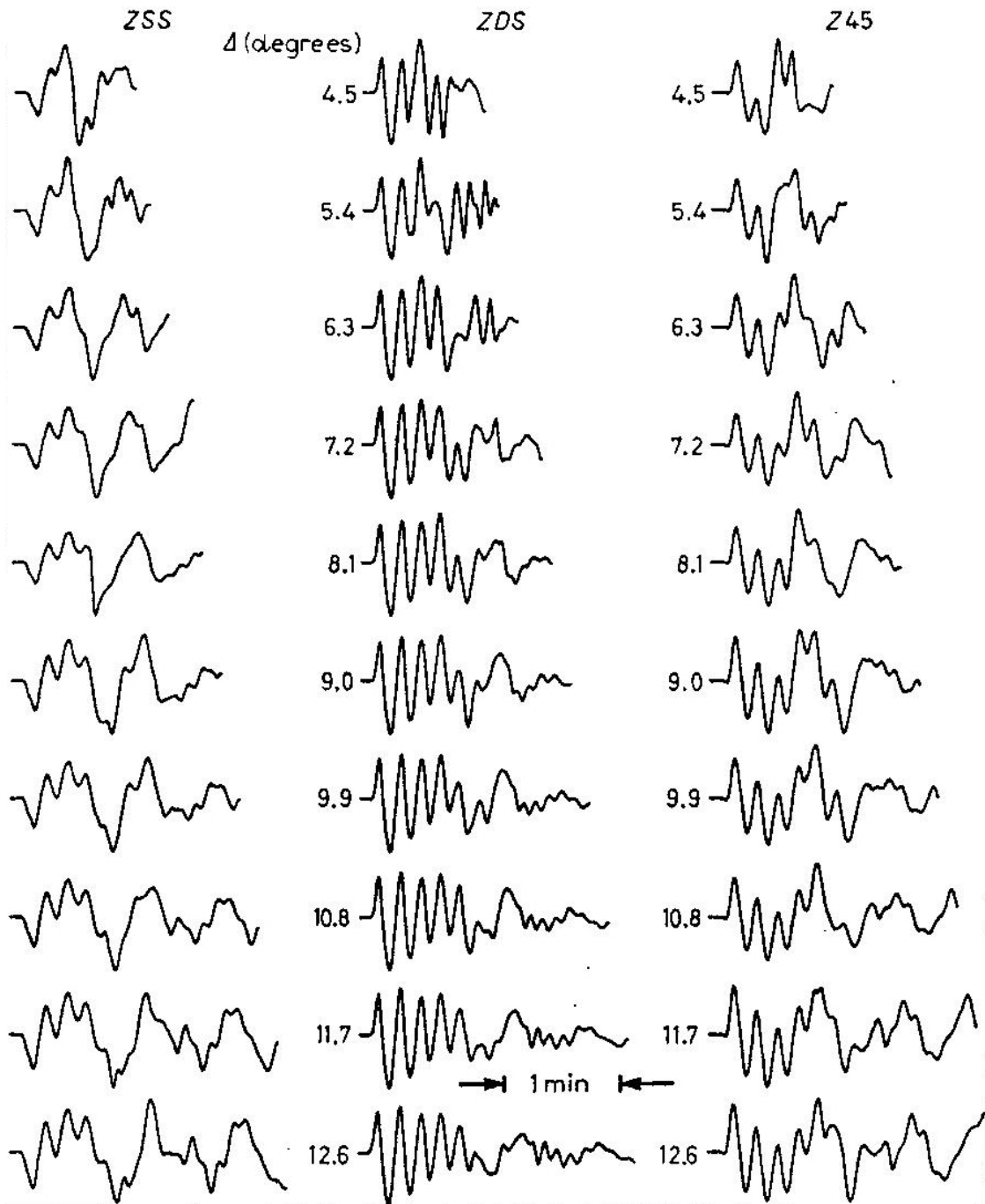
Figure 5.8: Profile of vertical displacement for the three fundamental faults. The Green's functions have been convolved with a 3 s trapezoid source time function and a WWSSN long-period instrument response. From Helmberger [1983].
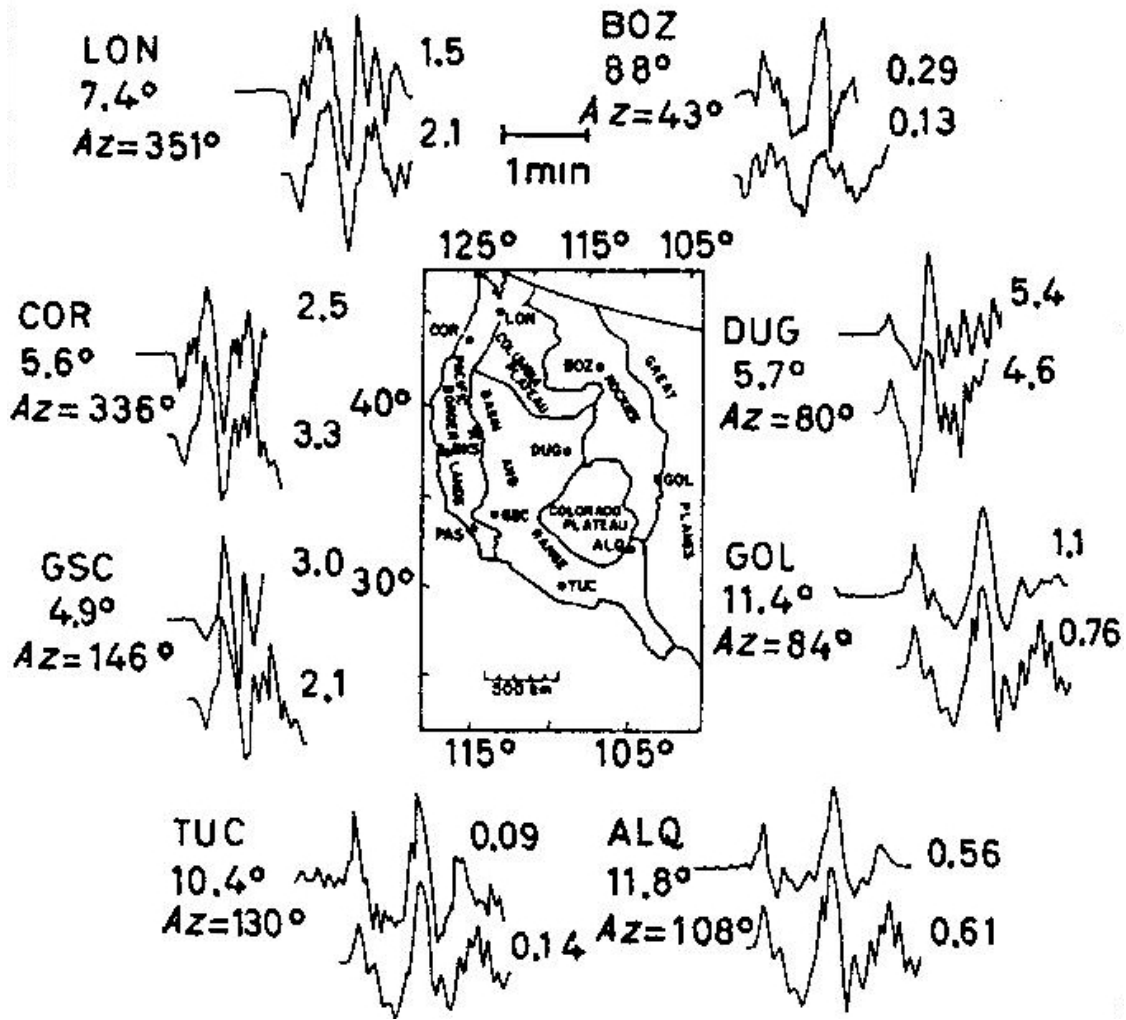
Figure 5.9: The vertical *Pnl* waveforms of the 1966 Truckee earthquake. The strike-slip focal mechanism (strike 43°N, dip 76°SE, and rake -11°) of the event has two nodal planes which project through station TUC and BOZ. From Helmberger [1983].
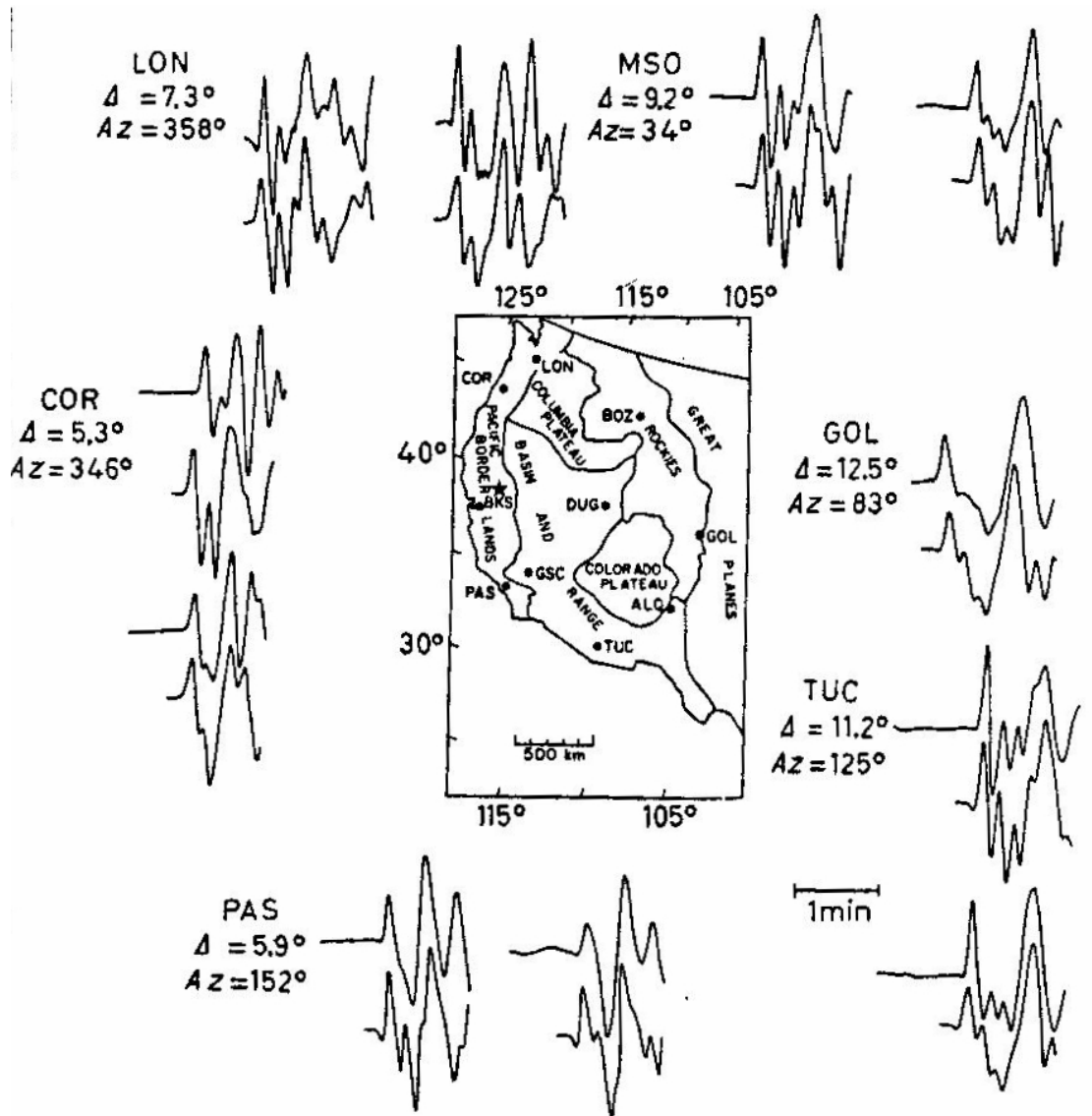
Figure 5.10: Filtered data and synthetics from the Oroville earthquake. At all stations except GOL both the vertical (the first trace pair) and radial components are shown. The focal mechanism (strike 204°, dip 66°, rake 275°) generates positive first-motions at all station in regional distances as opposed to those observed teleseismically. From Helmberger [1983].

64
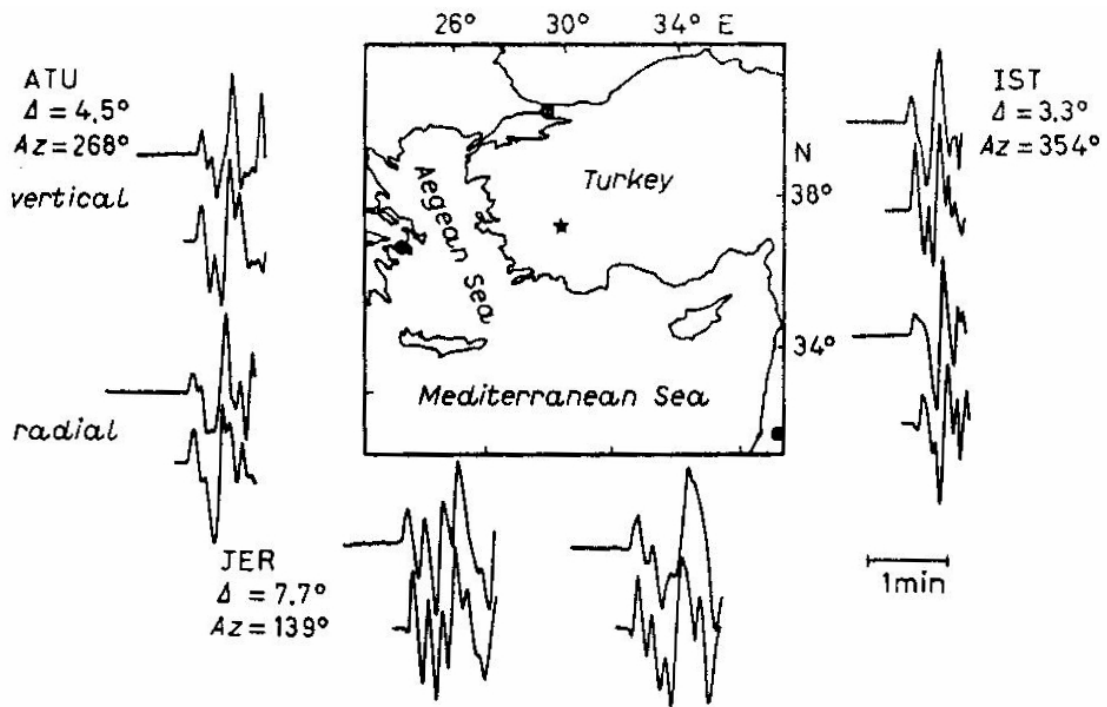
Figure 5.11: Filtered data and synthetics for both the vertical and radial components from an earthquake in Turkey (strike 131°, dip 68°, rake 272°). From Helmberger [1983].

Chapter 6

Upper-mantle Distance Waveforms

6.1 Earth flattening transformation

The Earth flattening transformation (EFT) transforms a sphere with constant velocity V_0 to a half-space with variable velocity $V(z)$ through

$$z = a \ln \frac{a}{r}, \tag{6.1}$$

$$V(z) = \frac{a}{r} V_0 = V_0 e^{z/a}. \tag{6.2}$$

It can be shown that the above transformation gives the same travel-time at the same epicentral distance for the half-space as for the sphere (kinematically equivalent).

It can be further shown that if we transform the density according

$$\rho(z) = \left(\frac{r}{a}\right)^5 \rho_0, \tag{6.3}$$

the SH-waveform for the half-space is the same as for the sphere (dynamically equivalent) [Biswas and Knopoff, 1970]. For the P-SV system, there is no exact transformation [e.g. Chapman, 1973, Bhattacharya, 1996].

For a sphere with radially varying velocity and density, we can divide the sphere into many thin shells and do EFT to each shell, using

$$dz = \frac{a}{r} dr. \tag{6.4}$$

Fig. 6.1 shows IASPEI91 upper-mantle seismic velocity model before and after the Earth flattening transformation.
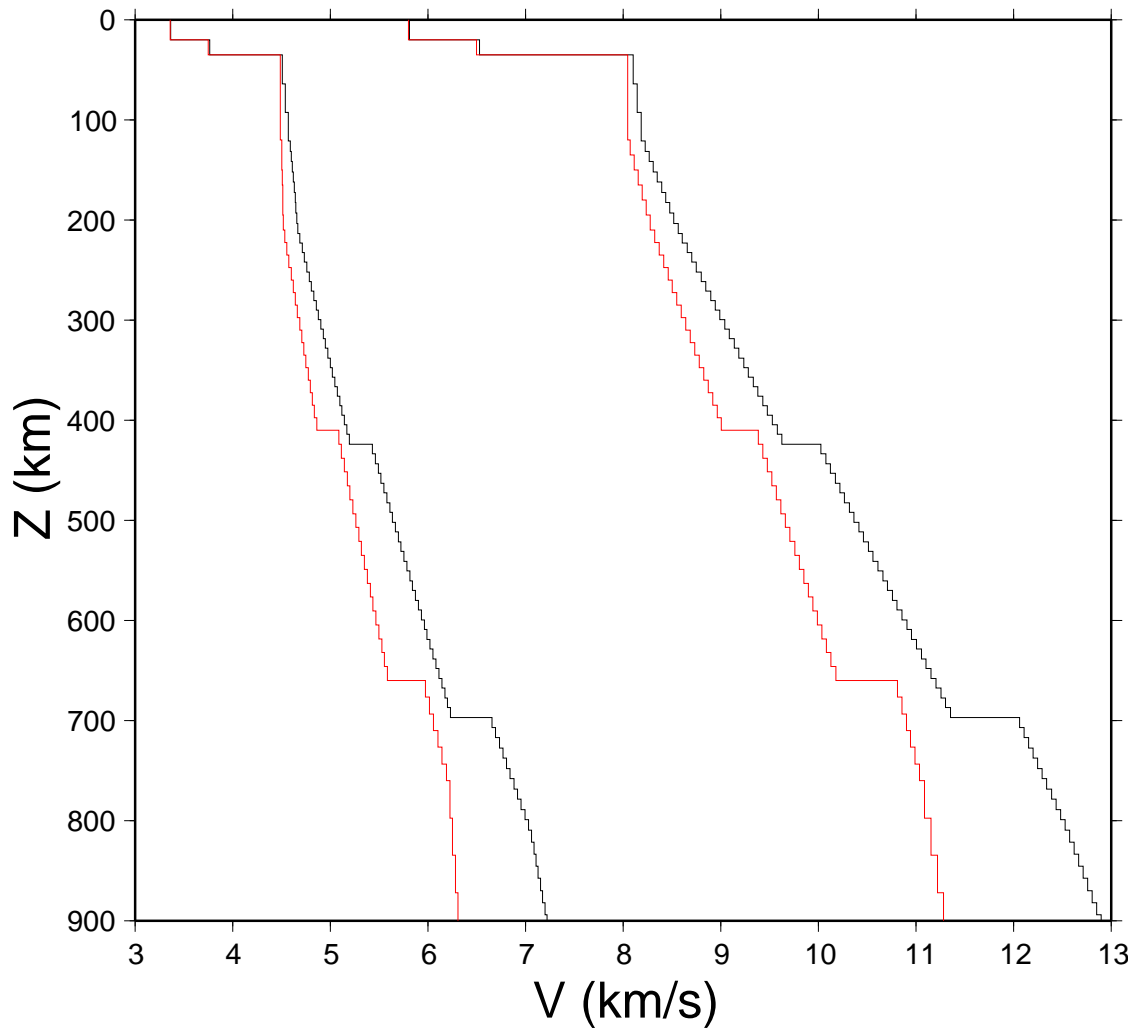
Figure 6.1: IASPEI91 upper-mantle seismic velocity model before the Earth flattening transformation (red lines) and after (black lines).
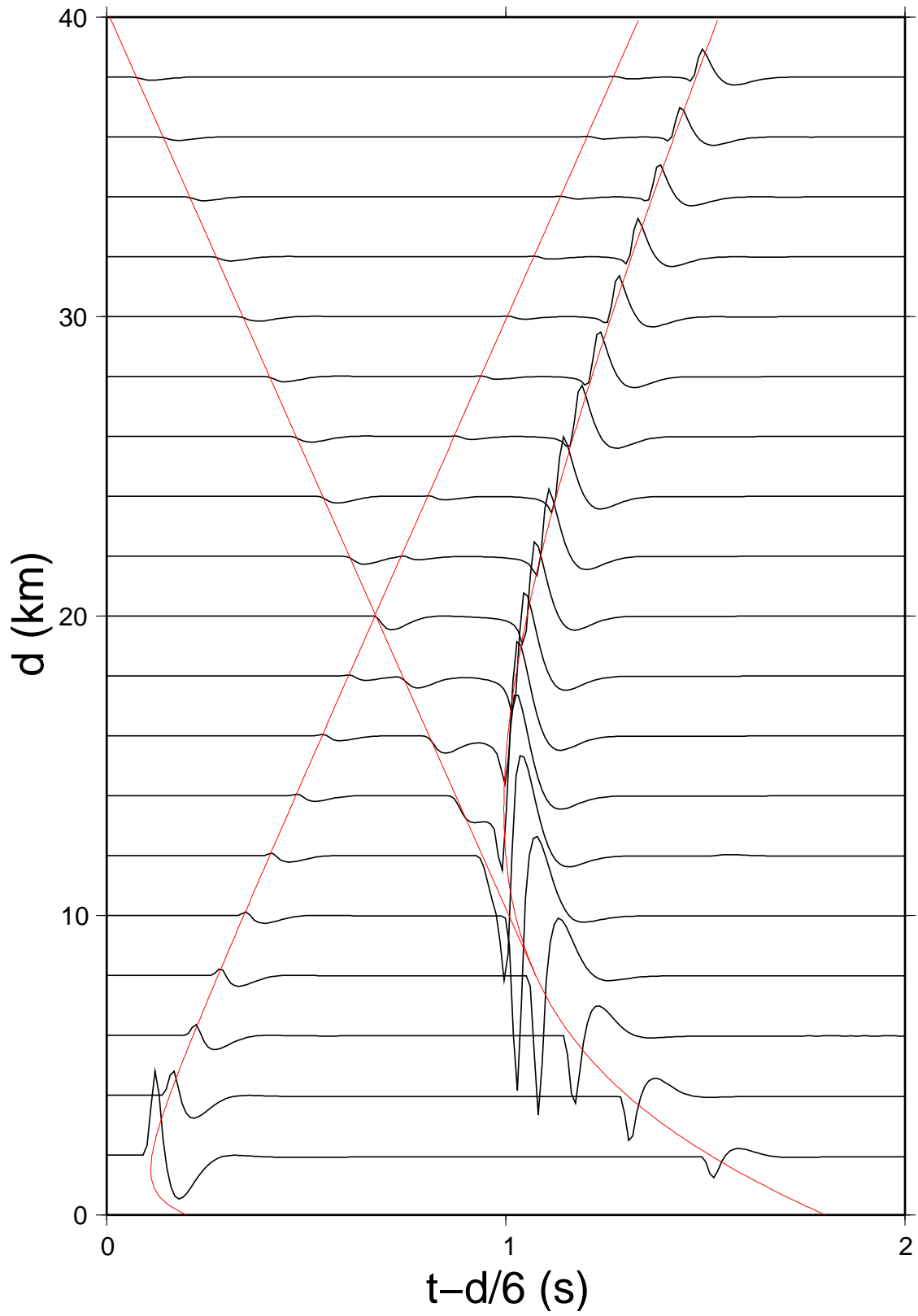
Figure 6.2: Direct, reflected and head waves for a two liquid half-space model.

68
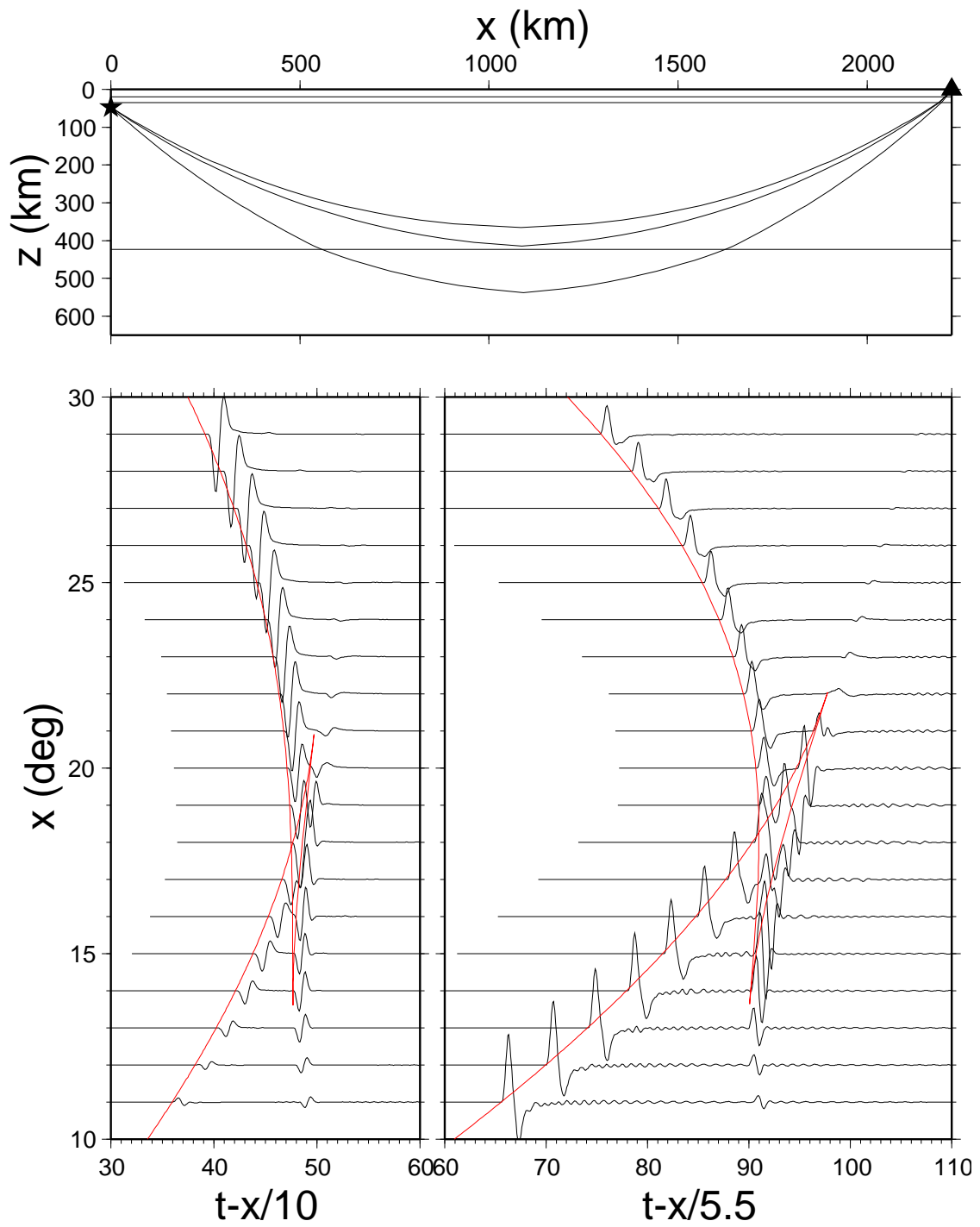
Figure 6.3: P (left) and SH (right) triplicated waveforms due to the 410 discontinuity.
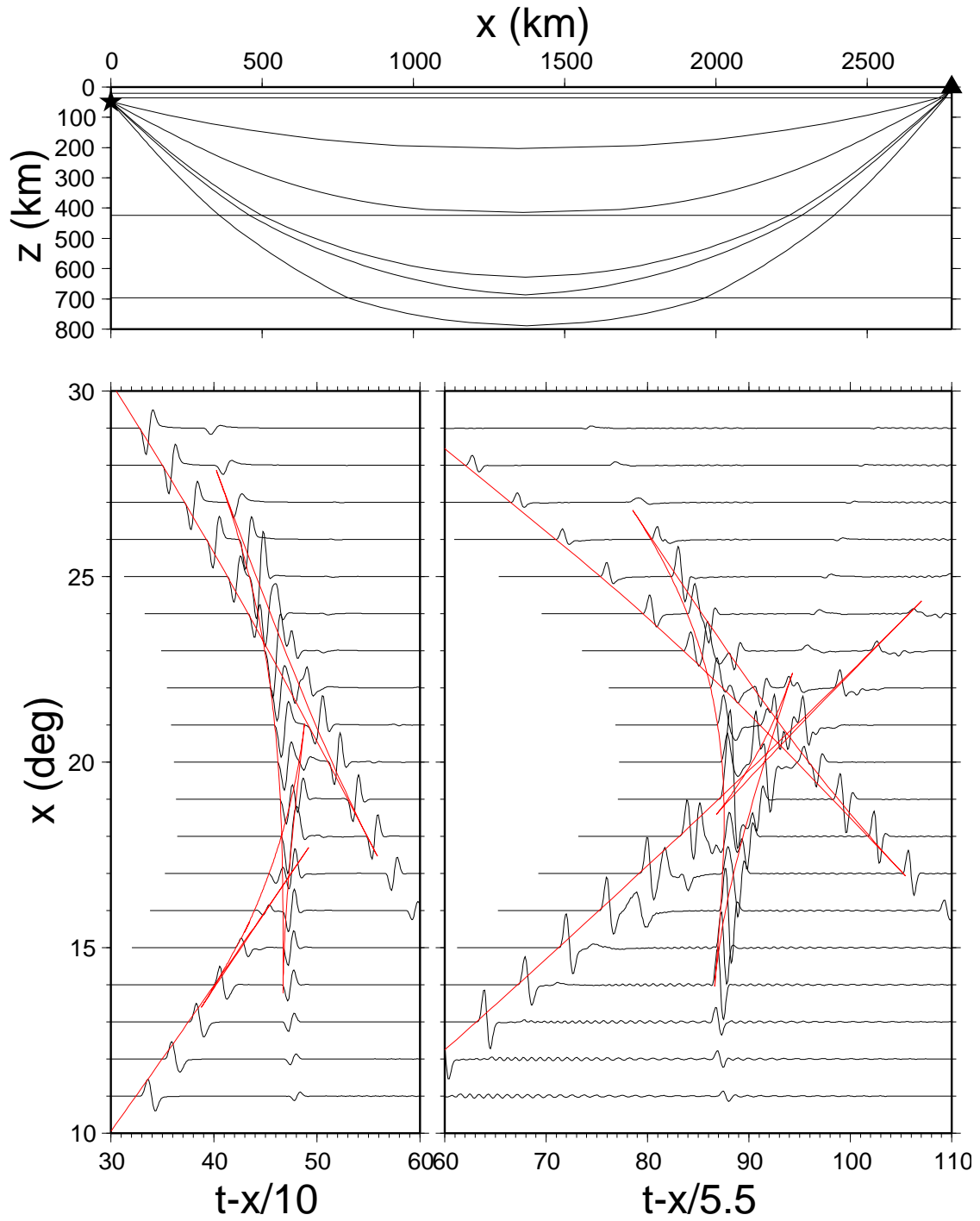
Figure 6.4: Triplicated P (left) and SH (right) waveforms for the IASPEI91 velocity model.
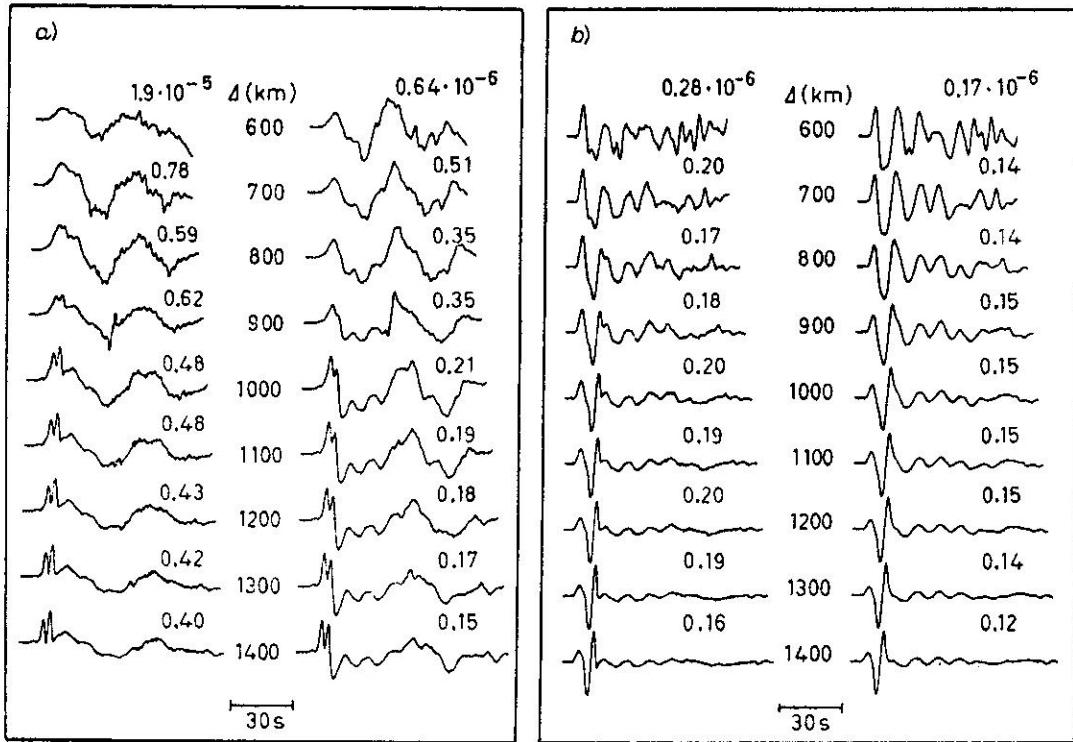
Figure 6.5: Vertical component seismograms going from P_{nl} domination at regional distances to P and long-period at intermediate distances, a) strike-slip and b) dip-slip.

71

regional

$t^* = 0, M_0 = 1.2 \cdot 10^{25}$

upper mantle

$t^* = 1.3, M_0 = 0.56 \cdot 10^{25}$

ALQ
$\Delta = 12°$
$Az = 108°$
$M_0 = 2.0$
$\cdot 10^{25}$

FSJ
$= 16°$
$= 168°$
$= 0.60$

DAL
$= 20°$
$= 102°$
$= 0.55$

GOL
$= 12°$
$= 84°$
$= 1.41$

LUB
$= 16°$
$= 106°$
$= 0.64$

FLO
$= 23°$
$= 82°$
$= 0.30$

COR
$= 6°$
$= 337°$
$= 0.93$

JTC
$= 19°$
$= 112°$
$= 0.49$

MDS
$= 23°$
$= 70°$
$= 0.85$

GSC
$= 5°$
$= 146°$
$= 1.4$

FFC
$= 20°$
$= 32°$
$= 0.46$

YKC
$= 23°$
$= 8°$
$= 0.51$

0   60 s

0   30 s
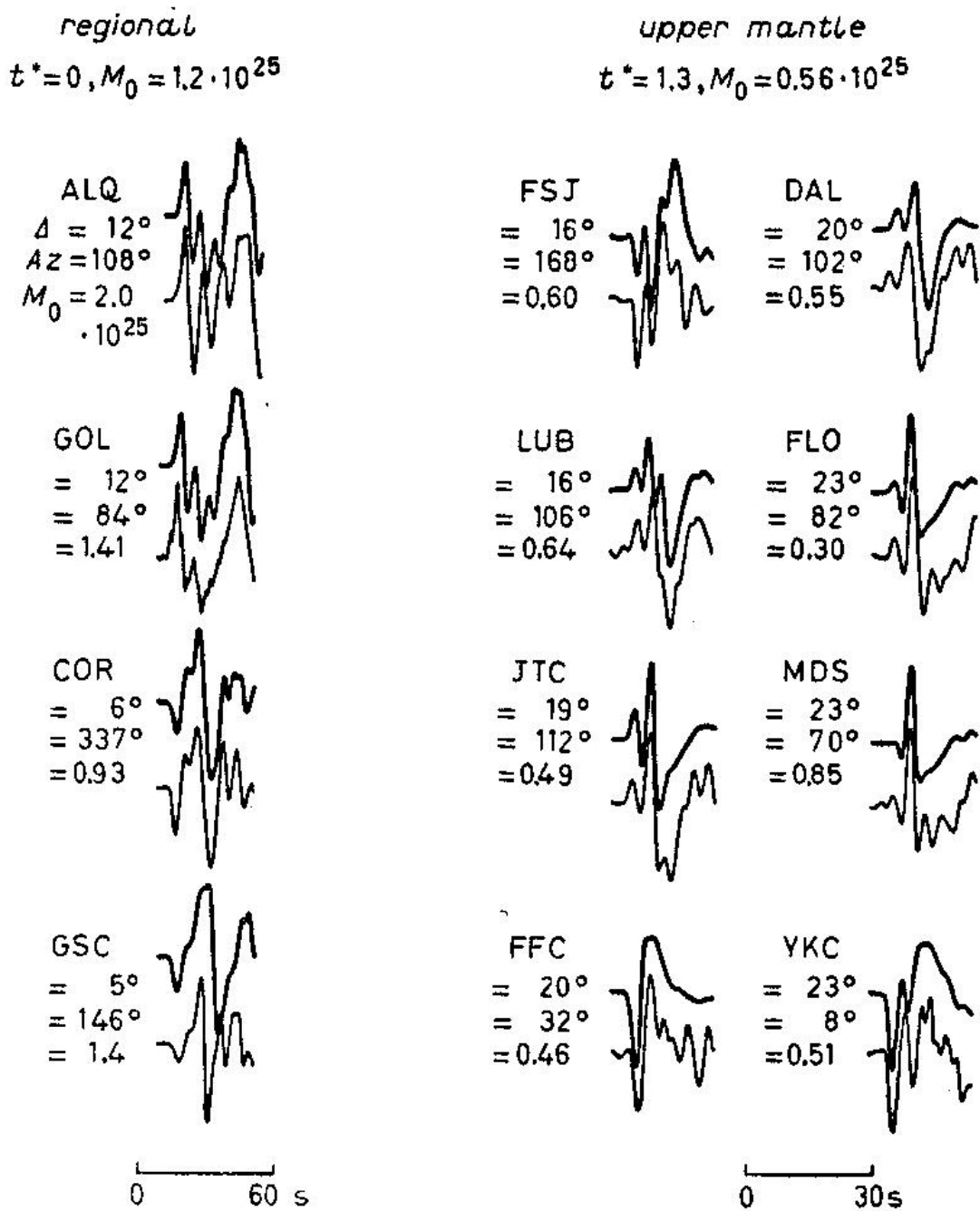
Figure 6.6: Comparison of synthetics with data of 9/12/1966 Truckee earthquake (strike 48°, dip 80°, and rake 0°) at regional and upper-mantle distances. From Helmberger [1983].

72

6.2 Velocity discontinuity and triplication

6.3 Upper-mantle structure from modeling triplicated waveforms

See Brudzinski and Chen [2003]

Chapter 7

Teleseismic Waveforms

7.1 Computing teleseismic synthetics

7.1.1 Full waveforms using normal-mode summation, DSM, and FK

7.1.2 Construction of teleseismic P-wave with GRT

$$u_z = \frac{M_0 R_{pz}(p_0)}{4\pi\rho R} \sum_{j=1}^{3} A_j \left[C_j(p_0)\delta(t) + C_j(p_0)R_{pp}(p_0)\delta(t - \Delta t_1) + SV_j(p_0)\frac{\eta_\alpha}{\eta_\beta}R_{sp}(p_0)\delta(t - \Delta t_2) \right].$$
$$(7.1)$$

7.2 Determining earthquake moment tensors and focal depth

7.3 Determine upper mantle structure

See Tan and Helmberger [2006].

7.4 Teleseismic receiver functions

.
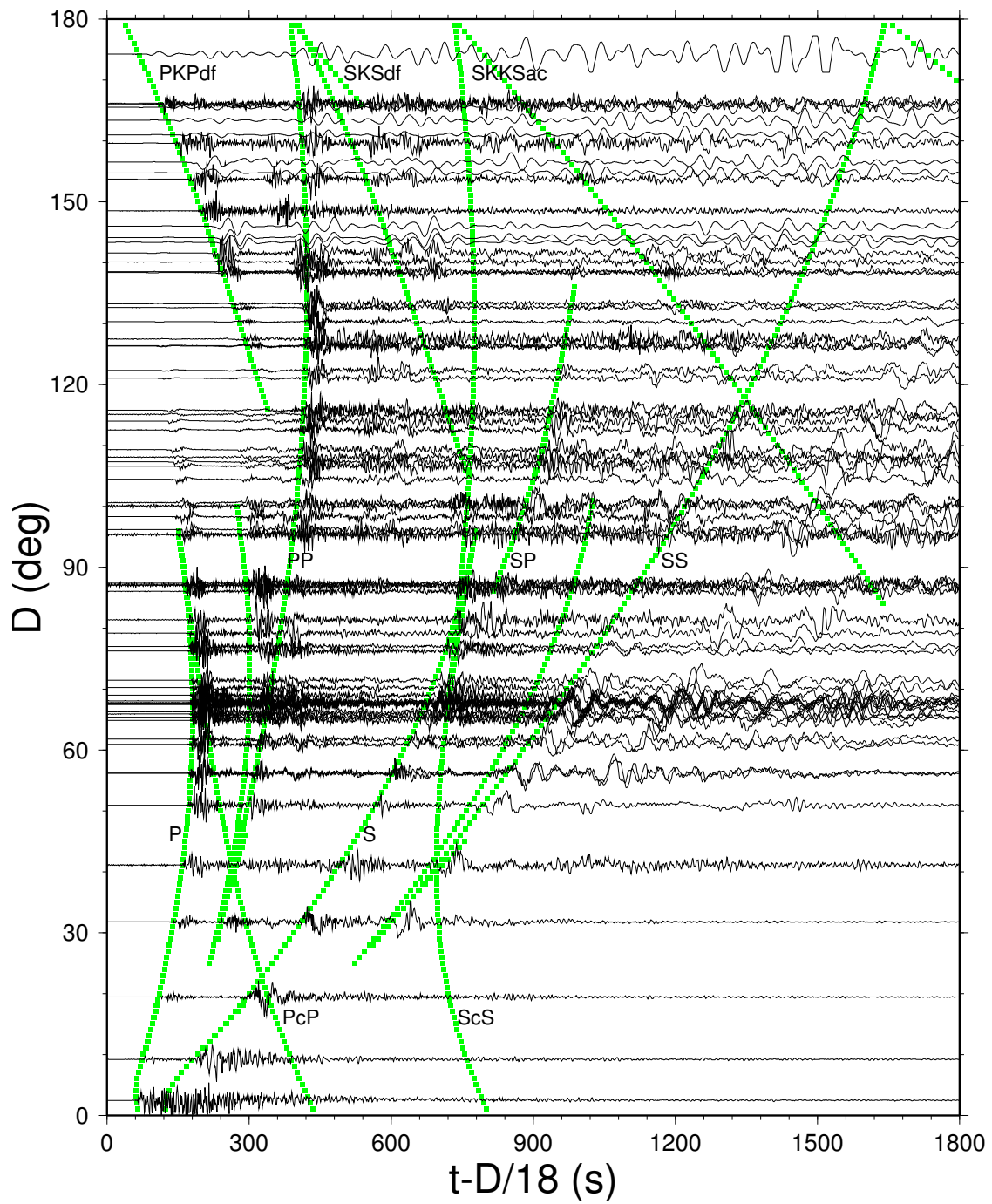
Figure 7.1: Vertical component record section of the 1994 Bolivia deep earthquake.
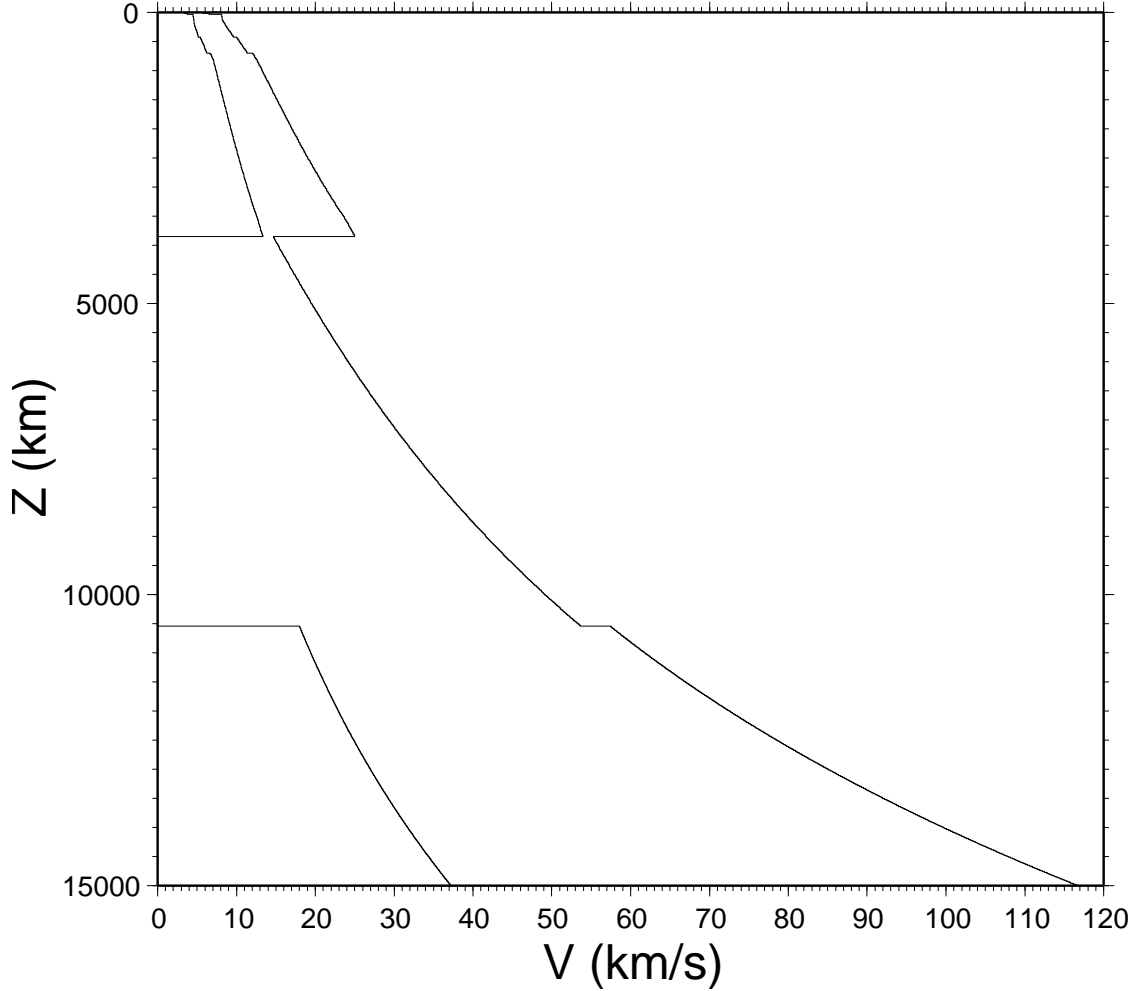
Figure 7.2: IASPEI91 velocity model after EFT.

7.4.1 Computing receiver functions

The vertical and radial components of teleseismic P wave:

$$Z(t) = S(t) \otimes E_Z(t), \tag{7.2}$$
$$R(t) = S(t) \otimes E_R(t), \tag{7.3}$$

where $S(t)$ is the time history of the incident P wave, which contains the earthquake source time function and the propagation effect through the mantle. $E(t)$'s are the responses of structure beneath the seismic station. The above equations suggest that the local structure responses can be isolated from three-component teleseismic recordings using spectrum division

$$\frac{R(\omega)}{Z(\omega)} = \frac{E_R(\omega)}{E_Z(\omega)}. \tag{7.4}$$
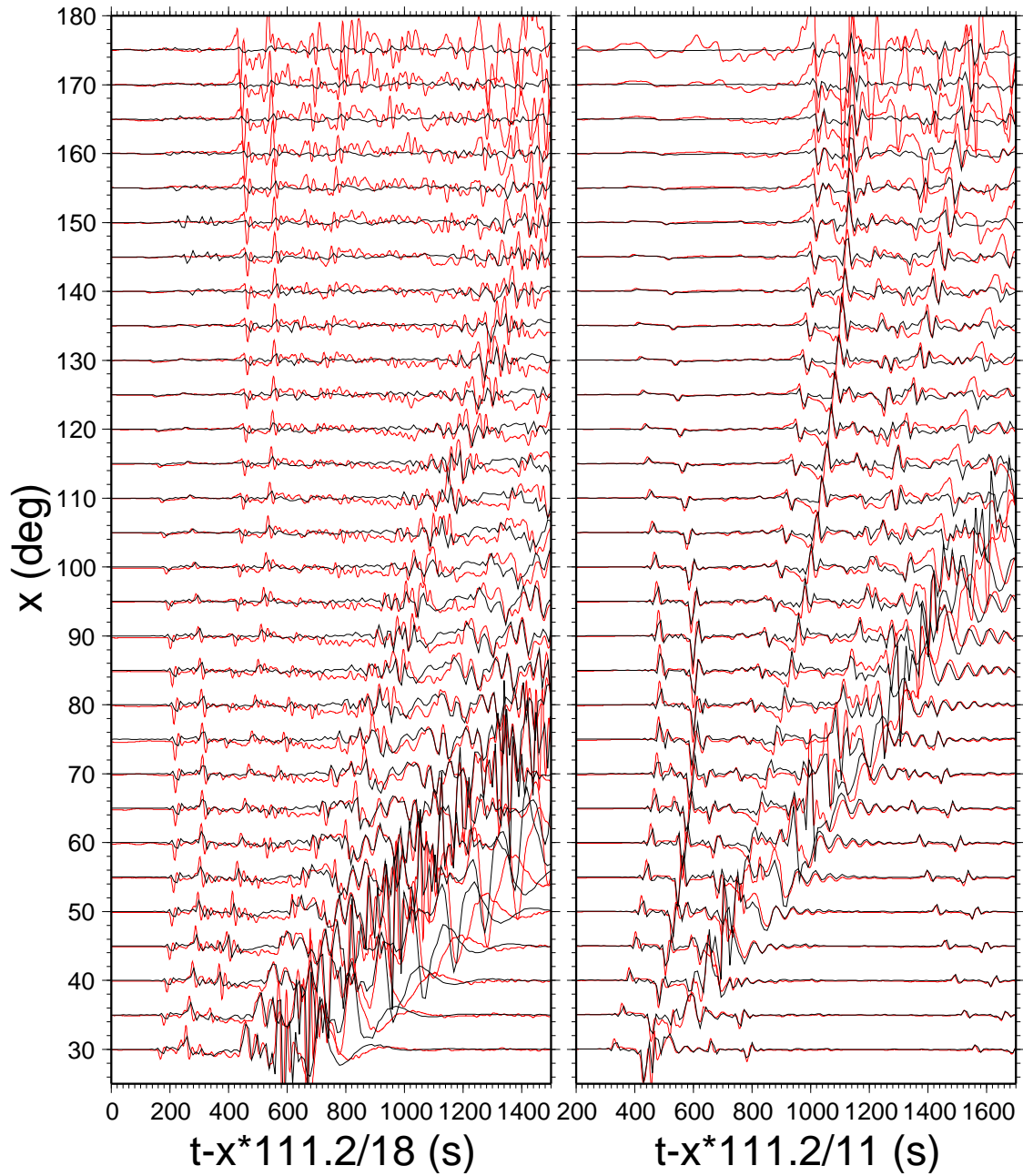
Figure 7.3: Vertical (left) and transverse (right) components of DSM (red) and FK (black) synthetics for the IASPEI91 model. A 20-sec-low-pass filter is applied.
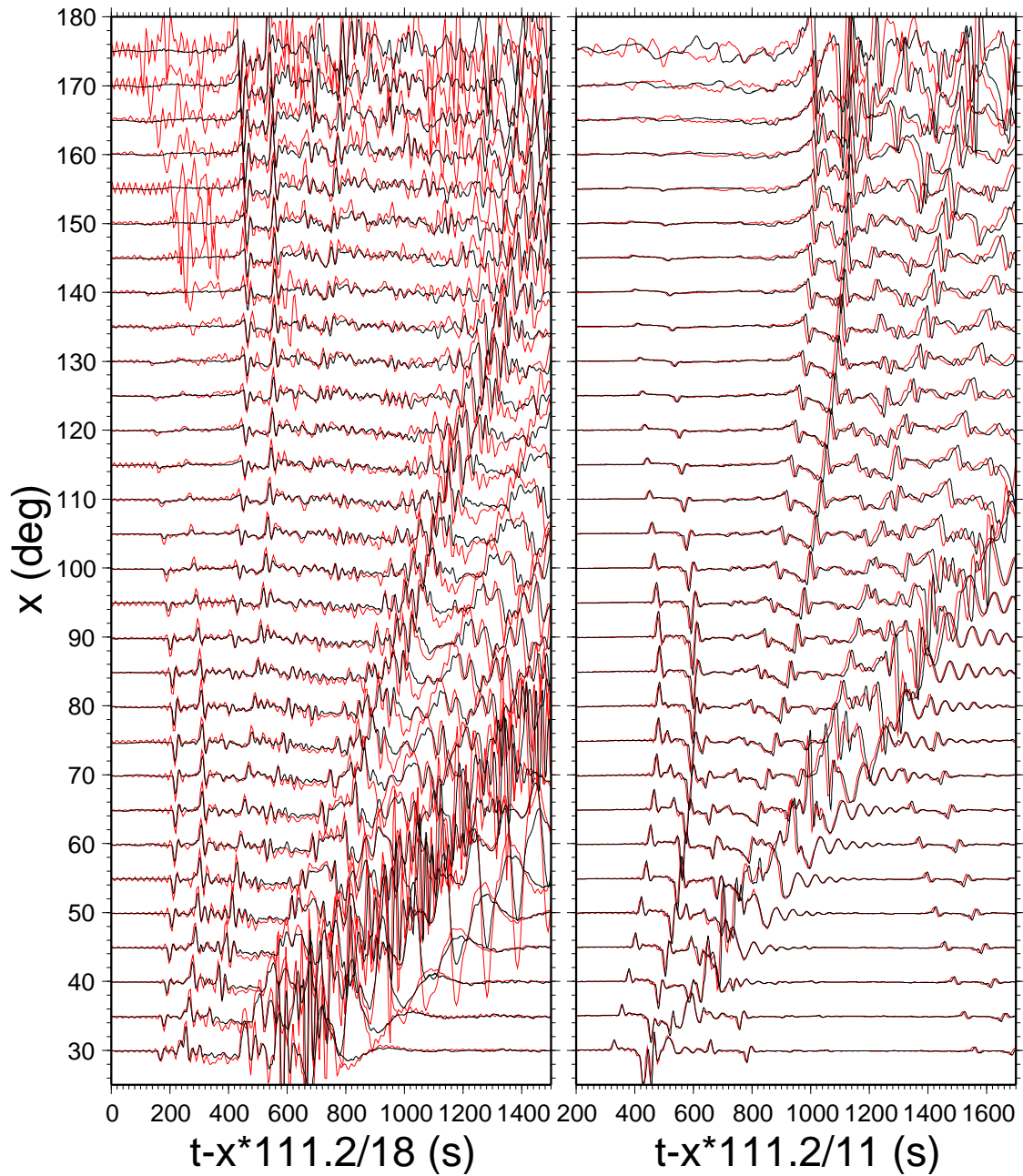
Figure 7.4: Vertical (left) and transverse (right) components of normal-mode (red) and DSM (black) synthetics for the IASPEI91 model. A 20-sec-low-pass filter is applied.

The corresponding time sequence is called the receiver function [Langston, 1977].

$$r(t) = \int \frac{R(\omega)}{Z(\omega)} e^{i\omega t} d\omega. \tag{7.5}$$

Fig. 7.9 shows the vertical and radial responses of a simple crustal model and the corresponding receiver function for a incident teleseismic P wave with a ray parameter of 0.06 km/s. Receiver functions are dominated by P-to-S converted phases at various velocity interfaces (e.g. Moho) and their multiples.

Computing receiver functions can be done in the frequency domain (spectrum division) or time domain (Wiener filtering). Both methods pre-whiten the signal to suppress spectrum "holes" to make the computation stable, see the usage of program *decon* for details. Kikuchi and Kanamori [1982] introduced an iterative time-domain deconvolution method that works well for noisy data. It has been implemented in program *iter_decn*.

Some real examples of receiver functions at station PAS are shown in Fig. 7.10

7.4.2 Inversion for 1-D velocity structure

Receiver functions calculated from broadband seismic records contain many P-to-S converted phases produced by the crustal structure under the station. We can utilize a time domain inversion technique [Owens et al., 1984, Ammon et al., 1990], which inverts the receiver function for a one-dimensional velocity structure beneath the station. By using a matrix formalism for propagation of elastic waves in stratified medium, theoretical receiver functions and their partial differentials with respect to elastic parameters m_i in each layer can be calculated [Kennett, 1983, Randall, 1989]. A set of linearized equations can then be constructed from a Taylor expansion,

$$\frac{\partial r(t)}{\partial m_i} \Delta m_i = r^{obs}(t) - r^{cal}(t), \tag{7.6}$$

which can be solved iteratively to get the one-dimensional velocity structure when the theoretical receiver functions match the observations. Fig. 7.11 shows an example using a temporary station deployed on the Tibetan plateau [Zhu et al., 1993]. In general, such inversion results are very non-unique because receiver function waveforms are more sensitive to velocity changes across discontinuities at different depths than to the velocities themselves.

7.4.3 Estimate crustal thickness and V_p/V_s ratio

Since Moho is usually the largest velocity discontinuity in the crust, the most prominent phase in the first 10 s of a radial receiver function is the Moho P-to-S conversion Ps. If we simplify the crust as one layer with a P velocity of V_p and an S velocity of V_s, The time

separation between Ps and P can be used to estimate crustal thickness,

$$H = \frac{t_{Ps}}{\sqrt{\frac{1}{V_s^2} - p^2} - \sqrt{\frac{1}{V_p^2} - p^2}}, \tag{7.7}$$

where p is the ray parameter of the incident wave. An advantage of this method is that because the P-to-S conversion point is close to the station (usually within 10 km laterally), the estimation is less affected by lateral velocity variations and thus provides a good point measurement. One problem is the trade-off between the thickness and crustal velocities. However, since t_{Ps} represents the differential travel time of S with respect to P wave in the crust, the dependence of H on V_p is not as strong as on V_s (or more precisely, on the V_p/V_s ratio κ).

For example, using a V_p of 6.3 km/s and V_p/V_s ratio of 1.732 for a 30-km-thick crust, one gets

$$\Delta H = \frac{\partial H}{\partial V_p} \Delta V_p = 4.3 \Delta V_p \text{ (km)},$$

which means that the uncertainty of H is less than 0.5 km for a 0.1 km/s uncertainty in V_p. However, the thickness is highly dependent on the V_p/V_s, as shown by

$$\Delta H = \frac{\partial H}{\partial \kappa} \Delta \kappa = -40.2 \Delta \kappa \text{ (km)},$$

i.e., a 0.1 change in κ can lead to about 4 km change in the crustal thickness. This ambiguity can be reduced by using the later phases which provide additional constraints

$$H = \frac{t_{PpPs}}{\sqrt{\frac{1}{V_s^2} - p^2} + \sqrt{\frac{1}{V_p^2} - p^2}}, \tag{7.8}$$

$$H = \frac{t_{PpSs+PsPs}}{2\sqrt{\frac{1}{V_s^2} - p^2}}, \tag{7.9}$$

so that both κ and H can be estimated [Zhu, 1993, Zandt et al., 1995, Zandt and Ammon, 1995].

In real situations, identifying the Moho Ps and the multiples and measuring their arrival times on a single receiver function trace can be very difficult due to background noise, scatterings from crustal heterogeneities, and P-to-S conversions from other velocity discontinuities. To increase the signal/noise ratio (SNR), one can use multiple events to stack their receiver functions. Such stacking is usually done in the time domain for a cluster of events [e.g., Owens et al., 1984]. Zhu and Kanamori [2000] proposed a straightforward H-κ domain stacking defined as

$$s(H, \kappa) = w_1 r(t_1) + w_2 r(t_2) - w_3 r(t_3), \tag{7.10}$$

where $r(t)$ is the radial receiver function, t_1, t_2 and t_3 are the predicted Ps, $PpPs$, and $PpSs+PsPs$ arrival times corresponding to crustal thickness H and V_p/V_s ratio κ, as given

in (7.7)–(7.9). The w_i are weighting factors, and $\sum w_i = 1$. The $s(H, \kappa)$ reaches a maximum when all three phases are stacked coherently with the correct H and κ (Figure 7.12). Advantages of this algorithm are that (1) large amounts of teleseismic waveforms can be conveniently processed; (2) there is no need to pick arrival times of different conversion phases; (3) by stacking receiver functions from different distances and directions, effects of lateral structure variation are suppressed and an average crustal model is obtained; and (4) uncertainties can be estimated from the flatness of $s(H, \kappa)$ at the maximum.

7.4.4 CCP stacking and imaging

Zhu [2000] developed a stacking and imaging technique called Common Conversion Point (CCP) stacking technique to image crustal structure when multiple stations are deployed close to each other so that the teleseismic rays to them crisscross in the crust. First the ray-path of the receiver function is calculated using a background velocity model. Then the amplitude at each point on the receiver function, after corrected for the incidence angle effect, is assigned to the corresponding location on the ray-path where the P-to-S conversion occurred, using its time delay with respect to the direct P. This amplitude represents the velocity change, or more precisely the impedance change, of the medium at the conversion point. The crustal volume is divided into certain size bins and all amplitudes in each bin are summed to obtain the average amplitude and variance. Fig. 7.13 shows a CCP image along a 140-km-long profile across the San Andreas Fault in southern California from stacking 941 short-period receiver functions.

7.5   Core phases

7.6 Exercises

1. Download the receiver function package from www.eas.slu.edu/People/LZhu/home.html and compile the deconvolution programs *decon* and *iter_decon*. Use them to compute receiver functions of station KUL. A three-component teleseismic recording is provided with the package. Compare your results from the frequency-domain deconvolution *decon* and the time-domain deconvolution *iter_decon*. Identify and measure the delay of the Moho P-to-S converted phase.

2. Compile the theoretical receiver function program *rcvFn* and use it to compute the receiver function for a standard crustal velocity model assuming that the ray parameter of the incident teleseismic P wave is 0.06 s/km. Adjust your crustal model to best-fit the observed receiver function of KUL.
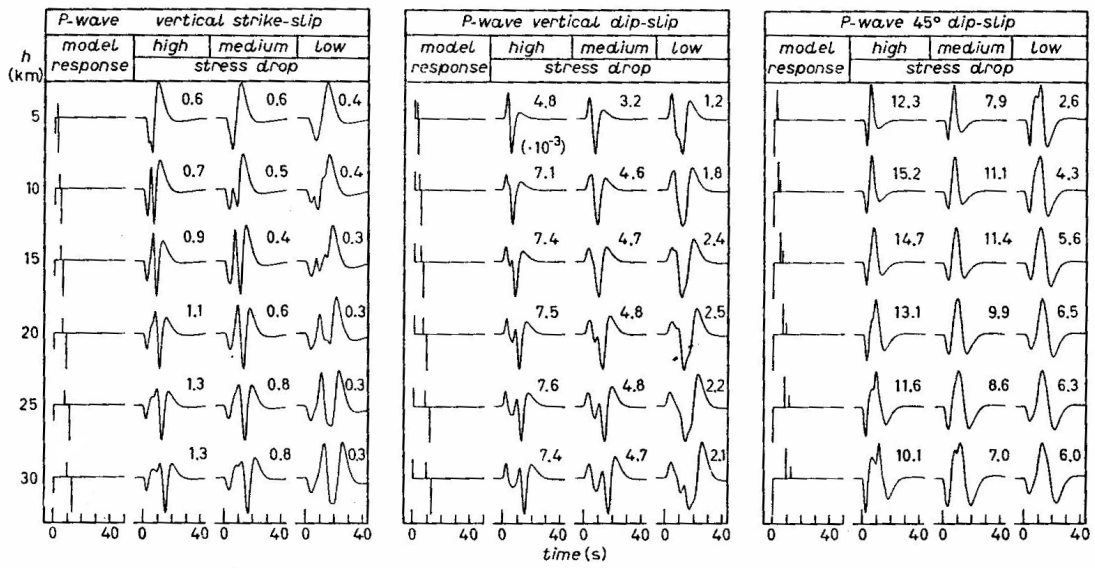
Figure 7.5: Teleseismic *P*-wave synthetics. The source time functions are (0.5, 1.0, 0.5) secs for high stress-drop, (1.0, 3.0, 1.0) secs for medium stress-drop, and (2.0, 6.0, 2.0) for low stress-drop. From Helmberger [1983].
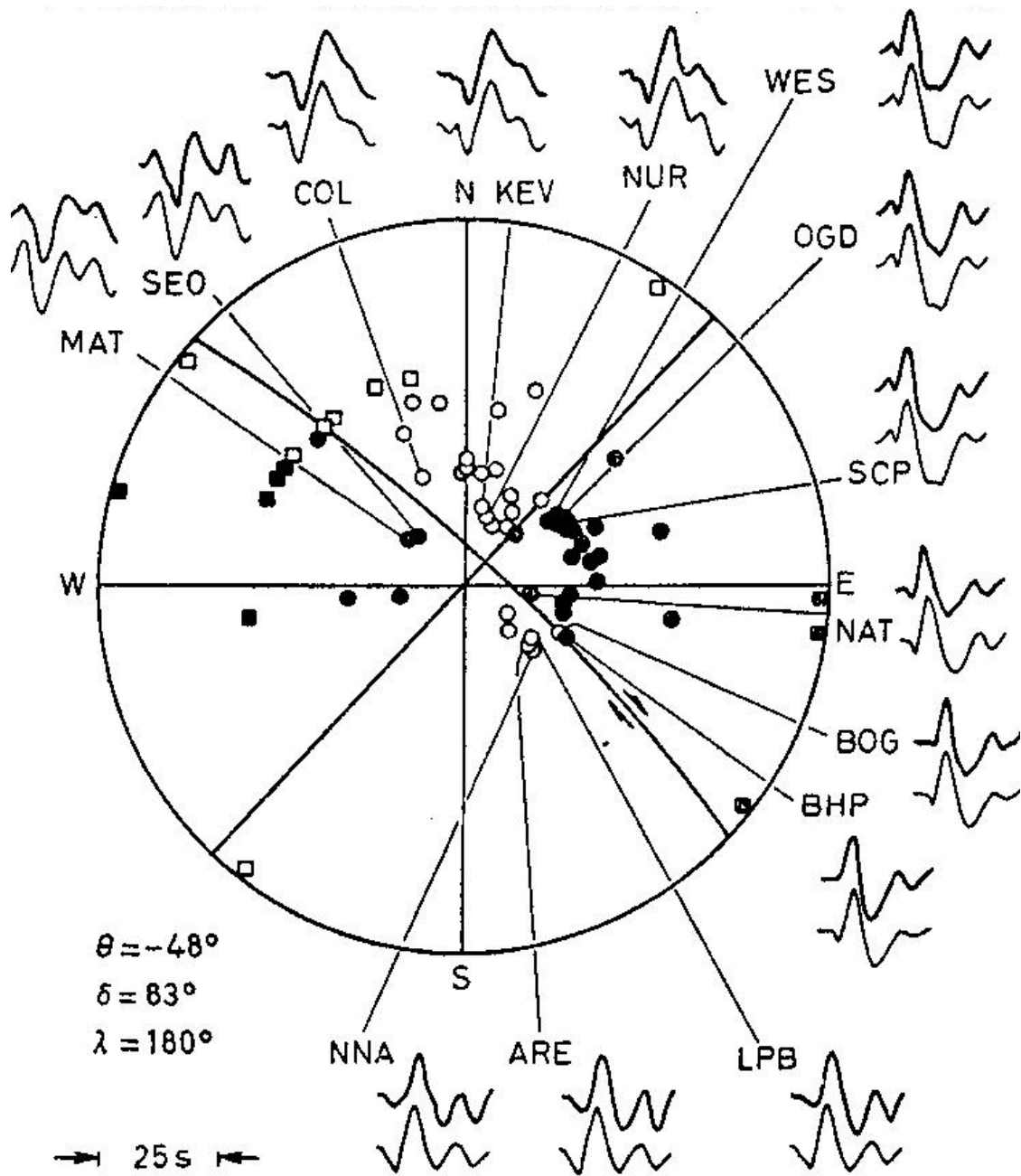
Figure 7.6: Observed (top) and synthetic (bottom) long-period P waveforms at 14 WWSSN stations from the Borrego Mtn. earthquake. From Helmberger [1983].
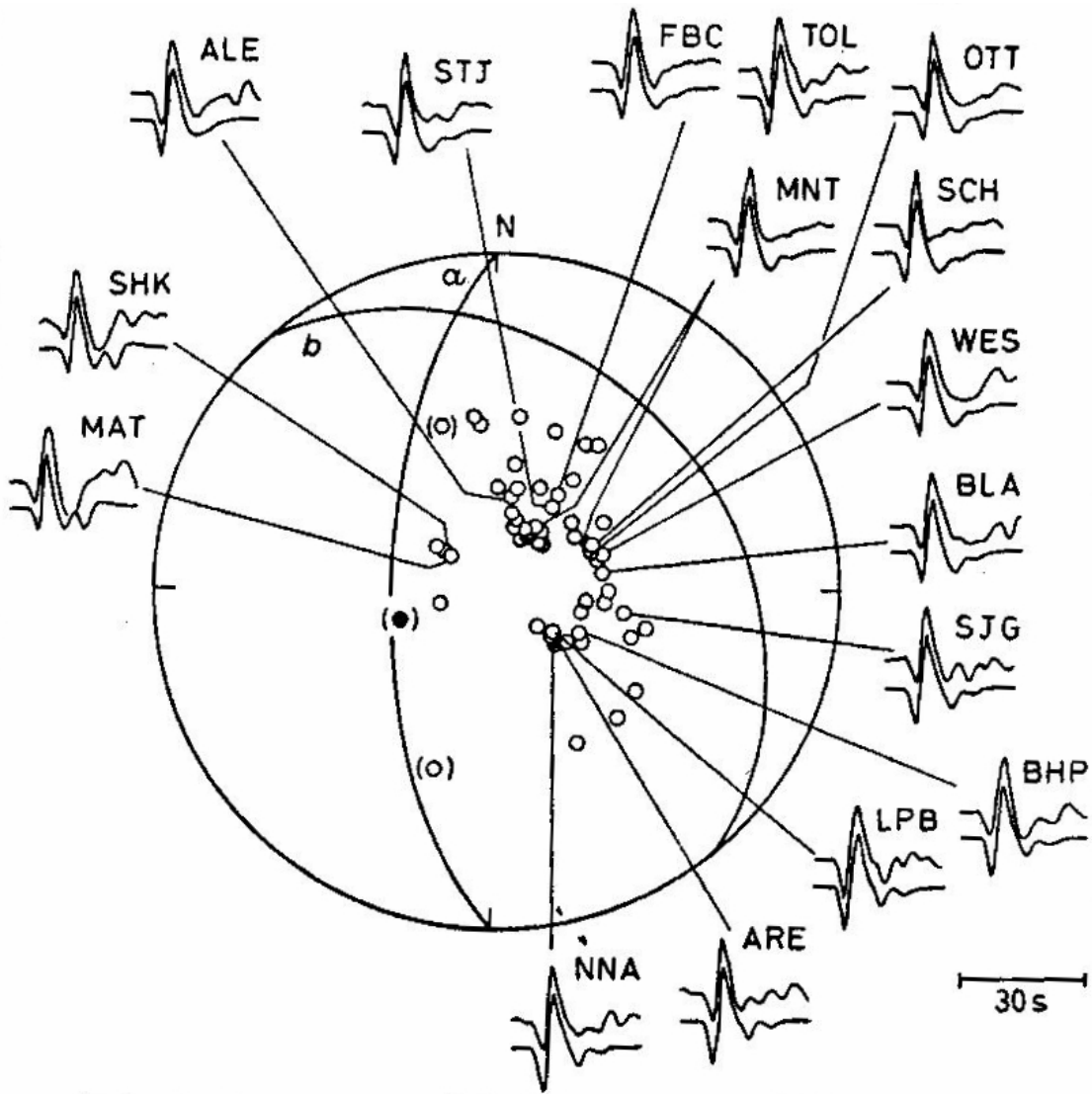
Figure 7.7: Observed (top) and synthetic (bottom) long-period P waveforms from the Oroville earthquake on Aug. 1, 1975 (strike 180°, dip 65°, rake -70°). From Helmberger [1983].

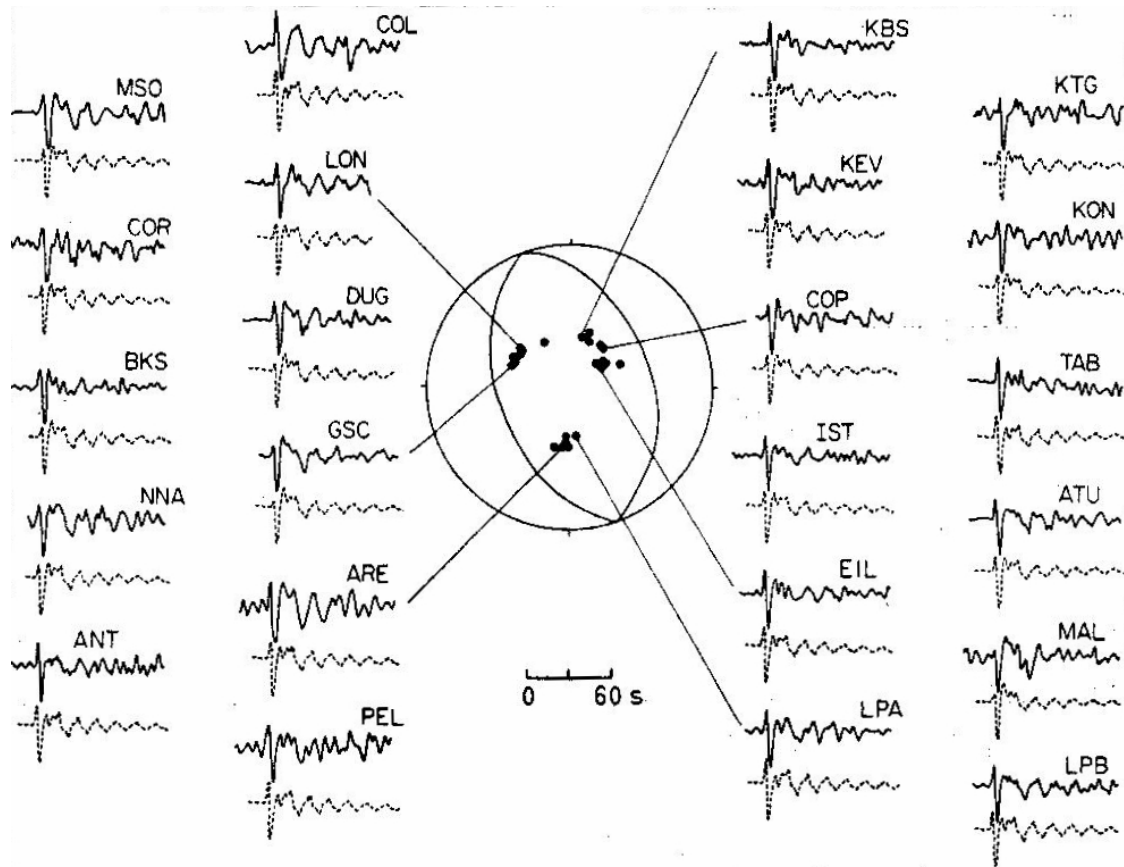Figure 7.8: Observed (top) and synthetic (bottom) vertical long-period WWSSN P waveforms from the Bermuda earthquake on March 24, 1978. From Helmberger [1983].
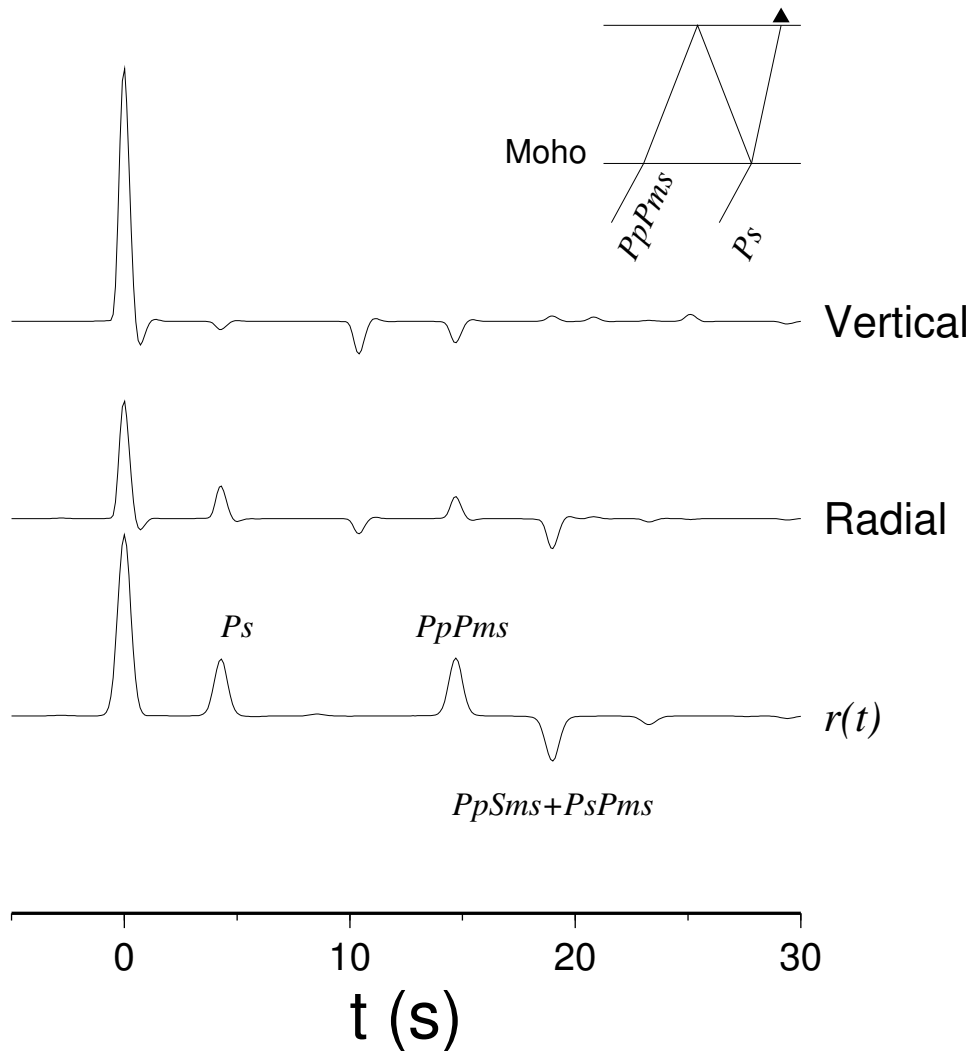
Figure 7.9: Receiver functions of a one-layer crustal model. The ray parameter of the incident P wave is 0.06 km/s.

Figure 7.10: Teleseismic receiver functions (right) computed from 10 teleseismic events recorded at station PAS (left).
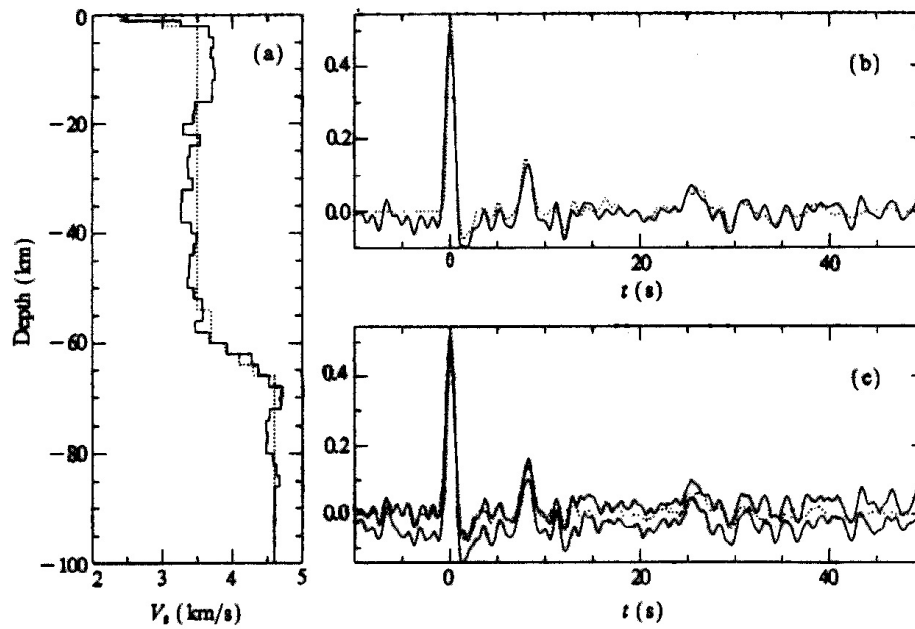
Figure 7.11: Inversion results using receiver functions of WNDO from SE. (a) Initial (dashed line) and final (solid line) shear velocity models. (b) the fit of final synthetic receiver function (dashed line) to both the mean receiver function (solid line) and the bounds (c).

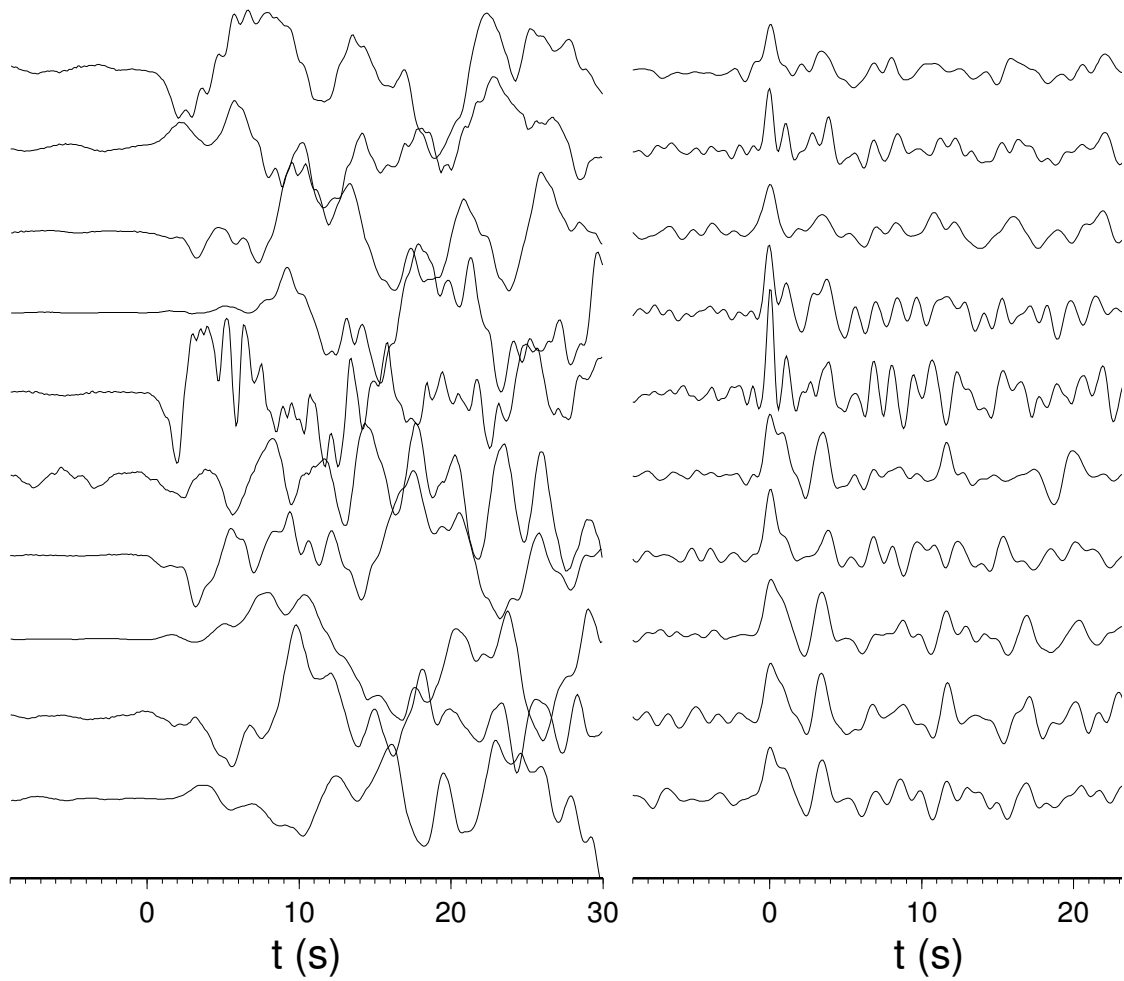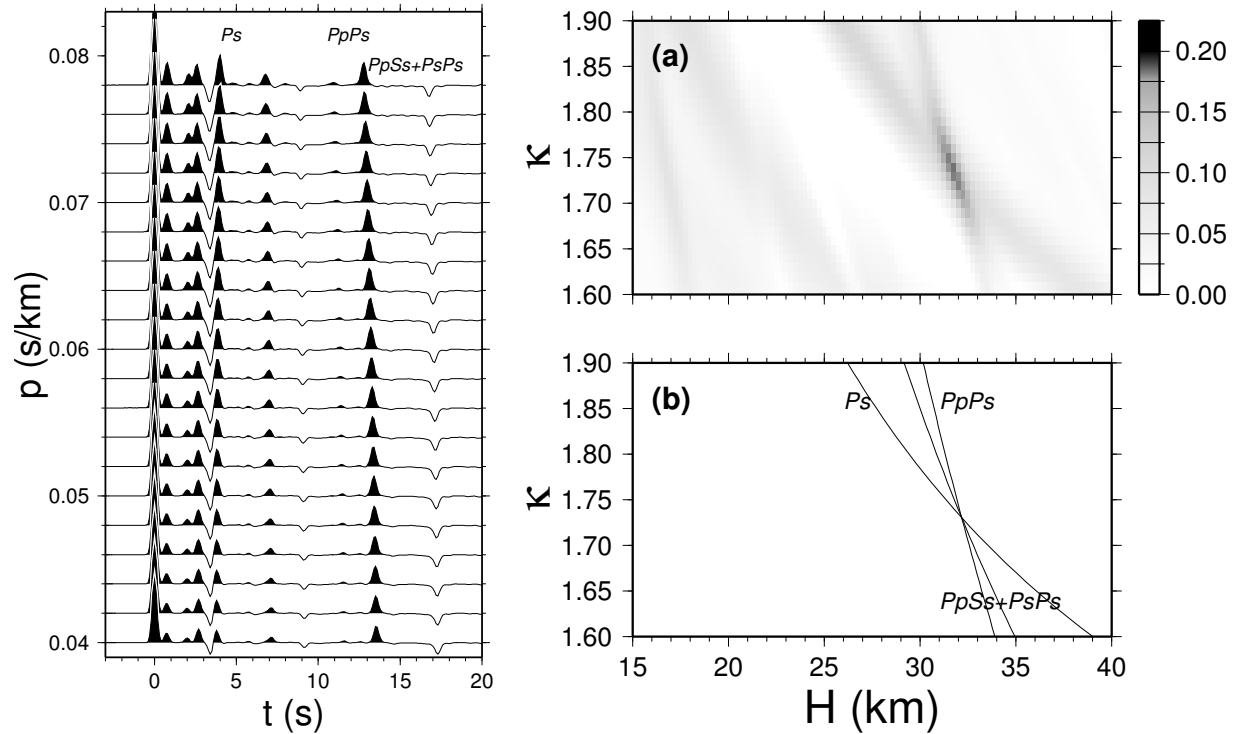Figure 7.12: The left panel shows radial receiver function as a function of ray parameter p for the Standard Southern California Velocity Model. Right: (a) The $s(H, \kappa)$ from stacking the receiver functions using (7.10). It reaches the maximum (solid area) when the correct crustal thickness and V_p/V_s ratio are used in the stacking. (b) H-κ relations, as given in (7.7)–(7.9), for different Moho converted phases. Each curve represents the contribution from this converted phase to the stacking.
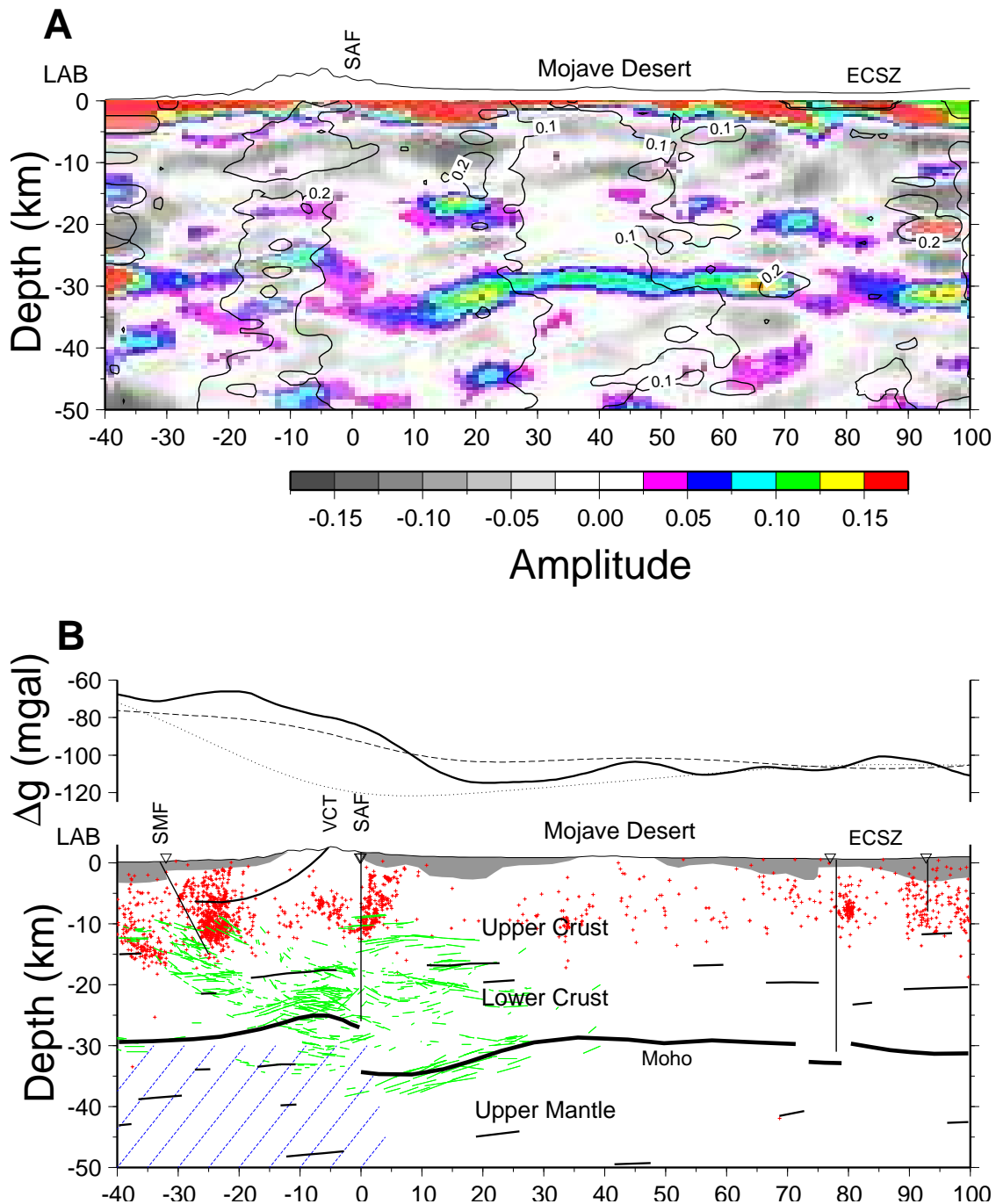
Figure 7.13: (A) The amplitude and variance (given by the contours) of CCP stacking. No vertical exaggeration except that the surface topography is amplified by a factor of 2. SAF: San Andreas Fault; LAB: Los Angeles Basin. (B) Crustal structure along the profile based on A. The thickened black lines are Moho and other possible velocity discontinuities. SMF: Sierra Madre Fault; VCT: Vicent Thrust Fault. Red crosses are earthquakes within the profile between 1981 and 1998. Green lines are the crustal reflectors imaged by LARSE [Ryberg and Fuis, 1998]; Hatched area in the upper mantle represents the Transverse Range high velocity anomaly from seismic tomography [Humphreys and Clayton, 1990]. Plotted on the top are the observed Bouguer gravity anomaly and the predicted Bouguer anomalies using the determined Moho topography (dashed line) and the Airy isostasy model (dotted line).

Figure 7.14: Vertical component of GRT synthetic seismograms for the IASPE91 model.
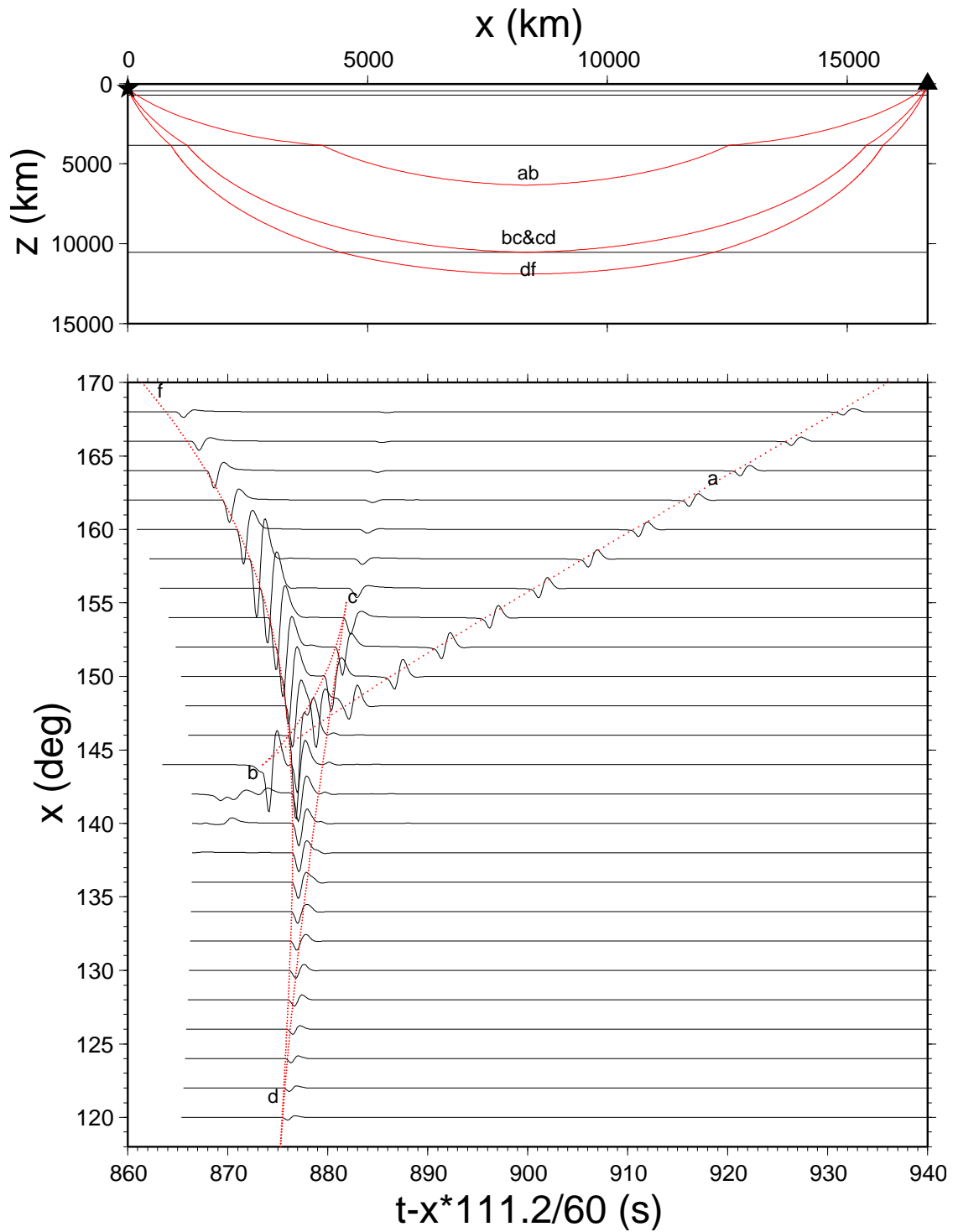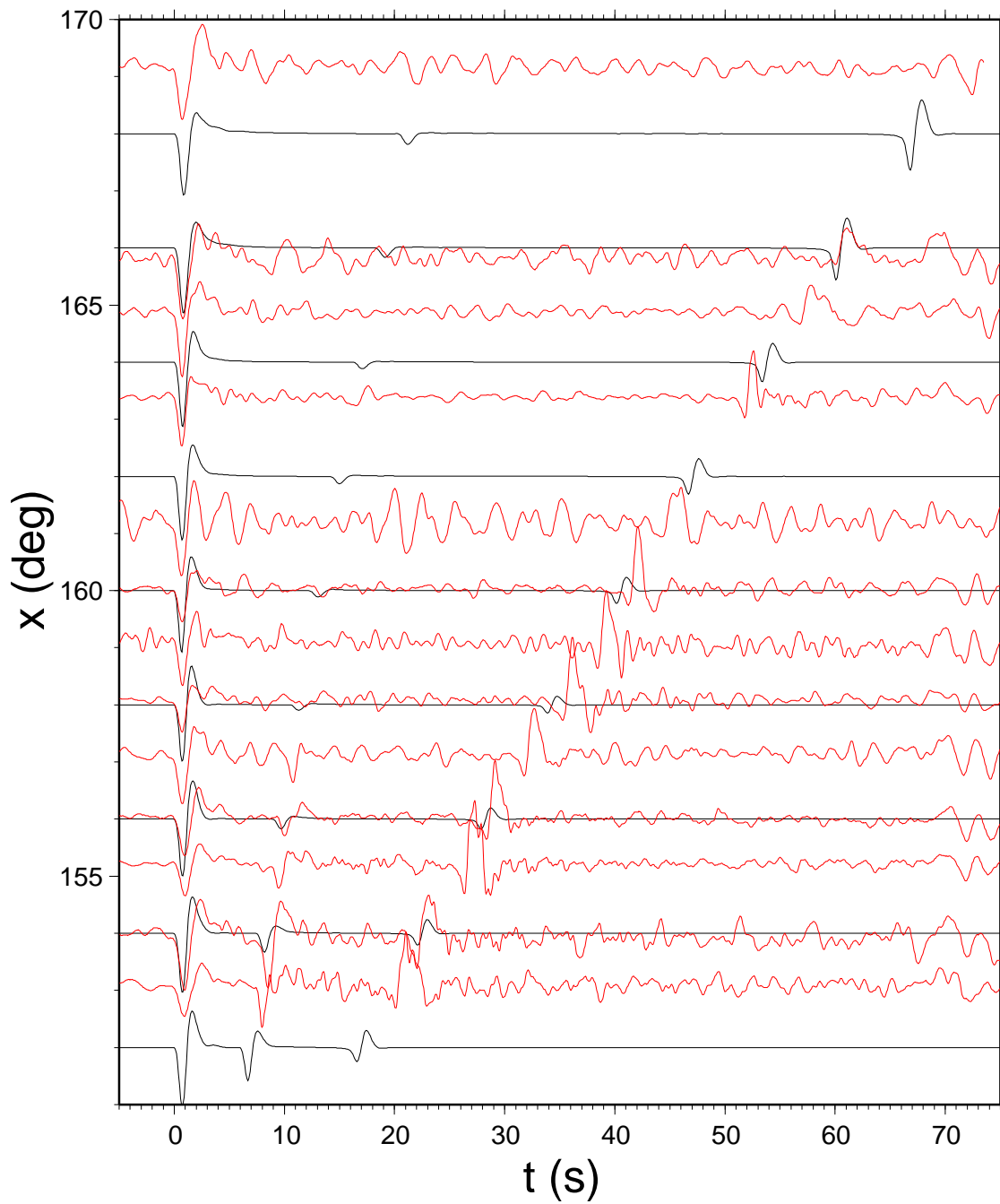
Figure 7.15: Comparison between observed (red) and synthetic vertical component of velocity records from the 6/29/2001 Mw 6.1 earthquake.

Bibliography

D. V. Helmberger. Theory and application of synthetic seismograms. In *Earthquakes: Observation, Theory and Interpretation*, pages 174–222. Soc. Italiana di Fisica, Bolgna, Italy, 1983.

K. Aki and P. G. Richards. *Quantitative Seismology, Theory and Methods*. Freeman and Company, San Francisco, 1980.

L. Zhu. Recovering permanent displacements from seismic records of the June 9, 1994 Bolivia deep earthquake. *Geophys. Res. Lett.*, 30(14):1740, doi:10.1029/2003GL017302, 2003.

J. E. Vidale, S. Goes, and P. G. Richards. Near-field deformation seen on distant broadband seismograms. *Geophys. Res. Lett.*, 22:1–4, 1995.

T. Ryberg and G.S. Fuis. The San Gabriel Mountains bright reflective zone: possible evidence of young mid-crustal thrust faulting in southern California. *Tectonophys.*, 286(1-4):31–46, 1998.

E.D. Humphreys and R.W. Clayton. Tomographic image of the southern California mantle. *J. Geophys. Res.*, 95(B12):19725–19746, 1990.

L. Knopoff and M. J. Randall. The compensated linear-vector dipole: a possible mechanism for deep earthquake. *J. Geophys. Res.*, 75:4957–4963, 1970.

M. L. Jost and R. B. Herrmann. A student's guide to and review of moment tensors. *Seismol. Res. Lett.*, 60:37–57, 1989.

J. A. Hudson, R. G. Pearce, and R. M. Rogers. Source type plot for inversion of the moment tensor. *J. Geophys. Res.*, 94:765, 1989. doi: 10.1029/JB094iB01p00765.

C. H. Chapman and W. S. Leaney. A new moment-tensor decomposition for seismic events in anisotopic media. *Geophys. J. Int.*, 188:343–370, 2011. doi: 10.1111/j.1365-246X.2011.05265.x.

T. W. Spencer. The method of generalized reflection and transmission coefficients. *Geophysics*, 25:625–641, 1960.

D. V. Helmberger. The crust-mantle transition in the Bering Sea. *Bull. Seismol. Soc. Am.*, 58:179–214, 1968.

H. Takeuchi and M. Saito. Seismic surface waves. In B. A. Bolt, editor, *Methods in Computational Physics*, volume 11, pages 217–295. Academic Press, New York, 1972.

H. W. Turnbull and A. C. Aitken. *An introduction to the theory of canonical matrices.* Blackie and Son, Ltd., London and Glasgow, 1952.

F. R. Gantmatcher. *Matrix Theory.* Chelsea Publishing Company, New York, N. Y., 1960.

N. A. Haskell. Radiation pattern of surface waves from point sources in a multi-layered medium. *Bull. Seismol. Soc. Am.*, 54:377–393, 1964.

C. Y. Wang and R. B. Herrmann. A numerical study of P, SV, and SH-wave generation in a plane layered medium. *Bull. Seismol. Soc. Am.*, 70:1015–1036, 1980.

N. A. Haskell. The dispersion of surface waves on multilayered media. *Bull. Seismol. Soc. Am.*, 43:17–34, 1953.

M. Bouchon. A simple method to calculate green's function for elastic layered media. *Bull. Seismol. Soc. Am.*, 71:959–971, 1981.

C. K. Saikia. Modified frequency-wavenumber algorithm for regional seismograms using filon-quadrature method – modeling of Lg waves in eastern North-America. *Geophys. J. Int.*, 118:142–158, 1994.

R. B. Herrmann. *Seismic Wave in Layered Media.* http://http://www.eas.slu.edu/People/RBHerrmann/CPS330.html, 2007.

L. Zhu and L. A. Rivera. A note on the dynamic and static displacements from a point source in multi-layered media. *Geophys. J. Int.*, 148:619–627, 2002.

P. Molnar and W. P. Chen. Focal depths and fault plane solutions of earthquakes under the Tibetan plateau. *J. Geophys. Res.*, 88:1180–1196, 1983.

N. N. Biswas and L. Knopoff. Exact earth-flattening calculation for Love waves. *Bull. Seismol. Soc. Am.*, 60:1123–1137, 1970.

C. H. Chapman. The earth flattening transformation in body wave theory. *Geophys. J. R. astr. Soc.*, 35:55–70, 1973.

S. N. Bhattacharya. Earth-flattening transformation for P-SV waves. *Bull. Seismol. Soc. Am.*, 86:1979–1982, 1996.

M. R. Brudzinski and Wang-Ping Chen. A petrologic anomaly accompanying outboard earthquakes beneath Fiji-Tonga: Corresponding evidence from broadband P and S waveforms. *J. Geophys. Res.*, 108:2299,doi:10.1029/2002JB002012, 2003.

Y. Tan and D. V. Helmberger. Trans-pacific upper mantle shear velocity structure. *J. Geophys. Res.*, submitted, 2006.

C. A. Langston. The effect of planar dipping structure on source and receiver responses for constant ray parameter. *Bull. Seismol. Soc. Am.*, 67:1029–1050, 1977.

M. Kikuchi and H. Kanamori. Inversion of complex body waves. *Bull. Seismol. Soc. Am.*, 72:491, 1982.

T. J. Owens, G. Zandt, and S. R. Taylor. Seismic evidence for ancient rift beneath the Cumberland plateau, Tennessee: A detailed analysis of broadband teleseismic *P* waveforms. *J. Geophys. Res.*, 89:7783–7795, 1984.

C. J. Ammon, G. E. Randall, and G. Zandt. On the nonuniqueness of receiver function inversions. *J. Geophys. Res.*, 95:15,303–15,318, 1990.

B. Kennett. *Seismic wave propagation in stratified media*. Cambridge University Press, 1983.

G. E. Randall. Efficient calculation of differential seismograms for lithosphere receiver functions. *Geophys. J. Int.*, 99:469–481, 1989.

L. Zhu, R. S. Zeng, F. T. Wu, T. J. Owens, and G. E. Randall. Preliminary study of crust-upper mantle structure of the Tibetan plateau by using broadband teleseismic body waveforms. *Acta Seismol. Sinica*, 6:305–315, 1993.

L. Zhu. Estimation of crustal thickness and V_p/V_s ratio beneath the Tibetan Plateau from teleseismic converted waves. *Eos Trans. AGU*, 74(16):Spring Meeting Suppl., 202, 1993.

G. Zandt, S. C. Myers, and T. C. Wallace. Crust and mantle structure across the Basin and Range-Colorado Plateau boundary at 37N latitude and implications for Cenozoic extensional mechanism. *J. Geophys. Res.*, 100:10529–10548, 1995.

G. Zandt and C. J. Ammon. Continental-crust composition constrained by measurements of crustal Poissons ratio. *Nature*, 374:152–154, 1995.

L. Zhu and H. Kanamori. Moho depth variation in southern California from teleseismic receiver functions. *J. Geophys. Res.*, 105:2969–2980, 2000.

L. Zhu. Crustal structure across the San Andreas Fault, southern California from teleseismic converted waves. *Earth Planet. Sci. Lett.*, 179:183–190, 2000.